Instrument Design and Radiation Pattern Testing

for Terahertz Astronomical Instruments

by

Kristina Davis

A Dissertation Presented in Partial Fulfillment
of the Requirements for the Degree
Doctor of Philosophy

Approved March 14, 2018 by the
Graduate Supervisory Committee:

Christopher Groppi, Chair
Philip Mauskopf
Judd Bowman
George Pan
George Trichopoulos
Willem Jellema

ARIZONA STATE UNIVERSITY

May 2018

ABSTRACT

The Milky Way galaxy is a powerful dynamic system that is highly efficient at recycling material. Stars are born out of intergalactic gas and dust, fuse light elements into heavier elements in their cores, then upon stellar death spread material throughout the galaxy, either by diffusion of planetary nebula or by explosive events for high mass stars, and that gas must cool and condense to form stellar nurseries. Though the stellar lifecycle has been studied in detail, relatively little is known about the processes by which hot, diffuse gas ejected by dying stars cools and conglomerates in the interstellar medium (ISM). Much of this mystery arises because only recently have instruments with sufficient spatial and spectral resolution, sensitivity, and bandwidth become available in the terahertz (THz) frequency spectrum where these clouds peak in either thermal or line emission. In this dissertation, I will demonstrate technology advancement of instruments in this frequency regime with new characterization techniques, machining strategies, and scientific models of the spectral behavior of gas species targeted by these instruments.

I begin this work with a description of radiation pattern measurements and their use in astronomical instrument characterization. I will introduce a novel technique to measure complex (phase-sensitive) field patterns using direct detectors. I successfully demonstrate the technique with a single pixel microwave inductance detectors (MKID) experiment. I expand that work by measuring the APEX MKID (A-MKID) focal plane array of 880 pixel detectors centered at 350 GHz. In both chapters I discuss the development of an analysis pipeline to take advantage of all information provided by complex field mapping. I then discuss the design, simulation, fabrication processes, and characterization of a circular-to-rectangular waveguide transformer module integrated

into a circularly symmetric feedhorn block. I conclude with a summary of this work and how to advance these technologies for future ISM studies.

DEDICATION

I dedicate this dissertation to Boulder Tyrell Davis, who encouraged me to go on runs, was really patient when I was busy with deadlines, and who was really sad when I wouldn't let him eat tennis ball fragments; but who was always there to snuggle, let me dress him up in costumes, and didn't mind when I sang to him really *really* off-key. You are my sunshine.

ACKNOWLEDGMENTS

Though there are many people that have helped me along my journey though graduate school, my family and friends have helped the most. Without your support to keep me from drowning in the craziness and stress of school and work, I would have never made it to the end. I would like to thank first and foremost my mom, for proofreading all of my papers since elementary school and for showing up to all of my events and performances, from soccer games, to band recitals, to ski races, and to my defense. I would like to thank my dad for escalating April Fool's day way too far and for encouraging me to pursue all of my crazy dreams, including being a bear zoologist, an orthodontist, and even the dream of being an astrophysics instrument scientist. I thank my brother and sister for helping me have fun during my days off from school, going on action-packed camping trips, and making fun of Dad when he was a snow-butt. I thank Garrett for making me coffee in the morning, singing terribly, learning to ski and teaching me to climb, sometimes listening, and simultaneously being the SD and the AC. I thank Theresa for being there for me always, even though we live states apart, and pushing me to get outside and to go backpacking. I want to acknowledge and thank my mini-support crew in Phoenix, Leslie Rychel, Helen Burtis, and Mindy Leu. Lastly, I would like to thank Chris Groppi for being not just an advisor but also a friend.

Professionally, I would like to start by thanking Chris Groppi for all of his advising and support over the years. You were the embodiment of what it means to be an advisor and not just a boss, and you worked with me to guide my journey into a career rather than just a degree. I also thank you for all the opportunities you gave me for professional growth, from travel for international collaborations to conduct pioneering research, taking me on conference travel all over the world to highlight

my work, and including me on the STO-2 team to gain hands-on experience with ballooning observatory integration, flight, commissioning, and operations.

I would like to thank everyone involved in making the ASU School of Earth and Space Exploration a top-tier interdisciplinary department. I really enjoyed the program, and I believe SESE and ASU set me up on a path for great success. I especially need to thank Chris Groppi and Paul Scowen, who organized the weekly Engineering Coffee. Weekly EC was my favorite aspect of the department and which I valued highly as a way to broaden my research interests and knowledge. One of the unsung benefits of those efforts were to realize how broad the astronomical instrumentation field is, and demonstrate that there are academic and industry partners that value interdisciplinary skill sets.

To my fellow grad students in the instrumentation group, thank you for all of the fun conversations and Friday afternoon hangouts. Good luck with your research, and I hope you know you all are seriously impressive scientists and engineers. I also want to thank my fellow SESE Grad Council members, with whom I fostered good relationships that allowed us to be better advocates for student issues. There are many friends from grad school who were helpful and supportive on my journey, but none more so than Caleb Wheeler and Natalie Hinkel, who I felt like I could turn to and trust with any and all discussions, both professionally and personally. I would like to acknowledge Andy Ryan and Scott Robinson for their support throughout the years. To all of my other countless friends from ASU, I thank you deeply for making my time in grad school worthwhile, and wish you success down whatever path life takes you.

I would like to thank all of my colleagues at SRON in the Netherlands. Without your collaboration, more than half of this dissertation would not have been possible. I

sincerely thank you for the opportunity to work on such an important project and to spend time mentoring me about MKIDs, Fourier optics, and multi-level data processing. It is always difficult to walk into another lab and start making progress immediately, and you were very helpful in making sure I had adequate support resources to make the most out of my visits. I want to especially thank Willem Jellema, Andrey Baryshev, and Stephen Yates for their continual support through my two publications. There are also many at SRON who helped me with these projects, whether they were involved or not. Those folks include Jochem Baselmans, Lorenza Ferrari, José da Silva, Andrey Kudchenko, Juan Bueno, Ronald Hesper, and Pieter Dieleman.

Lastly, I thank the STO-2 Antarctic campaign members from both of my seasons on the ice. I was very glad to be a part of the instrument team, and I want to thank all for involving me as a graduate student and letting me learn how to work on large collaborative projects. The team members include PI Chris Walker, Craig Kulesa, Bill Peters, Darron Hayton, Jenna Kloosterman, Jon Kawamura, Jose V. Siles, Wouter Laauwen, Brian Duffy, Ruben Domingez, Jian-Rong Gao, Abe Young, and last but very much not least, Casey Honniball. I also want to thank the members of the Columbia Science Balloon Facility crew that were helpful in both launching our mission and having fun around the station, including Garrison Breeding, Spence McDonald, Cesar Villasana, and Dale Spangler, as well as other fellow McMurdoans Lisa Marie Johnson, Jules Uberuaga, Amy Varga, Danny Uhlman, Mik Metzler, Mark 'Tubs' Evans, Gabriel Trilling, Brian & Steph, and the countless other friends and support crew members that made McMurdo the adventure of a lifetime.

TABLE OF CONTENTS

LIST OF TABLES

LIST OF FIGURES

Figure Page

Chapter 1

INTRODUCTION TO GAUSSIAN BEAM FORMALISM AND RADIATION PATTERN MEASUREMENTS

1.1 Scientific Motivation

Studies of the interstellar medium (ISM) are compelling to astronomers trying to understand and contextualize the formation mechanisms of star systems, including our own solar system and star systems around the galaxy. This research contributes to the new and exciting field of exo-planetology where astronomers are beginning to investigate the range of planetary conditions around other stars in the Milky Way. In order to understand what stellar or planetary system may be like, we must also understand where the gas and dust that forms these systems originates, how it evolves, what elements are present and in what ratios, if the chemical abundance is uniform or localized, and how different chemical species cool and condense into the proto-stellar system. As we look outward and try to understand galactic evolution, the relationship between star formation rates, gas mass, and stellar lifecycle can be studied in detail within our own galaxy, and used as a template by which we can understand distant galaxies, and study how different feedback mechanisms might produce the myriad of galaxy types we see in the Universe. We understand that the lifecycle of the interstellar gas and dust is a recycling process, in which previous stellar generations enrich the composition of the surrounding ISM with a higher presence of heavy elements, but the details of this distribution, mixing, cooling, and the conditions for cloud formation

and phase transformation are relatively poorly understood. Several key questions remain in this field, such as:

- How do the different phases of ISM clouds form, disrupt, and transition to subsequent stages?

- How long do the different phases of ISM clouds persist?

- How do ISM clouds interact with their thermal, gravitational, and radiative environment?

- What is/are the mechanism(s) for cloud growth and collapse? What is the role of feedback from internal or nearby star formation in this process?

- How does the evolution of an ISM cloud influence further stages of the stellar life cycle, and particularly the galactic star formation rate (SFR)?

Astronomers can begin to answer these questions by studying the light that the ISM emits, because light is the only observable parameter of these clouds from our position on Earth. To understand the physical processes that govern the creation and evolution of astronomical bodies, we can study how the body interacts with light emitted from other bodies, or we can study the light emitted by the body itself. Generally, direct observations are more prescriptive of the physical nature of the observation target, and are the most useful for deriving the processes that influence the ISM life cycle. Depending on the intensity, spatial position, and frequency of different types of light, we can infer many properties of the emitting gas and dust, including temperature, density, composition, excitation or ionization state, dipole

alignment, bulk and internal motion or rotation, and more. It is often the case that light at different frequencies is used to observe different properties of the ISM, such as different chemical species or different emission mechanisms, combining datasets can give us a more complete picture of the full system dynamics. This is a process that involves back-and-forth iterations between models and observations to begin to answer the questions outlined above. Figure 1.1 gives an example of this process using data from many frequencies using a suite of satellite, high altitude, and ground-based instruments.

Though the nature of the ISM have been of interest to the astronomical community since at least the 1960's and 1970's (Saslaw and Gaustad 1969) (Field, Goldsmith, and Habing 1969) (Parker 1966), (Solomon 1973) (Lovas and Krupenie 1974) (McKee and Ostriker 1977) (Draine 1978) (Savage and Mathis 1979), the instrumentation capable of studying light emitted directly from these sources has only become widely viable in the past $\sim$ 30 years. Some of the most diagnostic properties of ISM clouds come from observations within the terahertz (THz) frequency regime, generally defined as $\nu \sim 100$ GHz-5 THz ($\lambda \sim 3$ mm - 60 μm). Many cold bodies in the ISM have a blackbody peak in this regime, and it is the location of key cooling emission lines. From a scientific standpoint, the emission from this regime is considered to be the Far Infrared (FIR), but from an instrumentation standpoint, the technology has developed by pushing microwave detectors to very high frequencies. The astronomical understanding of the ISM has been closely tied with the technological advancement over the past several decades.

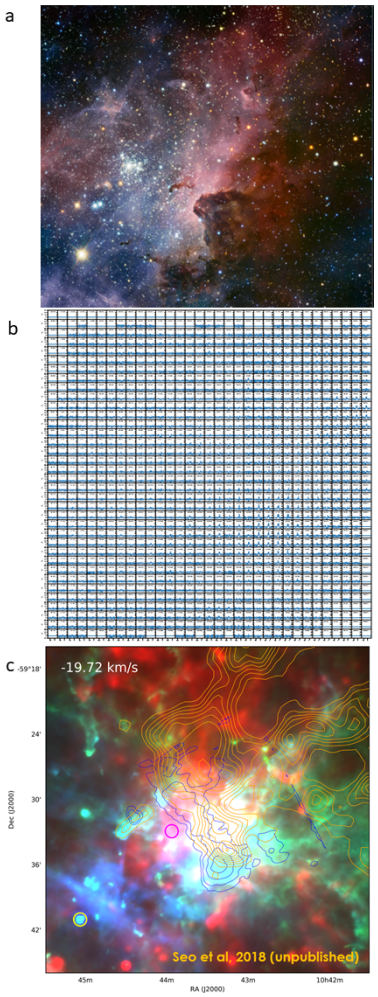

Figure 1.1. The complex ISM region near Eta Carina. The top panel a) shows an optical image of the region taken by the European Space Organization's VLT Survey Telescope (credit: VPHAS+ Consortium/Cambridge Astronomical Survey Unit). The binary star Eta Carina is visible in the lower left, and the newborn star cluster Trumpler 14 is visible up and to the right of the star, just left of the center of the image. The dark bands obscuring the background emission from the upper right and sweeping diagonally downwards to the left is very dense gas and dust, also seen in isolated pockets closer to the Trumpler 14 cluster. Panel b) shows a spectral mosaic of the same region at 1.9 THz as imaged by the STO-2 mission. Image credit: Volker Tolls (with permission). The lowest panel shows a composite image of the same region. Eta Carina is outlined in the gold circle and the location of the Trumpler 14 cluster is outlined in a magenta circle. The contour plot of the spectral mosaic from panel b) is overlaid in the blue contours, from Seo et. al., (2018, unpublished). The gold contours show ^{12}CO $J = 1 \rightarrow 0$ emission of the same region taken from the ground-based Mopra telescopeRebolledo et al. (2016). The diffuse emission is from a far infrared survey of the Carina region taken during the Herschel mission, with data from Herschel at 350 GHz (red), 1.9 THz (green), and 4.3 THz (blue) (Preibisch et al. 2012), (Roccatagliata et al. 2013).

1.1.1 Types of Emission

1.1.1.1 Continuum Emission

There are two ways in which we can study light emitted from astronomical sources. The first is continuum emission, which is the blackbody-esque energy radiated from a body. According to the laws of thermodynamics, all matter that has a physical temperature radiates energy. A blackbody is an idealized case in which radiated energy spectrum is defined solely by its temperature. This radiated energy is in the form of photons (light), and the spectra has a form defined by Planck's Law given by

$$B_\nu(\nu, T) = \frac{2h\nu^3}{c^2} \frac{1}{e^{\frac{h\nu}{kT}} - 1} \tag{1.1}$$

where B is the 'spectral radiance' of the emitted radiation, in units of $\frac{W}{ster\ m^2 Hz}$, ν is the frequency of light in Hertz, T is the temperature of the body in Kevin, h is the Planck constant in JK, c is the speed of light in $^m/_s$, and k is the Boltzmann constant in $^J/_K$. The radiance B_ν has a peak at a particular frequency ν, which indicates the temperature of the body T. Because of the strong relationship between temperature and emission frequency, observations of the peak in continuum emission are the primary way to study the temperature of an astronomical body. Weins' displacement law can be used to find the frequency peak of blackbody emission, which is given by $\nu = {}^{cT}/_b$, where b is a constant, here $2.873 * 10^{-3}$ mK. The THz range corresponds to peak blackbody temperatures between ∼2.5-100 K.

1.1.1.2 Science from Continuum Spectra

Even though continuum radiation is prevalent throughout the universe, because B_ν decreases as T decreases, cold objects are dim. Because all objects that have energy emit this radiation, continuum emission is an excellent way to study cold, diffuse objects that are neither very reflective or emit radiation by other mechanisms. In order to study these bodies, instruments have wide bandwidths centered on the (known or expected) peak of the thermal emission spectrum of the body of interest. A wider bandwidth collects more photons, helping to make dim objects observable.

Continuum emission is well suited to take wide-field images of cold dust. Studies have been conducted to survey large regions of the galactic plane to identify and characterize the position and orientation of cold, dusty ISM clouds, and determine how they interact with their surrounding environment. Dust emits as an approximate thermal blackbody with an emission peak proportional to its size as well as physical temperature. The APEX-Microwave Kinetic Inductance Detector (A-MKID) camera (Otal 2014) commissioned for the APEX telescope in Chile is one example of a mission to study ISM clouds in the Milky Way with continuum detectors. If a polarizing modulation scheme is introduced in the instrumentation, the polarization orientation of a wide-field source can map magnetic field lines in a medium or from distant background sources. The Balloon Large Aperture Stratospheric Telescope-The Next Generation (BLAST-TNG) (Galitzki et al. 2014) aims to observe the importance of galactic field lines in suppressing star formation in dense clouds. It is important to study the dust within the Milky Way to better understand how dust can influence the observations of more distant galaxies. The Stratospheric Terahertz Airborne Receiver for Far-Infrared Exploration (STARFIRE) (Aguirre 2015) aims to study dust-obscured

star forming galaxies (DSFGs) in the nearby Universe. Dust is important for both ISM studies and throughout the Universe, because the dusty ISM is a foreground source that can obscure observations of the Cosmic Microwave Background (CMB).

1.1.1.3 Spectral Emission

The second way that an astronomical body can radiate energy is through spectral emission. Spectral emission occurs when a physical processes emits radiation at a single frequency. Spectral emission is commonly referred to as an emission line. Under idealized conditions, this emission will approach a delta function on a plot of intensity vs frequency. Emission lines are important to study because each spectral line is unique to a physical process, and we can use it to uniquely identify the presence of a particular chemical species within the emitting source.

Because an emission line has a well-defined rest frequency, the spectral line can be used to track the motion of the host body. The Doppler shift of the emission line can tell us how fast the object is moving along our line of sight. Furthermore, if the line is very highly resolved, astronomers can study the profile shape to understand the source's internal motion. In the case of ISM clouds, all or part of the cloud may be rotating, or there may be turbulent motion within the cloud due to external forces acting upon it. Careful modeling of the cloud is needed to separate frequency shifts that may be due to cloud motion versus other factors that might affect the profile shape, such as the presence of magnetic fields or thermal broadening.

There are many forms spectral emission, but two mechanisms are prevalent in the ISM. The first is when asymmetric molecule emits radiation as it rotates. A classic example is for carbon monoxide, a diatomic molecule found in relatively large

quantities in the cold ISM. Because the C and O molecules have different masses, the center of mass is not in the middle of the molecular bond, which is where the center of charge is located (CO is a neutral molecule). Because of this tiny offset, as the CO molecule rotates, the center of charge moves back and forth along the line of sight. A moving charge will emit photons, and so the rotating molecule will radiate.

As is the case with individual electrons orbiting the nucleus of an atom, the rotation states of a molecule are quantized. The rotation states of a molecule are defined by the J parameter, and radiation occurs when a molecule transitions from a higher rotation state to a lower state. In this example, the lowest rotational emission line for CO is the $[^{12}C^{16}O]J = 1 \rightarrow 0$ transition, which will produce a photon at ν=115 GHz (λ=2.6 mm). The rotational emission of the $[CO]J = 3 \rightarrow 2$ transition occurs at 350 GHz, and was the primary target of the 64-pixel SuperCam instrument (Kloosterman et al. 2014).

An atom or molecule tends to be more opaque (better absorber) to radiation with a wavelength that is approximately equal to its physical size. Because of this, hot gas can cool by radiating energy at rotational frequencies that the CO molecule is not likely to re-absorb. Within the ISM, a classic scenario is that a CO molecule may be excited by the absorption of a UV photon or collision with another atom or molecule, and rotate at several progressive de-exciting rotational states before finally reaching the ground state (no rotation). A cloud can cool by this process if the radiated energy exceeds the incident and internal energy.

This rotational emission can be used to study the coldest and most dense proto-stellar 'clumps' of gas. Though H_2 is by far the most abundant species in these regions, it is not an asymmetric molecule, and therefore has no permanent dipole moment and does not emit strongly at these frequencies. In order to probe the cloud mass, the

intensity of the CO emission can be used to determine the abundance of CO, and the total cloud mass can be estimated by the $^{n(CO)}/_{n(H_2)}$ ratio.

The second type of emission spectra occurs when a valence electron spontaneously transitions between hyperfine states. For certain atoms, the valance electron can be either in a spin up or spin down state. However, the spin down state is slightly less energetic than the spin up state, and electrons prefer to be in the lowest available state. Given enough time, a spin up electron will spontaneously transition to the spin down state and emit a photon to get rid of the excess energy. The most well-known type of this emission is the 21 cm hyperfine transition of the hydrogen atom [HI], which is the most accessible probe of the cosmological "Dark Ages" (Bowman et al. 2018). Within the ISM, the hyperfine transition of singly ionized carbon [CII] occurs at ν=1.9 THz (λ=158 μm) (Goldsmith et al. 2012). Because of its prevalence through many ISM phases and cloud types, this emission line is the target of several astronomical studies. The Stratospheric Terahertz Observatory (STO) balloon mission, for which instrumentation in this dissertation was developed, had one frequency channel dedicated to this line.

1.1.1.4 Science from Emission Spectra

Independent of the emission mechanism, highly resolved spectral profiles can be used to probe a variety of different properties of the emitting material. Firstly, since the mechanisms for radiation are highly specific to particular states of individual molecules, the detection of a particular emission feature confirms the presence of that chemical species in the ISM cloud. Furthermore, for the processes described above, there is one photon emitted per transition, the intensity of the emision is proportional

to the total abundance N of that species, usually defined as a column density along the line of sight (denoted by $n = {}^{N}/_{\sigma}$, where σ is the area of the column. For distant observations, σ is proportional to the telescope's beam size).

Not all of the present atoms/molecules of that species may emit a photon within the range of observation. The likelihood of a particular transition to occur depends on many other parameters, both the fundamental rate coefficients—which are quantum-mechanical descriptions of the likelihood for excitation or de-excitation ($A_{u\ell}, B_{u\ell}, B_{\ell u}, C_{u\ell}$, etc) for various mechanisms—as well as parameters of the cloud environment, including the kinetic and excitation temperature of the gas, whether the gas is in thermal equilibrium or not, the radiation background, the density of the cloud. For a more thorough understanding of how these parameters relate to each other, see Walker (2015b), Tielens (2005), and Goldsmith et al. (2012). Through laboratory measurements that probe the rate coefficients and extensive modeling using radiative transfer numerical solvers, a representative synthetic spectra can be fit to the observed data by tweaking the environmental factors to "back out" a cloud's properties.

There are some physical drivers of emission spectra that make the observation more precise at determining certain cloud parameters than others. For example, the density of the observed species within the cloud can influence the intensity of the observed radiation. Since the emitted radiation from a particular emission mechanism can be re-absorbed by a different atom or molecule as an excitation process, the chance of a photon escaping the cloud will (generally) decrease as the density of that species increases. This process is described by the optical depth of the radiation, which is given by the equation

$$\tau_\nu = ln\left(\frac{\Phi^i_{e,\nu}}{\Phi^t_{e,\nu}}\right) \tag{1.2}$$

where τ_ν is the frequency dependent optical depth, and $\Phi^x_{e,\nu}$ is the spectral radiance

incident ($x = i$) (in this case, from within) or transmitted ($x = t$) through the cloud, respectively. Optical depth is not a unit of distance, but is a relationship showing how likely a photon is to escape the cloud without being reabsorbed or scattered. From an observational standpoint, the optical depth of the cloud is the number of scattering or absorption events a photon will encounter as it travels from the back of the cloud until it escapes along the line of sight. An optical depth of 1 means that a photon emitted from the back of the cloud will encounter only one absorption event on its way out of the cloud. In practical terms, this means the astronomer can see the back of the cloud. If $\tau > 1$, photons emitted from the back of the cloud are either re-absorbed or scattered out of the line of sight, so the astronomer cannot see all the way through the cloud (only photons from the surface layer of the the cloud make it to the astronomer).

In the case of $\tau \gg 1$, a cloud is said to be optically thick. In that case, the astronomer can only see the surface layer of the cloud, and the intensity of the emission is not representative of the total number of atoms/molecules along the line of sight (n). However, since a high optical depth occurs in dense clouds, the species is likely to be in thermal equilibrium with its surroundings, meaning the excitation temperature of the gas is the same as the thermal temperature. Therefore, optically thick emission features are diagnostic of the thermal properties of a cloud.

Conversely, when $\tau \ll 1$, a cloud is said to be optically thin, and the astronomer can see all the photons radiated throughout the cloud. In this case, the intensity of the spectral feature is proportional to the column density n. Because the different emission conditions are prescriptive of different cloud parameters, it is often the case that multiple emission features from different chemical species can be combined to get a more complete understanding of the cloud environment and dynamics. A classic

example of this is the simultaneous observation of [^{12}CO] versus [^{13}CO], the former being (generally) optically thick and the latter being optically thin, due to the relative abundances of the different isotopes of Carbon.

1.2 THz Astronomical Instrumentation

Astronomers design instruments to meet specific sensitivity, field of view, and resolution requirements suitable to study the scientific question at hand. Once the instrument is assembled, it must be tested to determine how well it matches the designed performance. The optical properties of the individual components must be calibrated to model the behavior of the complete assembly, and careful alignment during system integration is necessary to ensure maximum sensitivity and resolution. There are many figures of merit to characterize the optical performance of an instrument, but this dissertation will focus on measuring the instrument's radiation pattern in several ways for multiple receiver configurations as a way to check system alignment and optical efficiency.

Because of the reciprocity theorem (Balanis 2005) the sensitivity pattern (beam) of an instrument in a receiving mode is the same as the beam of light that would emerge from the system when used as a transmitter, and it is often convenient to think of a receiver's sensitivity as a beam emerging from the instrument. When thinking of the radiation pattern in this way, it can also be referred to as a beam pattern measurement. In the THz regime, the photon's wavelength λ is comparable to the detector device's physical dimensions. Rather than treating the photon as a point-like particle, full quantum-mechanical analysis must be applied, where a photon is treated as a quantized but dispersed field (with a wave-like nature).

Here, I will loosely refer to a system involved in capturing light as an instrument, and the specific device used for converting a photon into a voltage signal I will refer to as the detector. A detector is not often directly exposed to the optical environment of the instrument, and is coupled to free space with an antenna, typically a lenslet or feedhorn mounted in front of the detector chip. As a fundamental optical element, I will generally refer to this configuration as a detector sub-assembly. An instrument is designed to consist of a detector sub-assembly followed by other optical elements, namely lenses, mirrors, and apertures, before exiting a telescope and looking out to space. Generally, a receiver system refers to the optical elements of an instrument minus the telescope primary and secondary mirrors, though the term is imprecise. I will do my best to keep this nomenclature consistent throughout this dissertation, and I will try to make the distinction clear when I find it necessary to deviate from this plan.

1.3 What are Radiation Pattern Measurements?

At its most basic level, a radiation pattern measures the sensitivity of a receiving instrument as a function of angle from the principle axis of the optical system. The end result is a dataset consisting of (x, y, z, S) data points, where (x, y, z) define a measurement grid and S is the signal measured on the detector chip. Here I use S as a general output term. In most instances, S is a voltage read out by some mechanism, but depending on the operation principle of the instrument, it can be proportional to the input frequency or the total power in the beam.

The choice of coordinate axes is arbitrary, so the grid points (x, y, z) can easily be transformed into other coordinate systems. Scans in a 1D line are sufficient for many

applications, though full 2D or 3D scans provide more accurate measurements of the device parameters. Unless otherwise noted, this dissertation will assume a 2D planar beam pattern measurement scheme this scheme is widely used and is a good balance of scanner system simplicity and analysis depth. A planar scanning strategy can either be a point-by-point map where the scanned component is stationary for a sufficient integration time at each point, or the scanned component can move continuously in an on-the-fly scan pattern and the data can be re-gridded onto a uniform scan pattern (Kovacs 2008) .

The detector output S can be either real or complex valued. Chapters 2 and 3 will demonstrate how S can be sampled as a timeseries of voltage readings which can later be transformed to a complex value proportional to the electric field component of a receiver beam at each point in the scan pattern. A beam pattern is useful for measuring the relative change in S across the scan plane, so generally the value of S at any point is not used as an exact calibration measurement. Most often, S is normalized to a point in the scan plane, usually at the center of the coordinate system.

A radiation pattern is used to characterize the instrument for astronomical use. They measure the performance metrics that determining its ability to meet the scientific requirements of the observations. The main figures of merit a beam pattern can measure are:

1. A radiation pattern measurement is analogous to measuring a beam's 'shape' and 'size'. The beam 'shape' or spatial pattern is used to calibrate the absolute brightness of a point source depending on its position within the beam, and the beam size determines the resolution of the telescope. Irregularities in the shape of the beam can be used to diagnose misalignments between elements of the optical system or manufacturing errors of the receiver components.

2. The beam pattern is a way to measure the degree of coupling to a point source, which is a measure of the sensitivity of the instrument. The efficiency of the system is referred to as the throughput of the system, measuring what fraction of photons that hit the primary mirror make it to the detector. Maximum sensitivity is achieved when there are no optical losses through the instrument. Beam patterns on the ground or in the lab can diagnose focusing errors, reflections, or misalignments that introduce losses into the system.
3. A beam pattern measurement can also determine the pointing direction of the optical elements, referred to as the boresight angle of the beam. The boresight angle of the detector is measured relative to the optical axis of the telescope's primary mirror, most often measured using spherical coordinates with an origin at the focal plane. Typically, instruments are designed to have a boresight angle of zero, though this may not be the case for array instruments, off-axis optical configurations, or special circumstances where a beam does not fill the primary mirror. It is important to ensure proper alignment to ensure the telescope is aimed at the target.
4. Lastly, for array instruments, the beam pattern measurement is used to determine the imaging properties of the array. The beam pattern measurements can look at beam shape, sensitivity, and pointing direction as a function of pixel position. One important factor is how well the beams overlap as they appear on the sky, also referred to as the filling factor of the image. This determines whether a single pointing will fully capture and astronomical image or if the instrument will have to shift or dither to fully sample an image.

Because we may be interested in how the beam behaves as it travels through the optical system, and not just at one particular measurement point, we fit the

measurement of S at each position (x, y, z) to a known propagating electromagnetic field function. The field function is a mathematical equation that can be used to model how the beam will be affected by the presence of other optical system elements, and determine the final field of view after emerging from the telescope's primary mirror.

1.4 How are Radiation Patterns Measured?

A radiation pattern measurement can be performed in a laboratory setting or while the instrument is in use. For astronomical cameras, the radiation pattern is usually measured with the camera in the receiving mode, though for special circumstances it may be more convenient to measure parts of the optical system in a transmitting mode (again, possible due to the reciprocity theorem). Both the thermal and optical environment around the camera can affect the measured radiation pattern, so for accurate results most measurements are made in a carefully controlled environment. For example, in the THz frequency regime, absorbing materials are not widely available, so scattering materials are usually coated on surfaces surrounding the optical system. Scattering dilutes the incoming radiation and reduces the fraction of light that is eventually scattered back into the optical path.

To take a beam pattern measurement, either a source or the receiver element is mounted on a mechanical scanning system. S is recorded as a function of the scanner position. Most often, an emitting source probe is mounted on a planar scanning system and scans are made in a Cartesian coordinate grid, though for some applications cylindrical or spherical scans are used. Nyquist sampling theorem (Landau 1967) (Zhu 1992) (Lüke 1999) proves that the maximum step size between scan points of $\lambda/2$ is required for a complete description of the beam. However, scans at smaller

step sizes (oversampling) can extract more information from the measurement, for example reflections and beam steering (Weisstein 2014) . Step sizes as small as $\lambda/10$ or smaller are not uncommon for single pixel measurements. For large focal planes of many pixels there is a trade off between number of sampling points across the field of view and system stability over long scan durations.

The simplest scan mode is a planar Cartesian scan plane with a step-and-integrate mode, where the source probe is stationary for a set period of time at each (x, y) point in the scan plane before moving to the next (x, y) point. One potential disadvantage of this system is that time is lost as the scanner moves and stabilizes at each point. For wide-field instruments that require lots of (x, y) points, this 'dead time' can dominate the scan duration. In chapter 3 we therefore adopt a on-the-fly (OTF) scanning strategy. In this mode, the source probe is in constant motion across the scan plane, and data is recorded continuously at the detector. The X/Y motion stage position is time stamped, and the data output must be correlated to the stage motion in post-processing. The data is then averaged with other nearby samples and gridded onto a scan plane at regular intervals.

1.5 The Gaussian-Hermite Field Expression

In the THz frequency regime, the wavelength of the received radiation is comparable to the dimensions of the optical elements it interacts with, the telescope beam will suffer diffraction effects such that ray tracing is no longer valid as it is in the optical regime. Instead, the beam is better modeled as a Gaussian function, and so instrument scientists often choose to design their optical systems using Gaussian optics principles. This is also a matter of convenience, because in Fourier optics a Gaussian beam

transforms to another Gaussian beam, allowing a single set of equations to describe the beam at all points in the optical system.

In order to take advantage of the diagnostic power of a beam pattern measurement, the measured beam pattern is fit to a fundamental field function so that the instrument's performance can be modeled and verified. This section will describe the Gauss-Hermite function in detail, and section 1.7.3 will discuss the method used throughout this dissertation to take a measurement of $S(x, y, z)$ and fit it to this function. Other field functions can describe the nature of beams in this frequency regime, for example a truncated Bessel function (Functions et al. 2012), (Yousif and Melka 1997), but are not considered in this dissertation.

A Gaussian function, in terms of a 2D power function P, has a centralized peak P_o at a centroid location x_o, and falls off exponentially and symmetrically as a function of distance $\pm x$ from the centroid location. Therefore, $P(x_o) = P_o$ and

$$P(x) = P_o \; exp\left(-2\frac{x^2}{\omega(z)^2}\right) \tag{1.3}$$

where ω is the width of the function measured from the central axis at z, defined as the point where the power amplitude drops to $1/e$ of the on-axis strength (so where $P(x) = {}^{P_o}/_e$). Here we have adopted an (x, z) planar coordinate system. The term ω is referred to as the beam radius, since it is measured from the axis defined by x_o. A convenient reference point for a Gaussian function is the point z at which the function of $P(x)$ is dropped by a factor of two. We refer to this point as the full width at half maximum (FWHM) point. In dB scale, this value occurs at the -3 dB point of the beam. The relationship between the FWHM and the beam radius is $\text{FWHM} = 2\sqrt{2ln(2)}\;\omega(z)$.

In an optical system, we now consider not a 2D Gaussian power function but a 3D propagating electromagnetic field, so $P \rightarrow \vec{E}$, where $\vec{E}$ describes a sensitivity

pattern (the beam). The field $\vec{E}$ is complex, meaning it has both real and imaginary components. At any field point $\vec{E}(x, y, z) = \alpha \pm i\beta$, the amplitude of the beam is $\sqrt{\alpha^2 + \beta^2}$, and the phase of the beam is $\arctan(\beta/\alpha)$.

$$\vec{E}(x, y, z) = \left(\frac{2}{\pi\omega_x\omega_y}\right)^{\frac{1}{2}} \exp\left[\left(-\frac{x^2}{{\omega_x}^2} - \frac{y^2}{{\omega_y}^2}\right) - 1i\left(\frac{\pi x^2}{\lambda R_x} + \frac{\pi y^2}{\lambda R_y} - \frac{\phi_{0,x}}{2} - \frac{\phi_{0,y}}{2}\right)\right] \tag{1.4}$$

The terms $\omega_x, \omega_y, R_x, R_y, \phi_x$, and ϕ_y can all be re-written in terms of ω_o and z using the following equations:

$$\omega_n(z) = \omega_{0,n}\left[1 + \left(\frac{\lambda z}{\pi{\omega_{0,n}}^2}\right)^2\right]^{\frac{1}{2}} \tag{1.5}$$

$$R_n(z) = z + \frac{1}{z}\left(\frac{\pi{\omega_{0,n}}^2}{\lambda}\right)^2 \tag{1.6}$$

$$\phi_{0,n}(z) = \tan^{-1}\left(\frac{\lambda z}{\pi{\omega_{0,n}}^2}\right) \tag{1.7}$$

where the subscript n can indicate either the x or y axis. Therefore, a Gaussian beam observed in an arbitrary measurement plane can be described by the fundamental parameters $\omega_{0,x}, \omega_{0,y}$, and z.

The full mathematical field function of a propagating Gaussian beam in a 3D Cartesian coordinate system can be described by the first-order Gaussian Hermite polynomial, given in the equation (1.4). Here, we ignore the time dependence of the equation, which is required for beam propagation but is not measured with a radiation pattern measurement and so is not discussed in this dissertation. A full discussion of Gaussian beam propagation is the subject of Goldsmith (1998).

Gaussian beams do not converge into a single focal point, but rather come to a narrowest convergence point at the focal plane. The radius of the beam at that

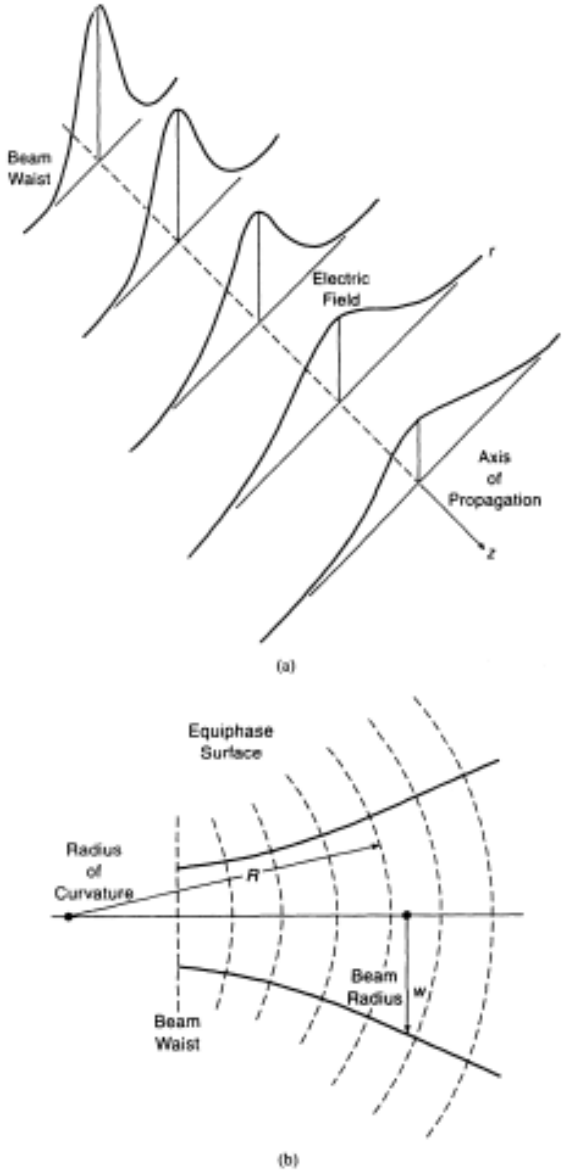

Figure 1.2. Upper panel shows a 1D Gaussian beam as it propagates along the z axis. The beam at the focal plane z_0 initially has a beam waist ω_0 which peaks along the optical axis. As the beam moves along z, the beam radius $\omega(z)$ gets larger, and the peak amplitude decreases. In the lower panel, we look at the beam along the yz plane. The solid lines represent the amplitude of the beam, and the dashed lines show the phase front of the beam. The phase radius R is clearly referenced to a point behind the focal plane. This figure is reproduced from (Goldsmith 1998), with permission.

location is called the beam waist ω_0, indicated in the lower panel of figure 1.2. As the beam propagates outward from this position, the amplitude peak of the Gaussian beam spreads out, getting wider and less prominent, so the beam radius becomes a function of the distance z from the focal point, $\omega(z)$.

The lower panel of figure 1.2 shows the phase of the emerging beam is constant over a spherical surface of a radius R. The location of the phase center is *not* the location of the beam the waist ω_0. If we call the beam waist location $z = 0 \Rightarrow z_0$ then the phase center is located at negative z, or $z < 0$. However, as $z \to \infty$, in equation (1.6) we see that $R \to z$, and thus the phase center approaches z_o for large values of z.

Breaking down equation (1.4), we see that that the fundamental parameters are independent along the $\hat{x}$ and $\hat{y}$ axis. This allows us to fit for beam asymmetries. The beam waist ω_0 can differ along the $\hat{x}$ and $\hat{y}$ axis, so $\omega_{0,x} \neq \omega_{0,y}$. The ratio of $\omega_{0,x}/\omega_{0,y}$ is a measure of the beam's ellipticity. Phase centers that are not aligned along the optical axis are described as astigmatic beams. Note here that a beam ellipticity implies astigmatism, though the two terms refer to different characteristics of the beam. The difference in distance between the phase centers of the beam is measured by the term $\delta z_{x,y}$, using the notation presented in Jellema (2015). The z terms in equations (1.5)-(1.7) can be substituted for $z \pm \delta z_{x,y}$ for one axis in the case of astigmatic beams.

We also see that (1.4) can be separated into a scalar term and an exponential term. The scalar term is a normalizing factor such that the integrated power in the beam adds to unity. The exponential term can be broken down further into real and imaginary terms. The real parts of the exponential term describe the amplitude behavior of the beam, and the imaginary parts of the exponential term describe the phase behavior of the beam. Looking first at the real (amplitude) terms of exponential

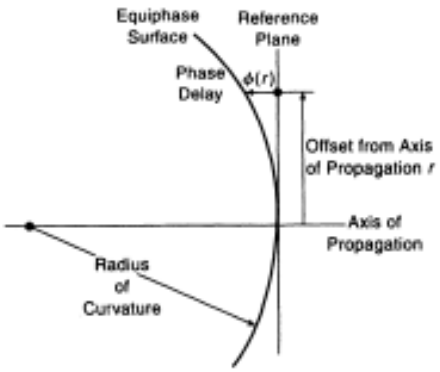

Figure 1.3. Representation of the phase terms of equation (1.4) as referenced to a phane at z_{ref}. Figure reproduced from (Goldsmith 1998), with permission.

in equation (1.4), we see that the first term determines the shape of the Gaussian beam.

Looking towards the phase (imaginary) exponential terms, the spherical phase fronts are described by the phase front R, which measures the the distance between the phase center and the reference plane at z_{ref} along the optical axis. The terms $R_x(z)$ and $R_y(z)$ describe the phase radius of each component of the wave in the xz and yz planes, respectively. Note that the phase surface in the plane at z_{ref} is only equal to R_x at a single point, which is the center of the plane at $(x = 0, y = 0, z_{ref})$. Elsewhere in the plane $(x \neq 0, y \neq 0, z_{ref})$, the phase surface is delayed by the factor $\phi_x(x, z)$ and $\phi_y(y, z)$, as represented in figure 1.3.

The upper two panels of figure 1.4 shows an ideal Gaussian beam at the reference plane z_{ref} as viewed from a point further on the optical axis. In the ideal case $R_x = R_y \Rightarrow R_{x,y}$ and $\phi_x = \phi_y \Rightarrow \phi_{x,y}$. We would see the phase peak at this point with a symmetrical (spherical) roll-off as a function of distance $r = \sqrt{x^2 + y^2}$ from the axis.

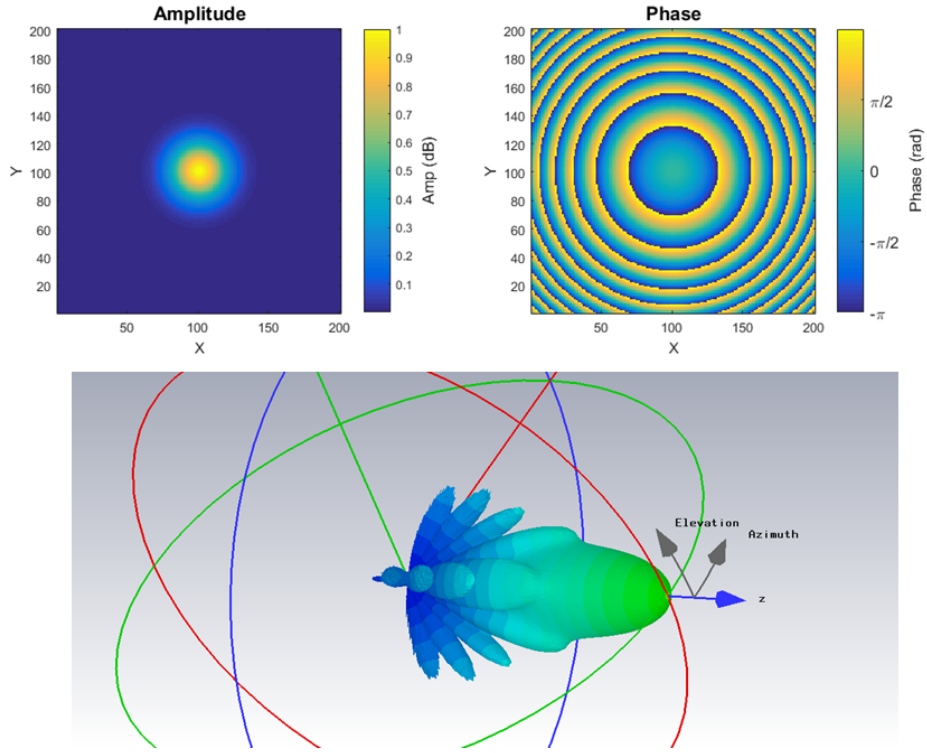

Figure 1.4. The upper two panels show the amplitude (left) and phase (right) of an idealized fundamental Gaussian beam produced using equation (1.4), both as viewed in a 2D plane perpendicular to the optical axis (i.e. from z_{ref}). The lower panel shows a 3D projection of a Gaussian beam in amplitude only (*CST Microwave Studio* 2016).

The plane shows concentric rings, where each ring shows a phase 'jump' from $-\pi/2$ to $+\pi/2$.

For Gaussian beams, there is a natural distinctive boundary between two regions closer and further from the beam. As seen in the amplitude (solid lines) in the lower panel of figure 1.2, close to the beam waist there is a region where the amplitude does not vary significantly as a function of distance, and the beam is roughly collimated. However, in that region, the phase of the beam is changing rapidly with z, beginning as planar at the beam waist and becoming more curved as the beam travels in z. At some distance, the phase reaches its maximum curvature, after which the propagating

beam spreads out and approaches a flat phase front. The location of the minimum radius of curvature is called the confocal distance, given by the equation

$$z_c = \frac{\pi {\omega_0}^2}{\lambda} \tag{1.8}$$

where z_c is the confocal distance.

In approximate terms, the near-field region of the beam is where the beam is roughly collimated in amplitude but varying widely in phase as a function of z, and the far-field region is where the beams begin to be consistent, well-defined, and approximated as plane waves. The distinction becomes important for radiation pattern measurements because the beam can behave very differently when measured in each region. However, there are advantages to measuring the beam in either the near field or far field as discussed in section 1.7.4.

There is no precise cutoff distance that distinguishes the near and far fields, but the confocal distance of Gaussian beams agrees with generally agreed-upon values (see Goldsmith 1998, section 2.2.4). A more rigorous explanation involves the reactive near-field, where the presence of evanescent modes dominates. Evanescent modes are solutions to the field function that do not propagate, and decay exponentially as a function of z. However, there is a region very near the radiating element (the reactive near field, $z \lessapprox \lambda$) where the signal contained in these fields is still significant enough that these modes affect the beam pattern.

Further into the near field, sometimes referred to as the Fresnel region, the beam is still diffracting with itself, causing rapid change in the waveform shape as a function of distance. This region is so named after the Huygens-Fresnel Principle, which states that each point on an arbitrary waveform is a secondary source of its own spherical waveform. To find the shape of a new, secondary waveform at some forward distance, the contribution of all points at the primary waveform must be summed for each

point on the secondary waveform, including amplitude decay and phase delay of each contributing wave along the propagation distance to the point on the secondary waveform. The diffraction caused by the interaction between all of the waveforms leads to significant change in the beam pattern as a function of distance. After some distance, these effects become negligible, and the far-field radiation pattern dominates.

1.6 Types of Radiation Pattern Measurements

Radiation patterns can be measured as intensity (measuring amplitude only, or total power) or as complex field patterns (amplitude and phase). Both types of measurements allow the data to be fit to a fundamental beam function and can determine the beam's pointing direction. The trade-off between the two types of measurements is the simplicity of experimental components with the accuracy to which the beam shape and pointing can be determined.

1.6.1 Intensity Measurements

An intensity measurement uses a single source scanned in front of the receiver. The source can be either a monochromatic or broadband (typically thermal) source. Thermal sources are relatively easy and inexpensive find, and are therefore the most common type of source probe used for intensity measurements. Thermal beam scans are useful in that they can be implemented and analyzed quickly to characterize the beam characteristics of the instrument. It may also be desirable to characterize a broadband detector with a broadband source to determine the behavior of the beam as it will be utilized in-situ (see discussion in Murphy et al. (2010)).

Thermal beam measurements can be made with either hot or cold sources. In the former case, the thermal source must be significantly hotter than the background environment so that the detector can measure an excess of photons radiating from the

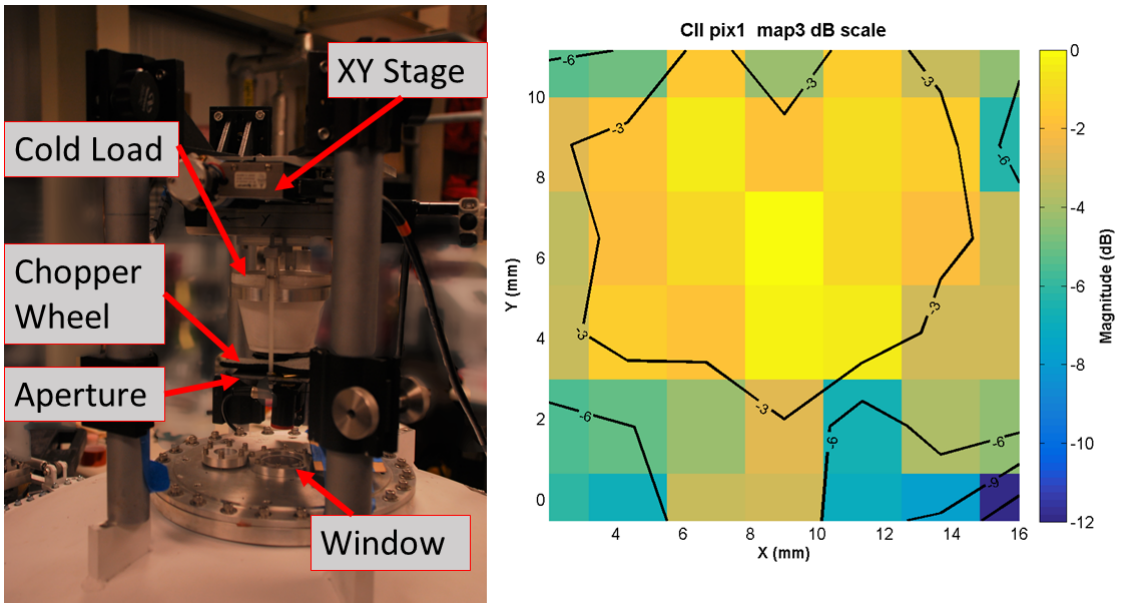

Figure 1.5. The right panel shows the beam scanning apparatus used to take thermal beam scans using a liquid nitrogen cold load with a aperture plate. A chopper wheel was mounted between the aperture plate and the bottom of the cold load. The Styrofoam cup is not very emissive at the frequency of observation ($\nu = 1.9$ THz) so an Eccosorb pad was placed in the cup. This particular measurement was made using a mixer-based detector in a bolometric mode, and the sensitivity to thermal changes was weak. The resulting beam pattern is therefore very coarse and suffers from significant noise. However, the aim of this measurement was to determine the position of the beam relative to the center of the cryostat window, and this measurement was sufficient to make that determination.

probe. In the latter case, a target submerged in a cold bath may be used as a source, and the detector measures an absence of photons radiating from the probe. In either configuration, if the detector's sensitivity to thermal changes is small, a chopper wheel can be inserted in the optical path. The chopper blade spins at a set frequency, and the detector output S is fed into a lock-in amplifier at the same frequency, which can boost the signal above the noise floor by several dB. The scanning system and beam pattern measurement taken for the STO-2 mission using a cold load configuration is shown in figure 1.5.

In order to fully constrain the boresight angle of a beam with power-pattern

measurements, at least two 2D planar scans must be taken at different different distances z_1, z_2 from the detector sub-assembly. If the scanning system moves exactly along the optical axis, the location of the beam maximum in each scan plane relative to the scanner system coordinates can be used to fit a line between the measurement planes, tracing the pointing direction. For a perfectly symmetrical beam, a pointing offset will make the beam appear progressively more elongated as the measurement plane moves further away from the focal plane. The same effect is measured when the scan plane is not normal to the beam axis, thus it is critical to ensure axial alignment of the scan system to the focal plane to measure the beam offset. Several techniques may be used for accurate alignment precision, such as optical alignment or very accurate mechanical alignment systems. A fundamental beam asymmetry will maintain a relative ellipticity over the successive scan planes, such that asymmetry can be distinguished from pointing offset if axial alignment is ensured.

Nyquist sampling theorem also limits the physical aperture of the source that samples the field. At the plane of measurement at distance z, the aperture of the source can not be larger than half of the e-folding diameter. As will be discussed in section 1.5, for a Gaussian beam this radius is $\omega(z)$, so the aperture of the source can be no larger than $\omega(z)/2$. Additionally, the source should resemble an isotropic radiator. For thermal sources this requirement can be made by placing the source behind an aperture plate.

1.6.2 Complex Field Measurements

The other beam pattern measurement technique is to measure the complex field parameters of the beam. The complex field parameter $\alpha \pm i\beta$ sampled over the

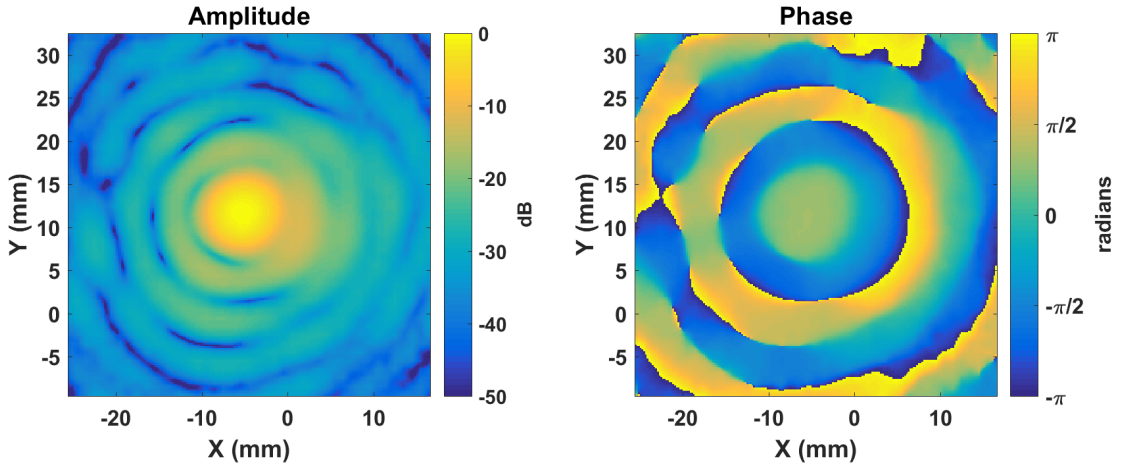

Figure 1.6. Example of a measured complex field pattern of a Gaussian beam receiver. The left panel shows the amplitude pattern and the right panel shows the phase pattern. The beam measured here is highly truncated at the aperture of the optical system, and suffers from diffraction effects that give rise to significant side lobe amplitude seen in the left panel.

scan plane can be translated into the amplitude and phase response of the receiver. Figure 1.6 gives an example of an amplitude and phase pattern measured from an astronomical instrument. A complex field measurement requires a coherent source, where the amplitude and phase of the time-varying electric field emitted by the source probe varies as a sinusoidal function over time. To measure a complex field parameter, the detector must respond to the change in amplitude of the incoming signal as a function of time, and $S(t)$ is recorded for a fixed duration. The peak in the FFT of the signal $S(t)$ is the complex field parameter. The full field pattern thus measures the electric field in the scan plane $\vec{E}(x, y, z)$, where the field E is a vector field by virtue of being complex valued. At low frequencies ($\sim$10-1000 MHz) a single coherent source with an output $\vec{E}(t) \propto \sin(2\pi f t)$ of may be scanned in front of a coherent receiver.

Though a detector chip can respond to the time-varying E-field oscillation at THz frequencies, the signal $S(t)$ is generally too fast to be recorded by commercially

available analog-to-digital converters. A solution is to use a heterodyne technique (Karpen and Mohr 1966), where two monochromatic, coherent sources are combined in front of the receiver system, generally with a simple thin-film beamsplitter or with a Fabret-Perot diplexer. The two sources are offset in frequency by a small amount Δf, one of which is scanned in front of the receiver at f_{RF} and the other is used as a stationary local oscillator (LO) at f_{LO}.

If the detector is a non-linear device, the detector will respond in such a way that the voltage output is modulated at different harmonics of the two input tones. If we choose the difference frequency to be within the response time of the detector, the voltage output of the device will be given by equation (1.9) (ignoring other mixer products) (Walker 2015b).

$$V(t) \simeq \sin(2\pi f_{RF} t)\sin(2\pi f_{LO} t) = \frac{1}{2}\cos\left[2\pi\left(f_{RF} - f_{LO}\right)t\right] - \frac{1}{2}\cos\left[2\pi\left(f_{RF} + f_{LO}\right)t\right] \tag{1.9}$$

where

$$f_{LO} = f_{RF} + \Delta f \tag{1.10}$$

All non-linear mixing devices have mixer products at both the upper $(f_{LO} + f_{RF})$ and lower $(f_{LO} - f_{RF})$ sidebands. Single sideband detectors are suppress one of these signals (usually the upper sideband), which is the most common receiver type. Double-sideband receivers that can record both the sum and difference frequency are preferred as they recover more of the input signal, though the receiver system is significantly more complex. In either case, the voltage output of the detector chip is a modulated signal at the lower intermediate frequency ($f_{IF} = \Delta f$). As one source is scanned in the optical path of the receiver, the amplitude and phase of the IF signal will change as a function of the receiver's beam pattern.

In the THz frequency regime, it is not often trivial to find two coherent sources, which add significant cost and complexity to the measurement apparatus. Source probe compensation techniques are possible for coherent measurements made close to the focal plane of the system (Leach and Paris 1973), (Paris, Leach, and Joy 1978), (Spang et al. 2010). With this compensation, the size of the aperture of the source probe can be larger than that required for incoherent beam scans.

However, these patterns offer several advantages over intensity beam measurements. Broadband measurements 'smear' out diffraction effects and standing waves because these frequency-dependent effects add incoherently in the optical path of the receiver, which can make side lobes appear larger or increase the overall noise level of the system. By measuring the complex field pattern at a monochromatic frequency, diffraction effects are present and so can be appropriately accounted for. Furthermore, most optical simulation software solves Maxwell's equations at discreet frequency steps, meaning they simulate the beam at one particular frequency. A monochromatic measurement is therefore the best comparison between the measurement and simulation.

Most importantly, a complex beam pattern is a more sensitive measurement of the fundamental beam parameters. By fitting in phase and amplitude, the measured pattern can be modeled in more degrees of freedom by a fundamental propagating function. We can see from equation (1.4) that amplitude-only measurements only fit for the first part of the exponential term, but complex fields can fit for the imaginary terms as well, which is an additional 4 degrees of freedom. This advantage is particularly useful for characterizing new detectors or feed types where it is desirable to directly compare a beam to its electromagnetic simulations.

1.7 Analysis Techniques Using Complex Field Measurements

A significant advantage to complex versus direct field measurements is that the intensity, beamwidth, and pointing direction are measured simultaneously, so only a single scan plane is required to determine basic beam characteristics. A single complex field pattern can be propagated and recreated at any plane along the optical axis, and so the scan can be conducted at arbitrary planes in the optical path, including in the near-field. This way, the beam pointing direction can be found by propagating the beam mathematically, rather than by measuring it in multiple separate planes as with intensity measurements. Complex or compact optical systems may only have one plane accessible to a beam scanning system, and thus being able to characterize the beam from a single scan plane is ideal.

Limitations in source probe output power at THz frequencies make it very difficult to achieve full end-to-end optical system characterization including a telescope's primary and secondary mirror. For example, let us use the definition of the far-field boundary in (1.8) but replace ω_o with D, the diameter of a telescope's primary mirror. For a telescope with a 1-meter primary operating at a wavelength of $\lambda = 1\text{mm}$, the far-field boundary occurs at 1 km away from the telescope aperture. Typical output power of source probes in this regime are not adequate to overcome the atmospheric attenuation at such long distances, making this measurement impractical from a technological as well as experimental configuration standpoint.

Though a single complex beam scan can characterize an instrument's sensitivity pattern, pointing direction, and coupling efficiency, higher-level information can be extracted for full beam characterization by conducting two sets of measurements at two scan planes using a singly polarized source probe. Two sets of scans are conducted

each at distance z_1 and $z_2 = z_1 \pm \frac{\lambda}{4}$, where the choice of z can be located either in the near- or far-field of the instrument. The quarter-wave offset in distance can be used to correct for optical standing waves introduced between the between the source probe and the optical system (i.e. standing waves between the source probe and cryostat). At each plane, after the first measurement the source probe is rotated by 90° and the beam pattern is re-measured, which can later be used to fit for the co- and cross-polarization axis of a receiver beam. Each of these techniques will be discussed in detail below.

1.7.1 Standing Wave Reduction

The principle used in this dissertation to remove standing waves can, to first order, eliminate the effects of optical standing waves throughout the optical system by virtue of the principle of linear superposition. In post-processing of the data from the two scan planes z_1 and z_2, we effectively cancel the standing waves using the equation 1.11

$$\vec{E}_{comp} = \frac{\vec{E}(z_1) + \vec{E}(z_2)e^{\pm\frac{i\pi}{2}}}{2} \tag{1.11}$$

where $\vec{E}(z_1)$, $\vec{E}(z_2)$ are the complex fields measured at each scan plane, and $\vec{E}_{comp}$ is the compensated field. The exponential term will be negative for z_2 further from the receiver than z_1, and positive otherwise. When the two maps are co-added, a wave traveling parallel to the optical axis will have a phase shift of $\frac{\pi}{2}$, but a standing wave, traveling twice the distance, will have a phase shift of π. These waves will cancel while the primary beam is simply averaged together. $\vec{E}_{comp}$ can be used for further post-processing. A more detailed description of this technique can be found in Jellema 2015.

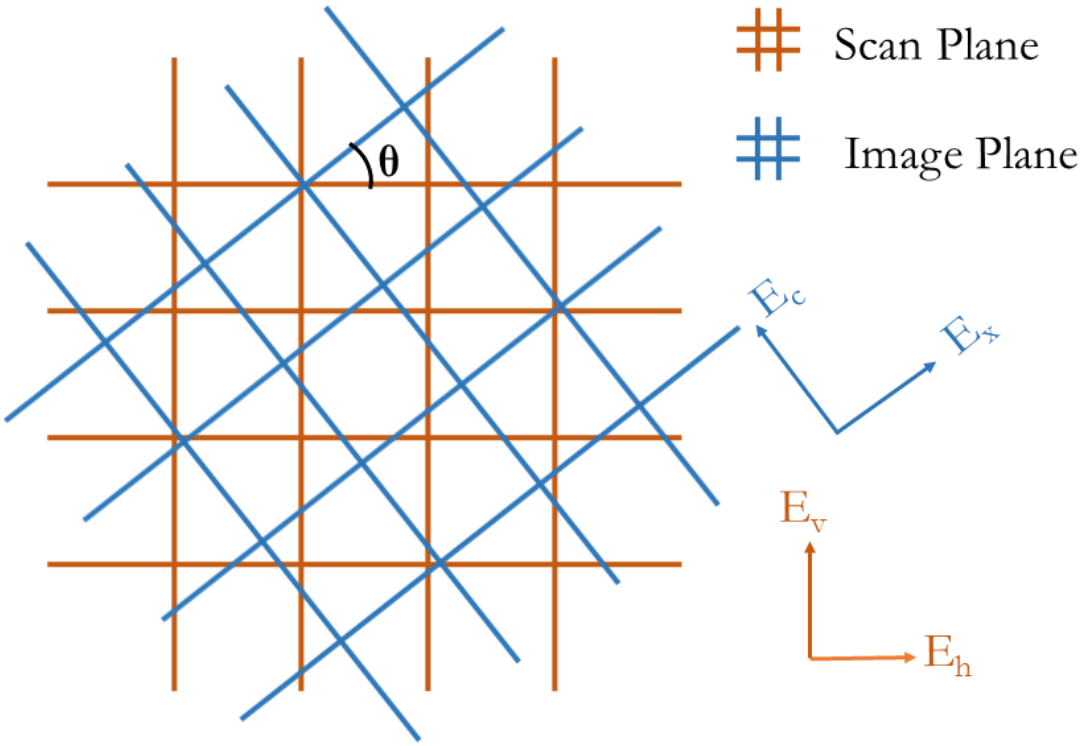

Figure 1.7. Example of a scan plane recorded at an arbitrary polarization orientation with respect to the co- and cross-polarization orientation of the instrument. A complex field measurement allows the measured scan plane to be rotated mathematically, and a fitting function can rotate the scan plane until the signal in the cross-polarization field is minimized.

1.7.2 Polarization

For either single or dual-polarization selective pixels, it is important to distinguish the co- and cross-polarization component of the beam pattern to accurately fit for the fundamental beam parameters. In principal, the co- and cross-polar beam pattern can be measured with only two scans at orthogonal polarizations of a singularly-polarized source probe. This is generally true for both intensity and complex field measurements,

though for intensity measurements the source probe must be precisely aligned with each of the field components, which may be unknown. The advantage of complex field measurements is that the source probe can be aligned in any orientation with respect to the actual co- and cross-polarization axis of the detector beam, and the exact co- and cross-polarization axes are fit for each pixel individually in post-processing.

During the measurement, the scanned source is first mounted with the polarization aligned to one principal axis of the stage. The resulting measurement is the field pattern $\vec{E}_h$, where the subscript denotes the measurement is made with the source probe at a particular polarization (here h is used to identify a horizontal polarization, though the source probe polarization alignment can be arbitrary). The source is subsequently rotated by 90° on a high-precision rotary stage before mapping $\vec{E}_v$. In post-processing, the measured fields can be projected onto arbitrary axes, and a minimization algorithm can be applied to solve for the transformation that minimizes power in the cross-polar field $|\vec{E}_x|$. The orthogonal axis is thus the co-polar field component $\vec{E}_c$. Figure 1.7 shows a simple illustration of this transformation. This technique allows straightforward measurement of the fields $\vec{E}_h$ and $\vec{E}_v$ without time-intensive calibration between the scan plane and image plane. By doing so, we fit the fields $\vec{E}_c$ and $\vec{E}_x$ for each pixel independently across the focal plane. The transformation is a simple matrix rotation of the two fields by a rotation angle θ, which can be described by the equation: .

$$\begin{bmatrix} \vec{E}_c \\ \vec{E}_x \end{bmatrix} = \begin{bmatrix} \cos(\theta) & \sin(\theta) \\ -\sin(\theta) & \cos(\theta) \end{bmatrix} \begin{bmatrix} \vec{E}_h \\ Ae^{i\phi}\vec{E}_v \end{bmatrix} \tag{1.12}$$

Assuming a low cross-polarization magnitude, the coupling between the source probe and the detector will be greater for the probe orientation more aligned to the co-polarization axis, and the absolute power contained in one axis ($|\vec{E}_h|$) will be

higher than the other ($|\vec{E}_v|$). The term $Ae^{i\phi}$ scales the two maps relative to each other to correct for this effect, as well as correcting for system drifts between the two measurements. Here A is the amplitude scale factor and ϕ is a relative phase offset between the two measurements $\vec{E}_h$ and $\vec{E}_v$. The values of A and ϕ are calculated for each transformation angle θ using a Nelder-Mead minimization function with initial guess values taken from the center of each measurement, such that $A_{guess} = \mathrm{Re}[\vec{E}_h(x, y = 0)] - \mathrm{Re}[\vec{E}_v(x, y = 0)]$ and $\phi_{guess} = \mathrm{Im}[\vec{E}_h(x, y = 0)] - \mathrm{Im}[\vec{E}_v(x, y = 0)]$.

1.7.3 Beamfitting

Section 1.5 presented an overview of Gaussian beam formalism, and this section will describe the technique to fit a radiation pattern measurement to equation (1.4). This is achieved by calculating the degree of coupling between the measured complex field $\vec{E}_m$ (possibly after processing detailed above) to an idealized beam $\vec{E}_{ideal}$ by equation (1.13)

$$c_{00} = \frac{\iint \vec{E}_{ideal}\vec{E}_m^* dxdy}{\iint \sqrt{\vec{E}_{ideal}^2} dxdy \iint \sqrt{\vec{E}_m^2} dxdy} \tag{1.13}$$

where $\vec{E}_{ideal}$ is the result of equation (1.4). The beamfitting algorithm initiates $\vec{E}_{ideal}$ using the designed of parameters $\omega_{o,x}, \omega_{o,y}$ at the nearest focal plane and propagates the idealized beam forward to z_m, the measurement plane. Gaussicity is the maximum fraction of coupled power into a fundamental Gaussian beam which best approximates the measured field. Gaussicity η can be calculated from the coupling parameter by $\eta = |c_{00}|^2$. The coupling loss between the measured beam and the idealized beam is this value subtracted from unity, or $\epsilon = 1 - \eta = 1 - |c_{00}|^2$.

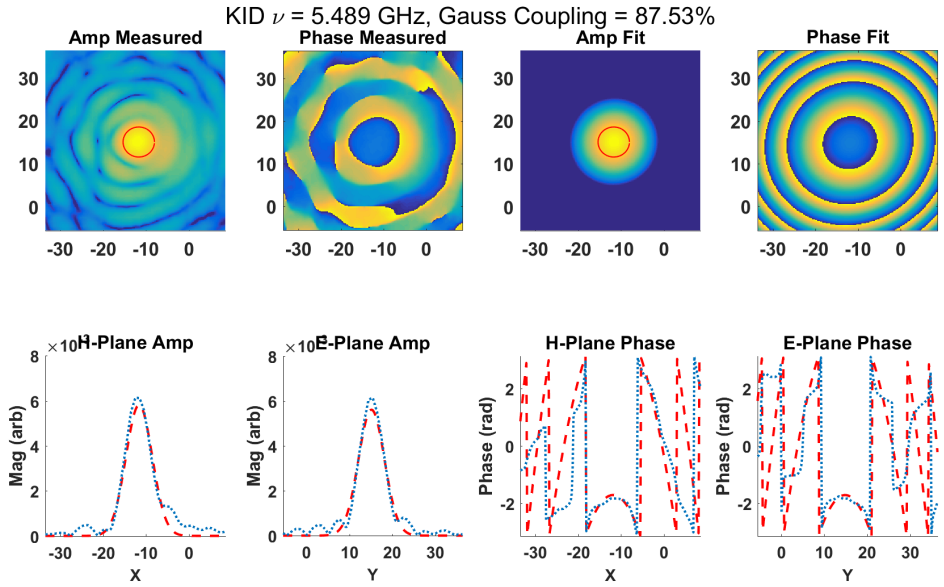

Figure 1.8. Comparison between a measured near-field beam pattern and the Gaussian beam ψ_{00} produced by equation (1.4). The upper panels show the 2D data and the lower panels show 1D cuts in the E- and H-plane. The blue dotted lines are the measured data and the dashed red lines are the fit data. The red circle in the upper two amplitude panels indicates the FWHM beam width.

If instead we do not assume the beam parameters $\omega_{o,x}, \omega_{o,y}$ and want to fit for the values $\omega_x(z), \omega_y(z)$, we can search the parameter space using a minimization function operating on the coupling loss parameter ϵ. The minimization function uses 'seed' values as initial guesses of the beam parameters, computes the value of $\vec{E}_{ideal}$ from these values, propagates the beam forward to the image plane, calculates the coupling loss coefficient between the measurement and fit data, and iterates over the parameter space until a convergence criteria is met. Figure 1.8 shows a comparison between an example of a measured beam pattern and the best-fit beam produced with this technique.

The minimization function can be specified depending on the degree of freedom given to the search criteria. An unbounded Nelder-Mead (Nelder and Mead 1965)

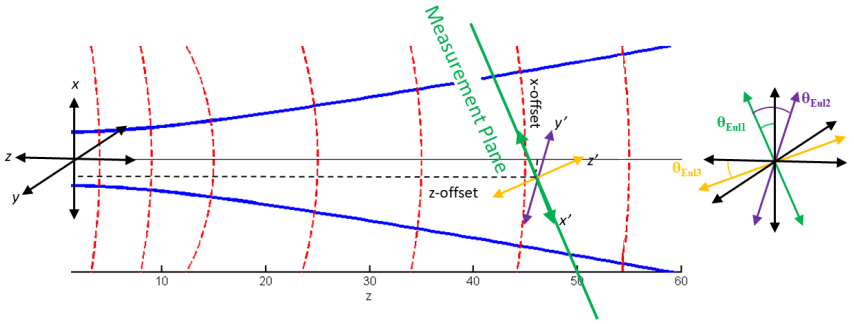

Figure 1.9. Demonstration of a Gaussian beam in a reference frame x, y, z, and a measurement plane with a misaligned coordinate system x', y', z'. The idealized Gaussian beam parameters must be transformed from the x', y', z' to the x, y, z system before the overlap integral can be performed. The blue lines show the beam amplitude, and red dashed lines show the spherical phase fronts. The primed and unprimed coordinate systems are shown in relation to their origin and are also superimposed to the right of the beam diagram.

minimization function can efficiently probe the parameter space and has a low chance of getting stuck into local rather than global minima. Chapter 3 takes the output parameters of that function to use as an initial guess for a non-linear least-squares minimization function (Marquardt 1963), which is also unbounded. The least squares algorithm allows us to more easily find the confidence intervals for the solution set of beam parameters.

It is important to note that the radiation pattern is measured relative the axis from the center of the coordinate system set by the measurement plane, which may not be along the principle axis of the receiver if there are lateral or rotational offsets between them. These offsets will skew the measurement plane relative to the image plane and can cause a beam to appear astigmatic or asymmetrical if not properly accounted for. One way to correct for this is to very precisely align the coordinate system of the scan plane to the optical axis of the receiver. Doing so requires high precision metrology of the apparatus prior to the measurement. However, as was

shown with Jellema (2015), the frequency dependence of the optical behavior of a system can cause apparent misalignments in a beam scanning system, even if properly aligned using laser metrology.

A better course of action adopted in this dissertation is to mathematically fit for the lateral and rotational offsets of the scanner system with respect to the optical plane. In the beam fitting algorithm, following the example set forth in Jellema (2015), an idealized beam is initiated in an arbitrary coordinate system with lateral offsets $x_{off}, y_{off}, z_{off}$ and rotated by $\theta_{Eul1}, \theta_{Eul2}, \theta_{Eul3}$ with respect to the scan plane. This new coordinate system x', y', z' is used to propagate an idealized, fundamental Gaussian beam ψ_{00}. The angles $\theta_{Eul1}, \theta_{Eul2}, \theta_{Eul3}$ are Euler-rotation angles (Piovan and Bullo 2012). Figure 1.9 shows the coordinate system transformation described here.

1.7.4 Near-Field to Far-Field Transformation

One advantage of complex field radiation pattern measurements is the ability to propagate the measurement plane either forwards or backwards through optical elements to arbitrary planes along the principle axis. This is especially helpful for the ability to transform a measurement from the near-field into the far-field, and vice versa. A few phase-less measurement techniques have been demonstrated to solve for the far-field antenna pattern from near-field data, but these techniques are either susceptible to finding erroneous solutions or require additional measurement planes (Isernia, Leone, and Pierri 1996), (Tkadlec and Nováček 2005).

There are two methods used to perform a near-to-far field transformation. The first is based on a Modal Expansion technique as described in Balanis (2005). The

second technique is based on the angular plane wave spectrum representation (APWS) (Novotny, Frimmer, and Reimann 2016), (Teyssier et al. 2008), (Tong et al. 2003), (Tervo and Turunen 2002), (Hollis and Ecker 1973) and will be described here. Though the APWS method of beam propagation is a highly accurate and representative, it is still only an approximation, in the same way a Fourier transform approximates an original function.

The APWS technique is analogous to a 2D Fourier transform converting a timeseries measurement to a frequency. In a 1D Fourier transform, a function is represented by an infinite series of sine (or cosine) functions. The sine functions each have an independent magnitude, frequency and phase offset, and the superposition of the infinite series of sine and cosine functions approaches a perfect description of the original function. For the 2D case, rather than breaking up a function into a infinite series of sines and cosines, the function is broken down into an infinite series of plane waves. The series of plane waves is the Fourier transform of the near-field measurement $\vec{E}_{nf}$, and the series is represented by the variable $\vec{A}$, after the Angular Plane Wave spectrum method (though in some sources it may be referred to as $\hat{E}$, as is common to designate a Fourier pair).

We perform a 2D FFT of the complex field $\vec{E}_{nf}$ measured in the near-field to find the APWS using the equation

$$\vec{A}(k_x, k_y) = \frac{1}{(2\pi)^2} \int_{-\infty}^{\infty} \int_{-\infty}^{\infty} \vec{E}_{nf}(x, y, z = 0) e^{-i(k_x x + k_y y)} dx dy \tag{1.14}$$

The field $\vec{E}_{nf}$ contains all the information about how a beam's sensitivity, pointed along the optical axis $\hat{z}$, varies as a function of spatial coordinates across the plane. In the reciprocal space, the Fourier field $\vec{A}$ contains the information of the beam's sensitivity as a function of angle, and all of the plane waves are co-aligned at the origin. From an optics standpoint, the field $\vec{A}$ represents the pupil plane (aperture) of

an optical system, where each point in the object plane fills the aperture, but has an individual pointing direction.

In the spectrum, all of the plane waves share the same wavelength (frequency), but each wave is pointed in a different direction and has a different vector length, proportional to the magnitude of the field in that direction. An individual wave is described by its propagation vector $\vec{k}$, which is pointed in the direction of propagation, which is normal to the plane, and has units of $^1/_{\mathrm{m}}$. The individual propagation vector can be projected onto a set coordinate system, so the pointing direction of each plane wave can be referenced to the original coordinate axis. We can then describe the propagation vector using $\vec{k} = k_x\hat{x} + k_y\hat{y} + k_z\hat{z}$, where the angle defined by $\tan(^{k_y}/_{k_x})$ describes the pointing angle of the beam, and k_z represents the propagation along the $\hat{z}$ axis (more later).

The angular resolution (the wavenumber spectrum points) of the plane waves making up $\vec{A}$ is dependent on the sampling of the $\vec{E}$ field in the measurement plane. From a sampling of the complex field over the $\hat{x}$ and $\hat{y}$ coordinate system at regular grid spacing of dx and dy, we can construct a grid of $M \times N$ points such that $-\frac{M}{2} \leq m \leq \frac{M}{2} - 1$ and $-\frac{N}{2} \leq n \leq \frac{N}{2} - 1$. Nyquist sampling theorem places an upper limit on the spacing of the grid points dx, dy of $^\lambda/_2$ in order to properly reconstruct the field. The extent of the sampling plane M, N is typically reaches at least -30 dB from the amplitude maximum of the beam.

The values of the wavenumber spectrum points (angles) on the grid in Fourier space are:

$$k_x = \frac{2\pi m}{Mdx} \tag{1.15}$$

$$k_y = \frac{2\pi n}{Ndy} \tag{1.16}$$

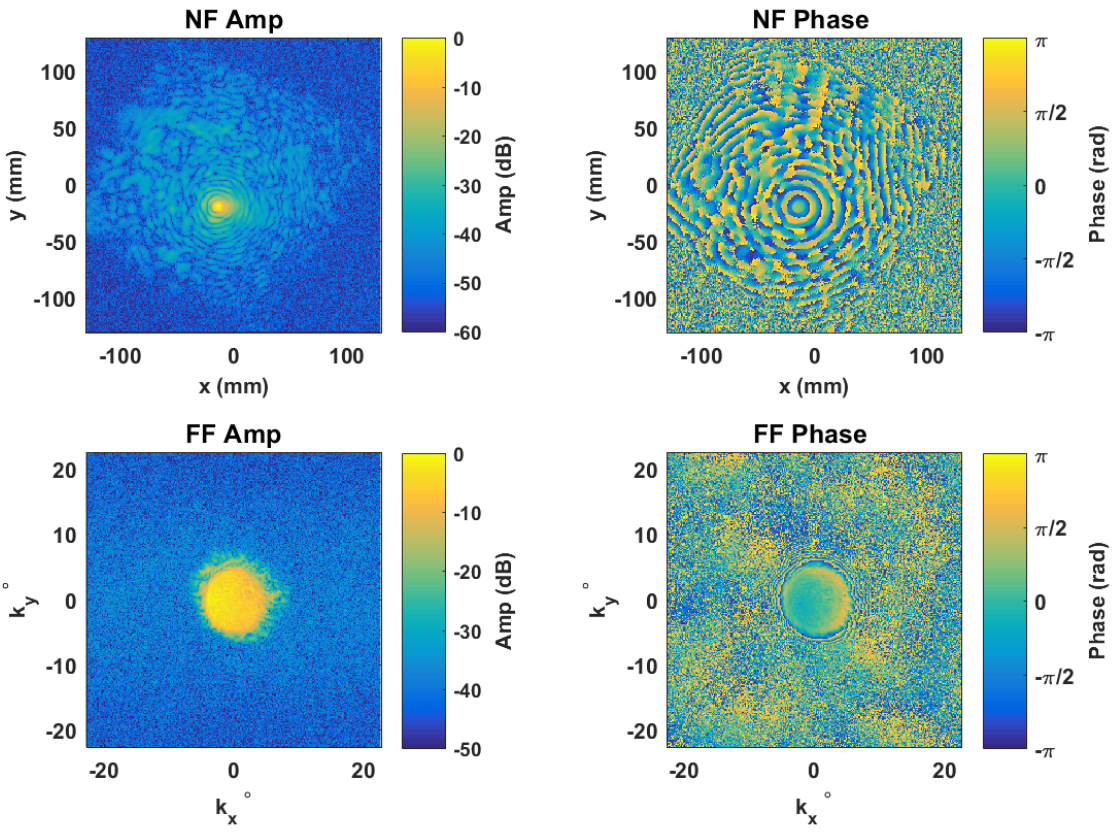

Figure 1.10. The upper two panels show the amplitude (left) and phase (right) of $\vec{E}_{nf}$ and the lower two panels show the transformed field $\vec{A} = \vec{E}_{ff}$. This figure uses the same dataset that will be the subject of chapter 3.

In some references, because of the analogy to 1D Fourier transforms between time domain sampling and frequency, the coordinates are referred to as 'spatial frequencies', though this can lead to some confusion because we ignore temporal dependence in the plane wave representation. So when viewing the field $\vec{A}(k_x, k_y)$ in a 2D map, the value of $|\vec{A}|$ is proportional to the intensity of the wave at each grid point (k_x, k_y), where each grid point represents the angle or pointing direction $\tan(k_y/k_x)$ across the 2D plane. Figure 1.10 shows a comparison between the near-field and APWS-fields.

So far we have only discussed the plane wave spectrum as a stationary field, located at the measurement plane. We now consider the z dependence of the spectrum. This

is represented by the $k_z\hat{z}$ term in the propagation vector $\vec{k}$. In order to propagate the plane wave spectra to an arbitrary plane located at $z \neq 0$, the field must be multiplied by a propagation factor $e^{\pm ik_z z}$ such that

$$\vec{A}(k_x, k_y, z) = \vec{A}(k_x, k_y)e^{\pm ik_z z} \tag{1.17}$$

where

$$k_z = \pm\sqrt{{k_o}^2 - {k_x}^2 - {k_y}^2} \tag{1.18}$$

and

$$k_o = \frac{2\pi}{\lambda} \tag{1.19}$$

In order to satisfy the Helmhotz equation, the two solutions for $\pm k_z$ from equation (1.18) must be superimposed. The first solution is for $+k_z$, which represents plane waves propagating (radiating) forward to $z > 0$. The second solution is for $-k_z$, which represent evanescent waves which radiate into the hemisphere $z < 0$. In the forward direction, these waves decay, and asymptotically approach zero magnitude well before reaching $\sim z_c$.

In order to propagate the APWS spectrum from $z = 0$ to an arbitrary measurement plane at $z \neq 0$, we multiply the spectrum $\vec{A}$ by the correct propagation factor for the direction we want to propagate. We can then re-create the field at the new plane plane with an inverse FFT:

$$\vec{E}(x, y, z) = \frac{1}{(2\pi)^2}\int_{-\infty}^{\infty}\int_{-\infty}^{\infty}\vec{A}(k_x, k_y)e^{\pm ik_z z}e^{-i(k_x x + k_y y)}dk_x dk_y \tag{1.20}$$

From equation (1.20) we see that the APWS field (the Fourier transform of the $\vec{E}$ field in the measurement plane) is sufficient to describe the field at all points in the (x, y, z) coordinate space.

In the special case of being interested in propagating to the far-field at $z \to \infty$, we can take advantage of the Method of Stationary Phase to find a shorthand solution

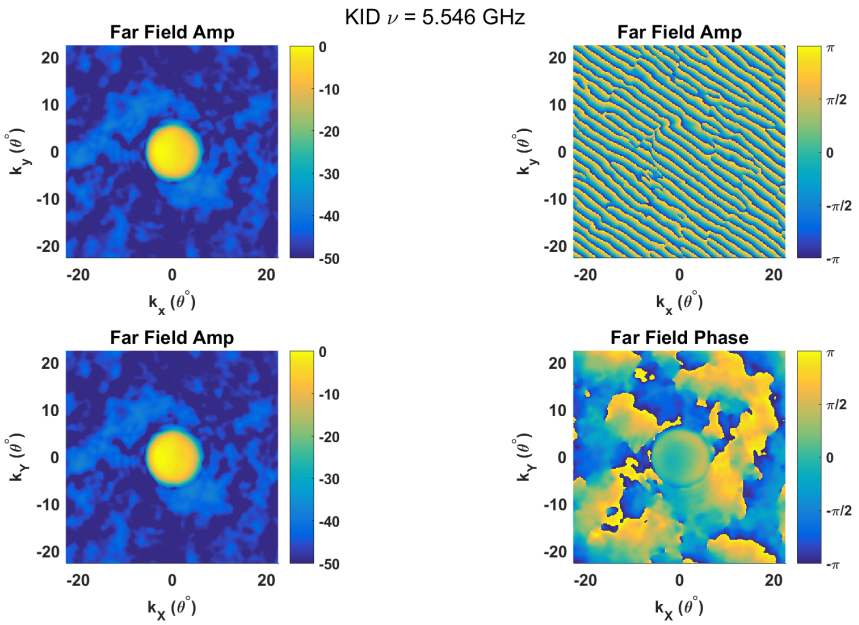

Figure 1.11. An example of applying the phase correction of equation 1.21 to a far-field transformation. The right two panels show the amplitude projection which remains constant, and the left two panels show the phase transformation. The top left panel shows the phase of the plane wave spectra as viewed edge-on, and the lower left panel shows the phase when viewed after shifting the phase angle to align with the projection axis.

for the far-field $\vec{E}(x, y, z \to \infty)$. A rigorous description of this method can be found in Born and Wolf (1994) but is outside the scope of this dissertation. The method of stationary phase makes the approximation that as the beam diverges from the near field, in the very far-field the plane waves from all other pointing directions cease to influence the point in question (x, y, z). Thus at $z = \infty$, the field point is only influenced by a single plane wave from the near field. All of the other plane waves destructively interfere and cancel each other by the time they reach the far field. The effect of this approximation is that the Fourier transform of the near field measurement becomes the far-field radiation pattern $\vec{E}(x, y, z) \approx \vec{A}(k_x, k_y)$.

If the near-field measurement includes data from an array instrument with many beams, the amplitude maximum of any non-central beam will not be in the center of the measurement plane. Because of this, the transformation will propagate from the center of the scan plane rather than the center of each beam, and the initial far

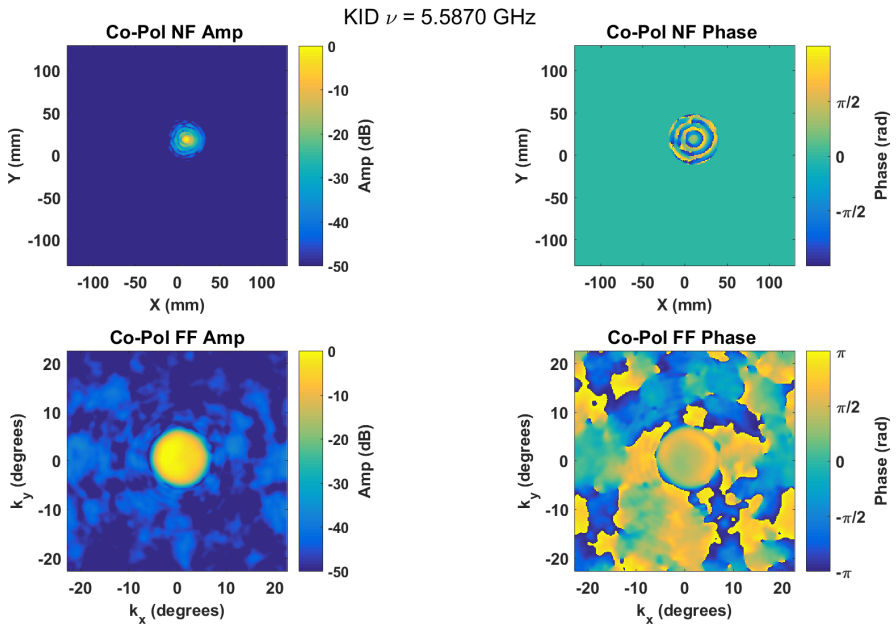

Figure 1.12. The upper two panels of this plot show a full 2D planar scan of a 880-pixel focal plane array. Data was recorded individually for each pixel, and the near-field data in amplitude (right) and phase (left) from a representative pixel is shown. A 2D Hanning window centered on the amplitude maximum of the near-field beam is applied in the upper two panels of this figure. The lower two panels show the far-field transformation. Any residual diffraction is likely an artifact of the optical system of the array and not from the analysis pipeline.

field transformation will show an edge-on view of a plane wave pattern which appears 'striped'. We mathematically correct for this projection by shifting the phase by the equation

$$\vec{E}_{ff} = \vec{E}_{ff} * \exp\left[i\left(k_x x_o + k_y y_o + k_z z_o\right)\right] \tag{1.21}$$

where (k_x, k_y, k_z) are the coordinate axis in the far field and (x_o, y_o, z_o) are the coordinates of the central peak found in the near-field, with $z_o = 0$. The effect of this phase shift is to re-center the k-space coordinate system at the amplitude maximum before transforming into the far field. The effect of this shift can be seen in the two right panels of figure 1.11.

Additionally, we can use spatial filtering techniques in the near-field measurements to remove truncation effects in the far-field pattern. Though a single pixel measurement will end sufficiently in the noise floor of the radiation pattern, for focal plane array measurements significant off-axis signal, such as stray light reflections in the device substrate, can produce a diffraction pattern in the far-field transformation. We can reduce this effect by applying a circularly-symmetric spatial mask to the near-field data. Figure 1.12 shows the near-field data from a single pixel in an array with the spatial mask applied to the near-field data. The far field data has had the phase correction of (1.21) applied.

Chapter 2

DEMONSTRATION OF A SINGLE-PIXEL MKID COMPLEX BEAM PATTERN MEASUREMENT

Abstract

As was discussed in the previous chapter, complex-field radiation pattern measurements can characterize an astronomical instrument in more parameters or figures-of-merit than can incoherent beam pattern measurements. For THz astronomical instruments based on incoherent detectors, such as Microwave Kinetic Inductance Detectors (MKIDs), or Transition Edge Sensors (TESs), most instruments have only used intensity mapping techniques by necessity, since MKIDs or TESs do not inherently record phase information from the incoming signal.

Both of these detector types rely on a fundamentally different read-out scheme than their heterodyne counterparts. In a TES, a photon that hits a tiny, superconducting bolometer sitting in a thermal bath at a constant temperature T_c, causes the detector to transition from superconducting to normal material. When it does so, the bias electronics record a change in voltage proportional to the change in temperature of the detector. In order to read out hundreds of pixels across the array, each pixel is sampled at a different time t in a cycle across all pixels, which is referred to as time-domain multiplexing. However, this process is slow and is not scalable to very large arrays if the time to sample all pixels across the array starts to become slower than the response time of the detector.

A relatively new read-out scheme was developed for MKID arrays. Instead of being sampled individually in time, each pixel is capacitively coupled to a transmission line at an individual frequency. The read-out electronics generate a tone at the coupling frequency of each pixel. When a photon hits the LRC circuit of a MKID, the kinetic inductance of the superconducting device changes, which causes a phase shift in the tone coupled to the transmission line (read-out line). This process is called frequency domain multiplexing. The sampling frequency of each pixel is then determined by the sampling rate of the ADC in the backend of the read-out electronics, and can be scaled to arrays of thousands of pixels and used with devices that have fast response times. Because of this success, some newer TES arrays have incorporated frequency domain multiplexing schemes.

Particularly for TES and MKID detectors with frequency-domain multiplexing systems, the fast read-out time can be utilized to make a complex field radiation pattern measurement technique. This chapter describes a proof-of-concept demonstration on how to set up a measurement system to record both amplitude and phase response of a single MKID pixel in an astronomical instrument. These are the first results of complex field radiation pattern measurements of direct detectors, though a similar two-source measurement system was used to record the coherence sensitivity of MKIDs in (C. Thomas and Withington 2012).

Complex field beam patterns require sampling of the E-field of a receiver in both amplitude and phase. MKIDs have no inherent phase response to incoming radiation and are thus classified as direct detectors. We map the amplitude and phase patterns of the detector beam profile by adapting a two-source heterodyne technique. The testing strategy recovers the E-field phase information by creating a reference signal to trigger data acquisition. At each x, y point in the scan plane, a timeseries recording of the total power incident on the MKID array at a set phase point in the reference signal is triggered, such that the phase

offset between the reference and acquired signals is proportional to the phase response of the receiver beam. The reference is generated by mixing two slightly offset low frequency signals from the output of the synthesizers used to drive two coherent sub-mm sources.

Of note here is that in other literature, a 'receiver' generally refers to a particular type of detector (the device that converts photons into current); namely, one based on a heterodyne mixer principle. Therefore, heterodyne devices such as Superconductor-Insulator-Superconductor (SIS) mixers or Hot Electron Bolometer (HEB) mixers, which both naturally record amplitude and phase, are referred to as receivers. A 'detector' then generally refers to a device that just responds to total incident power, so MKIDs and TESs are considered detectors. However, these terms are imprecise, and as this chapter points out, sensitivity to phase is not a property of the chip, it is more correctly a property of the entire electrical scheme to record voltage signals per pixel. This dissertation will continue to refer to a 'receiver' as a subset of components that make up an astronomical instrument (generally, a detector chip, optical feeding element, and the possible addition of mirrors, lenses, and apertures excluding the telescope primary or secondary mirrors), and will refer to a detector as any device type that actually performs the conversion of photons into voltage signals. This convention makes it easier to distinguish between different levels of component assembly, especially when referring to properties applicable to both mixing and incoherent detectors, though I apologize in advance for any confusion.

2.1 Background

MKID detectors measure the change in kinetic inductance of a superconducting resonator upon photon absorption, causing a detectable phase shift in the detector

readout (Day et al. 2003),(Zmuidzinas 2012), (Baselmans 2012). This process is sensitive only to the total power of the incident electric field, and therefore KIDs are incoherent detectors. Typical beam pattern characterization thus relies on scalar (amplitude only) detection of a source scanned in the main beam of the receiver (S. Yates et al. 2014), most often with a thermal source and optical chopping. The advantage of these systems is that they are low-cost and easy to implement.

A coherent beam measurement characterizes the beam emerging from the last optical element in the chain, and that beam is influenced by all optical elements preceding it. If the optical system is characterized well enough (i.e. amplitude and phase distortion per element), a coherent beam scan can differentiate between errors in the fundamental beam provided by the detector, alignment errors in the optical system, or misalignment of the beam measurement system to the optical axis (Teyssier et al. 2008), (Jellema 2015), (Naruse et al. 2009). Furthermore, measurements of the complex field parameters are required to de-convolve the beam produced by the source probe from the measured field, which is common practice when available. Phase measurements allow for compensation of standing waves and multiple reflections in the optical system, which are common and usually a dominant source of error for beam pattern measurements of heterodyne detectors.

2.2 Methodology

The strategy we developed to measure complex beam patterns of MKID detectors is based on heterodyne receiver characterization. In general, this technique requires at least one monochromatic, coherent source to illuminate the receiver; for amplifier-

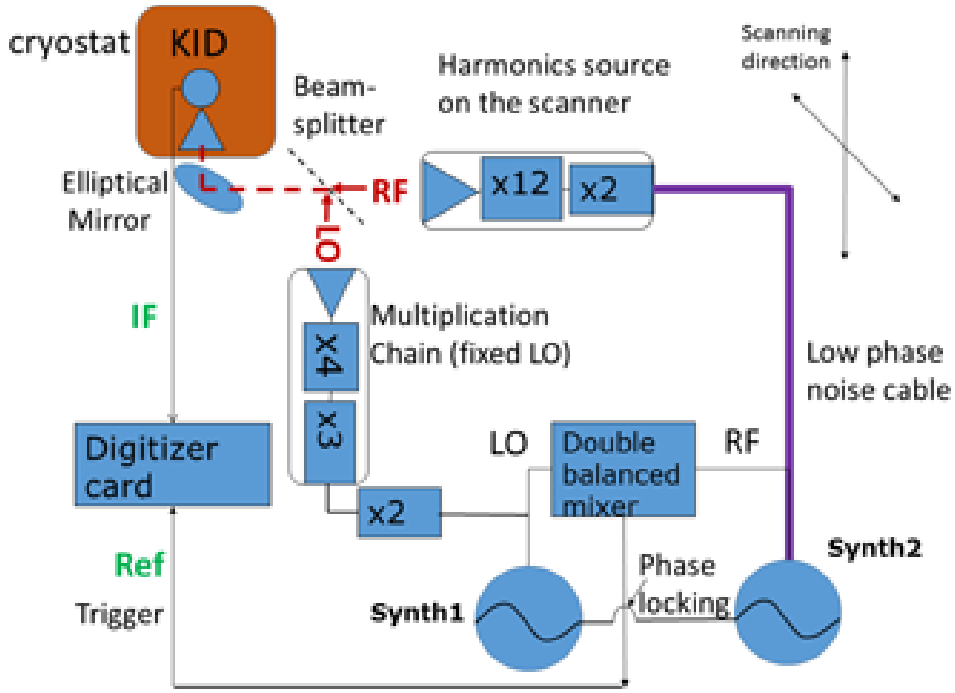

Figure 2.1. Schematic of complex-field measurement system for single MKID pixel demonstration. The high frequency RF is labeled in red and the low frequencies are indicated in green.

Table 2.1. Experiment System Frequencies

Location	f
Synth1	14.166500000 GHz
Synth2	14.166500400 GHz
RF	339.995009600 GHz
LO	339.995000000 GHz
IF	9600 Hz
Ref	400 Hz

List of the frequencies used for the heterodyne beam scanning system outlined in figure 2.2

based detector systems, only one source is necessary, but for mixer-based detectors a second coherent, source is used. This second source is referred to as the local oscillator (LO). The LO may be injected optically by a beamsplitter located in the optical path of the receiver, or may be injected directly (for example, through a waveguide port in the detector block). For this particular demonstration using a MKID, we employ a two source technique with quasi-optical LO injection shown in figure 2.1.

In principle, the source signal can be scanned in front of the MKID in a planar, cylindrical, or spherical pattern. The results we present here are based on 2D planar scans. The amplitude and phase response of the detector changes as a function of position of the source probe. Typically only relative measurements are of interest, so the scan data is normalized by a set point in the measurement, usually the grid center. Phase and amplitude maps as a function of position define the beam pattern of the device under test (DUT). The frequencies used in this demonstration are shown in table 2.1. A more detailed description of the heterodyne measurement theory can be found in Yaghjian (1986) and Hollis and Ecker (1973).

The LO and source probe are offset in frequency by a small value δf, and are quasi-optically coupled together with a beamsplitter in the foreground of the receiver. The LO is kept stationary while the source signal is mounted on an X/Y motion stage. The received signal at the detector is modulated at the difference of the two frequencies, according to equation (2.1), where we ignore terms outside the detector read-out bandwidth.

$$S_{RO}(t) \propto \frac{|\vec{E}_{source}|^2}{2} + \frac{|\vec{E}_{LO}|^2}{2} + |\vec{E}_{source}||\vec{E}_{LO}| \cos\left[2\pi \left(f_{source} - f_{LO}\right) t + \delta\phi\right] \quad (2.1)$$

In this equation S_{RO} is the timeseries signal of the detector, $|\vec{E}_{source}|$ and $|\vec{E}_{LO}|$ are

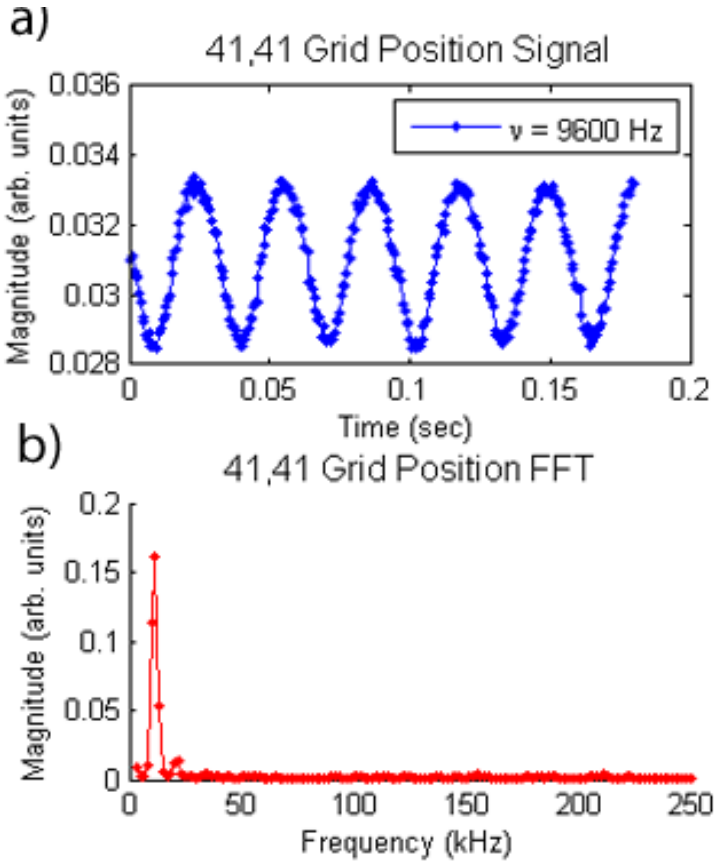

Figure 2.2. Timeseries measurement of the amplitude of the IQ mixer-based readout signal at the central point in the measurement scan (a) and FFT (b). We plot the real part of the FFT output $|S_{RO}|$.The signal in (a) is modulated at 9600 Hz, which shows up as a strong peak in a single frequency bin in (b).

the electric field amplitudes of the source probe and LO sources, f_{source} and f_{LO} are the source probe and LO frequencies, t is time and $\delta\phi$ is the relative phase shift between the two signals. The two signal input frequencies are related by $f_{source} = f_{LO} - \delta f$. Here it is important to distinguish the similarities and differences between the modulation we create in the MKID detectors versus a true heterodyne measurement. Similar to a coherent heterodyne beam map, we convert the detector readout signal S_{RO} to a complex field parameter. At each x, y point in the scan plane, the S_{RO} is recorded over a time T, where T is proportional to an integer number of waveforms triggered

by a reference signal. The peak in the Fourier transform (FFT) of S_{RO} is the complex field parameter $\alpha \pm i\beta$ at x, y. Figure 2.2 shows the timeseries recorded at the central grid location of our measurement plane, as well as the FFT of that series.

In a heterodyne mixer, the response time of the device is fast enough to respond to the time-varying E-field amplitudes, and the phase response of the detector matches the input signals. The response is fast enough to generate higher and lower ordered mixing products. For an MKID detector, S_{RO} is proportional to the number of quasi-particles generated in the resonant circuit by the incident field. The time constant of this response, defined by superconducting properties like quasi-particle lifetime, is not fast enough to respond directly to the incident field at THz frequencies. The phase of the incident field is lost when converting the intensity signal into the time-varying quasi-particle density, and the phase of the read-out modulation is no longer related to the two coherent sources. This is why the phase referencing system is required to properly reproduce the phase pattern of the device's response. The quasi-particle density is modulated (responds to) the difference frequency δf at the multiplication frequency IF, which can be chosen to fall within the bandwidth of the read-out electronics and is so recorded. No higher order mixer products are tracked by the MKID response, so there is no need for additional filtering or supression of these signals in the detector system. We use the IF notation for the multiplied difference frequency (modulation frequency) of S_{RO} due to its similarity to the conventional heterodyne receiver's output signal, though the mechanism for its generation and loss of phase coherence makes it considerably different in the case of a direct detector.

In the back-end electronics, $S_{RO} \Rightarrow \theta_{MKID}$, where θ_{MKID} is the phase of the complex in-phase and quadrature (IQ) signal used as the data acquisition technique for this experiment. This adds to an additional phase offset is introduced by the IQ

mixer, which is not referenced to the incoming optical signals. We therefore need to remove this effect with a phase reference system, described below.

The reference signal is created by splitting the signal from the LO and source probe synthesizers (at low frequency), combining them with a double-balanced harmonic mixer, and then feeding that signal as a trigger into the data acquisition module, also illustrated in figure 2.1. Data acquisition of S_{RO} is triggered by a positive zero crossing of the reference signal. The relative phase offset of the detected signal to the reference signal (here we chose to measure phase offset from zero for convenience) encodes the phase response of the KID detector.

In order to Nyquist sample the modulated MKID signal, the data acquisition (DAQ) system must have a sampling rate of at least $2 \times f_{IF}$. In principal, f_{IF} can be any positive value of Hz. Practical limitations for f_{IF} are the read-out rate of the DAQ, especially for arrays with multiplexed readout schemes. $1/f_{IF}$ must also be longer than the response time of the superconducting KID resonator. Lower values for f_{IF} may be used for devices with a slow response time, but there is a trade-off since higher offset frequencies decrease the $1/f$ noise in the system.

2.3 Experimental System

The DUT in this experiment was a meandering $\lambda/4$ hybrid Al-NbTiN superconducting MKID array, similar to the device in (Janssen et al. 2013) except using a sapphire substrate instead of silicon. We tested the geometrically-centered pixel of a 4×4 array. The detector was fed by a twin-slot antenna that sits beneath a 2 mm diameter laser-machined silicon lens array coupled to the device substrate.

The array was mounted in a dual stage 4He-3He cryostat reaching 250 mK. The

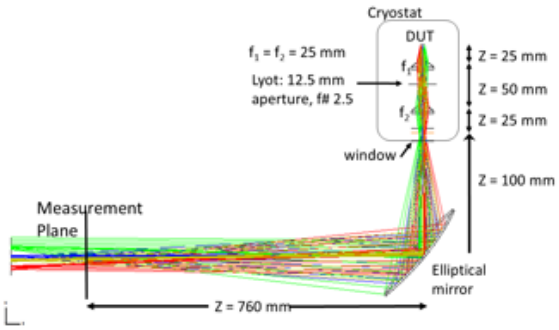

Figure 2.3. Optical system schematic of the 4He-3He cryostat. Not pictured is the beamsplitter with the injected LO signal. In this diagram you can see the measurement plane is inside the focal plane emerging from the ellipsoidal mirror.

cold optics consisted of a Gaussian beam telescope (see for example Goldsmith (1998)) made of two hyperbolic high density polyethylene (HDPE) lenses of focal length 25 mm and separated by twice the focal distance. One lens was directly mounted on the array housing and another was mounted to the 4 K shield. An cold stop (aperture) was placed in between the lenses, limiting the opening angle to an $f/2$ beam, or 14° half opening angle.

There was misalignment between the two lenses due to curvature in the 4 K plate, which also caused misalignment to the elliptical mirror of order 3 mm. For these reasons, the position of the elliptical mirror was adjusted to give the most symmetric 3 dB beam shapes for all pixels, trading the on-axis aberration performance for better off-axis performance. A system diagram is shown in figure 2.3.

We used a modified ALMA band 9×24 chain as the stationary LO source (Baryshev, Hesper, and Wild 2015). The scanned signal source was a harmonic generator based on a superlattice device set to maximize the output power of the 12^{th} harmonic of the input frequency (Paveliev et al. 2012). To reach our desired frequency we fed the harmonic generator with an active frequency doubler. The spectral output of this device was checked with a Michelson Fourier transform spectrometer to ensure

there were no undesired harmonics within the bandpass of the receiver. A low phase noise cable connected the scanned source to the synthesizer. The LO source used a split-plane diagonal feedhorn and the signal source used a recessed open-ended rectangular waveguide probe.

The read-out system used a IQ detection technique to measure changes in the transmitted phase of a microwave signal that passes through a common feedline coupled to each MKID in the array, based on the principle described in (Day et al. 2003). We used data acquisition rate of 500 kS/s which limited our Nyquist sampling frequency to 250 kHz. At each point in the scan plane, a 300 point timeseries was acquired, and 80 timeseries were averaged to produce the signal shown in figure 2.2a. The phase and amplitude are taken from the peak in the FFT, shown in figure 2.2b. Though somewhat arbitrary, the reference frequency of 400 Hz was chosen to ensure the modulation at high frequency (9.6 kHz) fell sufficiently below the Nyquist limit and the response time of the MKID at $\sim$30 kHz.

With this experimental system, simultaneous measurement of the beam patterns of multiple KID detectors in an array configuration is possible, with a multiplexing acquisition system and appropriate re-imaging optics as necessary. This proof-of-concept demonstration used only a single pixel for simplicity of the system configuration and computational processing. In principle, there is no significant difference in the measurement technique between scans of a single pixel versus an array.

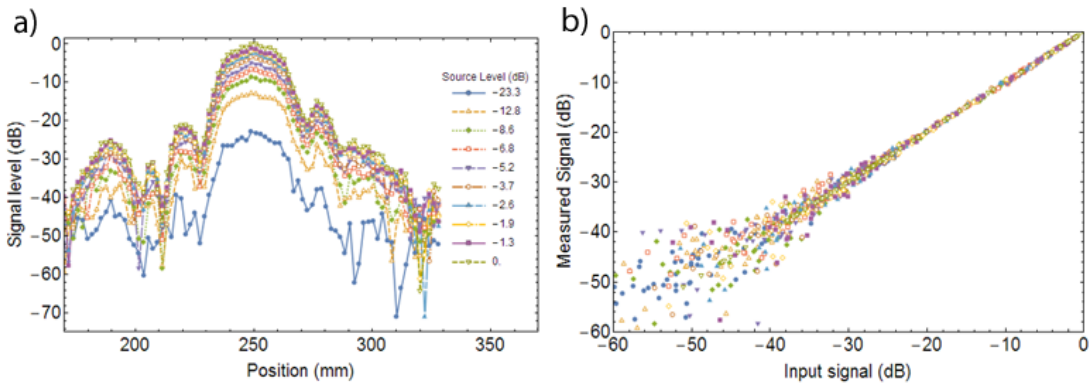

Figure 2.4. Amplitude response of the receiver taken multiple times over the same x cut while varying the source probe input power (a). Panel (b) compares the input power to output power for each scan. We see there is excellent agreement for input signals greater than ∼40 dB.

2.4 Results

2.4.1 Linearity

We measured the linearity of the DUT by making a series of cuts across the measurement plane while varying the input power to the signal source such that the amplitude response of the DUT was reduced. In each cut we measure the response over a relative signal source input power range of 50 dB. The detected power scans are shown in figure 2.4(a) and shows that the shape of the central lobe of the beam remains the same for over the full power range demonstrating excellent linearity of the KID. By comparing the measured cuts at low power levels one can accurately determine the source power of each cut. This subsequently allows the recovery of the linearity plot of the system shown in figure 2.4(b). For the beam scans presented in this manuscript, the source power was kept at 17.5 dBm for maximum stability and signal to noise ratio. corresponding to the -1.3 dBm line in figure 2.4(a).

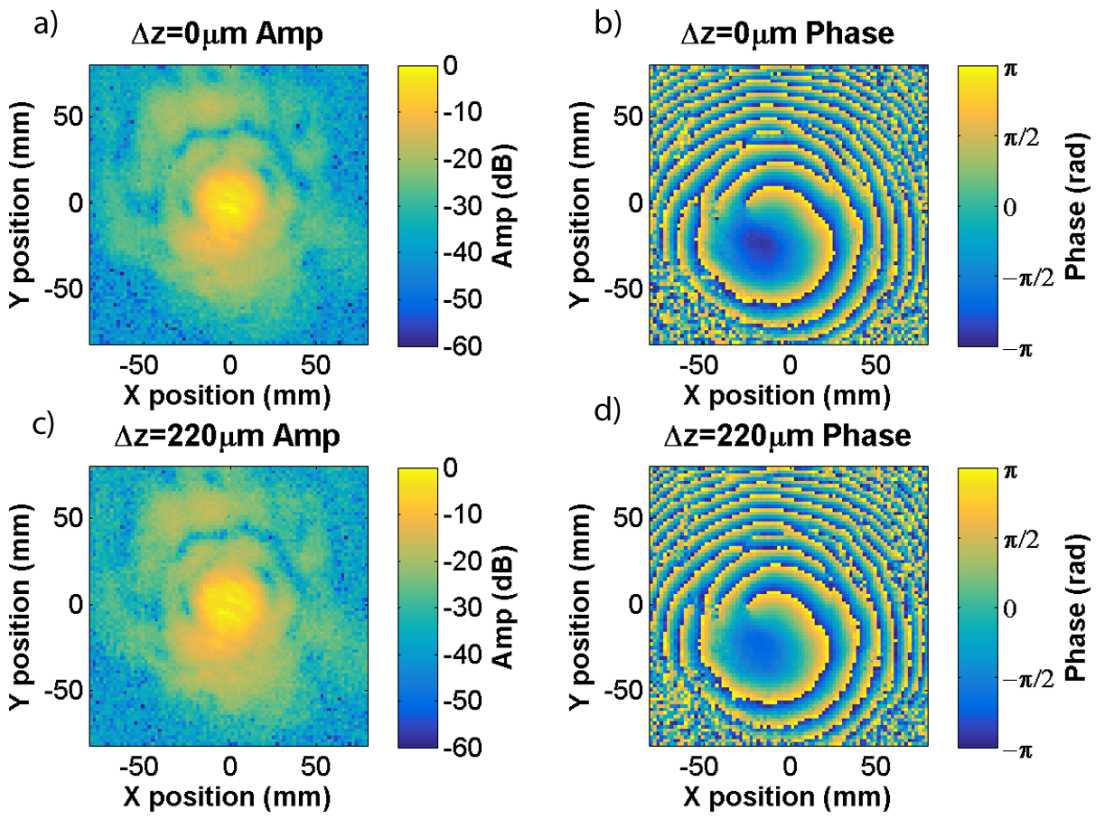

Figure 2.5. Amplitude (a, c) and phase (b, d) measurements of the beam pattern of the KID receiver. The top two panels (a, b) are the measurement with zero z offset, and the bottom two (c, d) were taken after the scanned source was shifted by a distance of z=220 μm.

2.4.2 Beam Scans

The amplitude and phase maps of the data collected using the above technique are presented in figure 2.5. The upper two scans were taken at a fixed distance from the cryostat, whereas the lower two scans were obtained by displacing the source by a distance of $\lambda/4$ from the original measurement plane. This axial offset was introduced to compensate for the effects of standing waves, as will be discussed in section 2.4.3. We have achieved a $\sim$40 dB dynamic range in the amplitude scans. The Gaussian

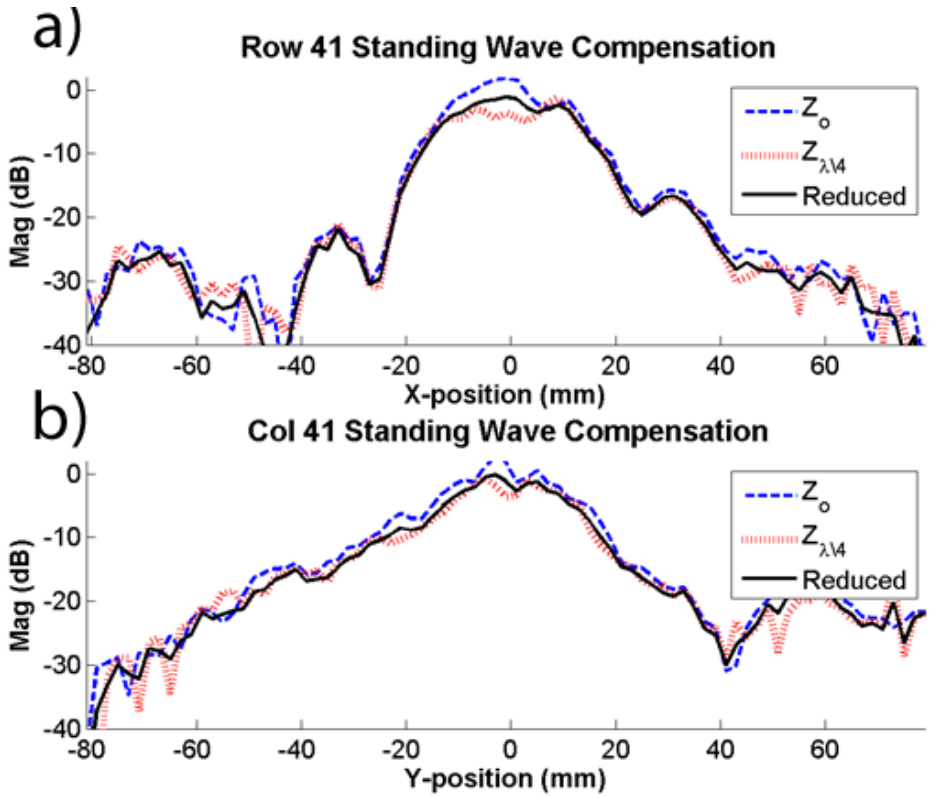

Figure 2.6. X-cut (a) and Y-cut (b) of the standing wave reduced amplitude map. The red and blue lines show the two cuts at $\delta z = 0\mu m$ and $\delta z = 220\mu m$, respectively, and the solid black line is the compensated signal.

beam can be clearly recognized in figure 2.5 (a) and (c), and (b) and (d) clearly reveal the spherical phase fronts of the diverging beams as the phase increases from the phase center outwards. The annular structure is caused by 'jumps' where the phase wraps from$-\pi$ to $+\pi$. Generally, the phase signal degrades where the noise floor is reached in the amplitude maps.

2.4.3 Standing Wave Compensation

Monochromatic measurements are particularly susceptible to standing waves, where reflections off of surfaces in the beam path can either constructively or destructively interfere with the incoming signal and cause a 'ripple' effect in the beam pattern. We find a strong standing wave effect discernible in the x and y cuts shown in figure 2.6, most notable at the peak of the central lobe. To correct for this, we employ the quarter wave offset technique, described in section 1.7.1 using equation (1.11).

Figure 2.6 shows the central E-plane and H-plane cuts through the measured data, illustrating that the compensated signal is much smoother than either the $\Delta z = 0\ \mu m$ or $\Delta z = 220\ \mu m$ maps. For this demonstration we manually moved the source probe for the z-offset with a micrometer mounted to the X/Y stage. Signal stability between the two maps could be increased by using a XYZ scanner that automatically takes the offset data before the system drifts significantly.

2.5 Gaussian Beam Analysis

To calculate the fundamental Gaussian beam parameters of the detector, we perform a normalized overlap integral in equation (1.13) to search for the best-fit fundamental Gaussian mode $\vec{E}_{ideal}$ given by equation (1.4) as discussed in section 1.5. This method works by using an initial guess of the three free beamfitting parameters in (1.4) ($\omega_{o,x}, \omega_{o,y}$ and the term characterizing the phase center offset in $\hat{x}$ and $\hat{y}$, $\delta z_{x,y}$) and producing an idealized Gaussian beam at the nearest focal plane of the optical system. As outlined in section 1.7.3, we correct for any offsets in the measurement system by producing the idealized beam in a new coordinate system with translational and

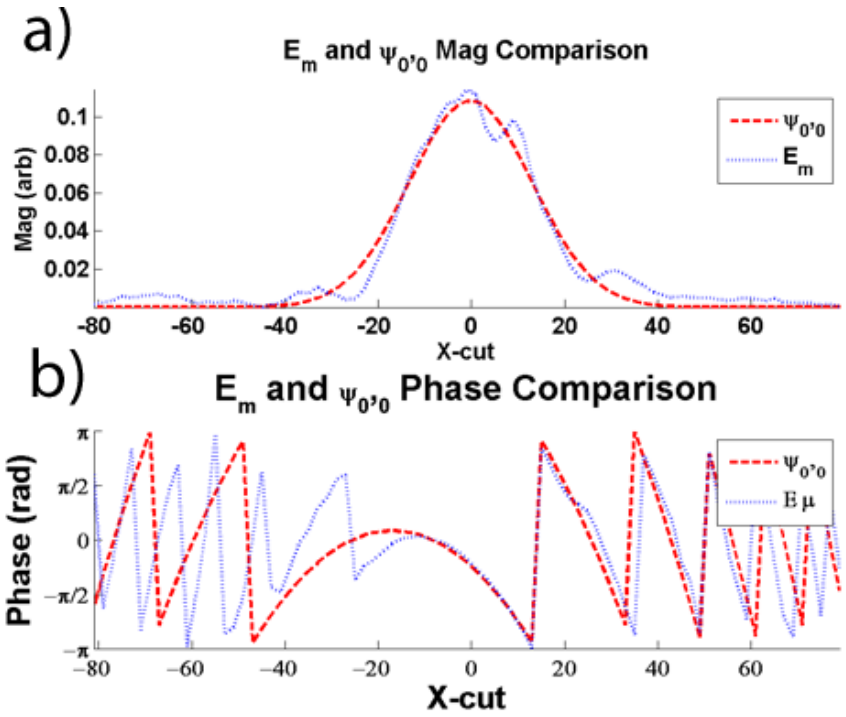

Figure 2.7. Comparison of the central H-plane cut of the measured field $\vec{E}_m$ to the fitted Gaussian $\vec{E}_{ideal}$ in amplitude (a) and phase (b). The phase fit between the measurement and idealized beams is very tight in the region of strong amplitude signal but falls off as the signal-to-noise level of the measurement increases. We see here that the phase center is not well aligned with the amplitude maximum of the beam. We believe this is caused both by a significant stray-light signal within the device substrate as well as a misalignment of the silicon lenslet array feeding the device.

rotational offsets to the measurement plane. The translational offsets are characterized by x-offset, y-offset, and z-offset, and the rotational offsets are characterized by the Euler rotation angles θ_{Eul1},θ_{Eul2},θ_{Eul3} .

Equation (1.13) determines the degree of coupling between the idealized beam and the measured complex field. We use the algorithm described in 1.7.3 to iterate over the Gaussian beam parameters to find those that produce the lowest coupling loss factor (1-$|c_{00}|$). The results of this analysis are summarized in table 2.2. We

Table 2.2. Gaussian Beam Parameters and Fit Values

Fitting Parameter	Initial Value	Measured
$\|c_{00}\|$ (unitless)	1.0	0.803
1-$\|c_{00}\|$ (unitless)	0.0	0.197
$\omega_{o,x}$	10.0	11.6
$\omega_{o,y}$	10.0	10.0
$\delta z_{x,y}$	0.0	-0.16
x	-24.0	-10.0
y	-26.0	-20.0
z	-760	-600
θ_{TB1} (°)	0.0	0.028
θ_{TB2} (°)	0.0	-0.017
θ_{TB3} (°)	0.0	0.16

Gaussian beam parameters and coordinate system transformation values minimized to produce an optimal model Gaussian beam from the measurement data. All values given in mm unless otherwise stated.

calculate the Gaussicity of the receiver's beam to be 80.3%, which matches decently to the 85% coupling predicted by antenna-lens simulations. It is likely that the 19.7% loss is scattered into higher order modes. There is also some loss due the presence of remaining standing waves that were not removed in section 2.4.3. These standing waves are most likely due to reflections within the cryostat from a defocused pupil and a tilt on the elliptical mirror.

We believe that there are significant optical performance degradation arising from the specific architecture of the DUT and misalignment of optical elements within the cryostat, which may include a standing wave on the device substrate and misalignment of the lens antenna. A complete and qualitative comparison of the measured and expected optical performance of this device requires full characterization and control of the optical system geometries to within fractions of a wavelength. It also requires rigorous electromagnetic modeling of the preliminary and experimental lens-antenna system, which will not be available until the physical nature of the device is better

understood and constrained. This level of characterization was not the primary purpose of this experimental demonstration. A methodical characterization of the optical performance of this new device is suggested for follow-up research but lies beyond the scope of this paper.

2.6 Angular Plane Wave Spectrum Analysis

We use equation (1.14) to transform the near-field map to the plane wave spectrum, and use the analysis outlined in sectio 1.7.4 to find the spectrum points and far-field beam pattern. Figure 2.8 shows the plane wave spectrum amplitude and phase plots for this dataset. We retain signal to noise ratio of $\sim$30 dB. The far-field map has recovered the Gaussian amplitude profile and the spherically symmetric phase structure. There is an introduction of rings, discernible in the amplitude map, which we attribute to diffraction from the propagation from the near-to-far fields rather than a side-lobe signal, since there is no evidence for such highly symmetric side lobes from the near-field map. The diffraction pattern could be suppressed by an apodizing spatial mask in the near-field before the transformation, following equation (**??**). However, this would also suppress the stray-light (off-axis) signal present in this measurement, which is useful in this case for characterizing the optical environment within the cryostat. The peak offset in the APWS amplitude is in excellent agreement with the fitted Gaussian beam tilt angles, listed in table 2.2, both in sign as well as magnitude, illustrating that the key optical system properties can be consistently extracted from a single complex beam map.

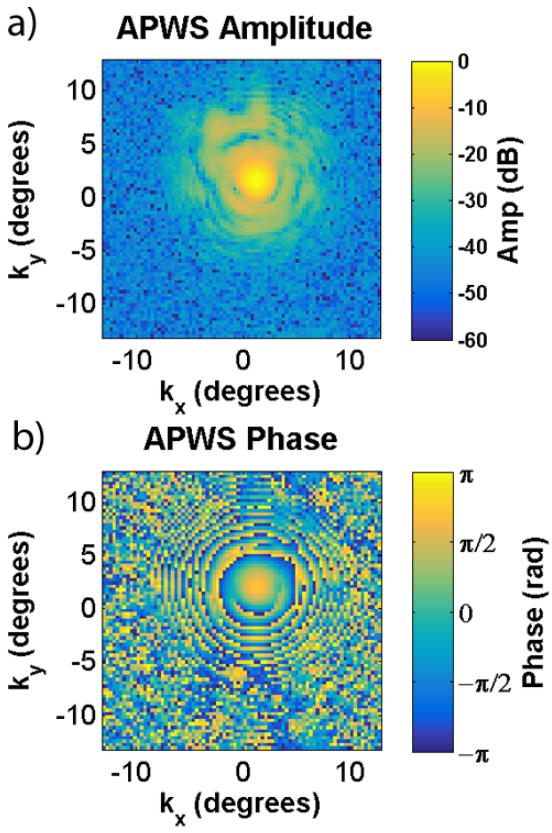

Figure 2.8. The paraxial far field of the measured data. Amplitude is shown in (a) and phase is shown in (b). The phase is clearly recovered by the transformation, and we see that the signal degradation in the phase measurement traces the low signal in the amplitude measurement. There is significant diffraction effects present in both maps, but we believe some of this can be removed by spatially filtering the near-field data.

2.7 Conclusions

In this chapter we have unambiguously demonstrated a complex measurement technique using a MKID detector, which is in principle suitable for other direct detector instrument types. This new technique provides measurement accuracy suitable to determine the primary beam characteristics of interest for receiver characterization. The phase preservation through APWS analysis, agreement to the predicted Gaussicity,

and the agreement between the beam angles and derived from the overlap integral analysis and the APWS analysis verifies the system reliability. Future analysis of this dataset will be useful in diagnosing the optical misalignments of this optical system, and the monochromatic measurements can be directly compared to discreet frequency optical simulations.

Though complex beam measurements have an increase in cost and complexity in electrical components compared to scalar measurements, the advantage in the capability of performing multiple diagnostic tests from a single scan, making the required scan area significantly smaller, make this measurement technique valuable for most instruments. Importantly, a single scan at a fixed position in z simultaneously finds the beam waist and focal position of the receiver. We will continue this work by understanding the optical performance of each element in the receiver chain and completing the analysis of the end-to-end system, with detailed comparisons of the measurement to electromagnetic simulations. Follow-up work for other instrument analyses are already underway to take this system and use it as a diagnostic tool both from a device and an instrument perspective, as well as scaling the analysis pipeline to measure a full detector array.

Chapter 3

COMPLEX FIELD MAPPING OF LARGE DIRECT DETECTOR FOCAL PLANE ARRAYS

Abstract

As a follow up to the previous chapter in which we demonstrate a complex field measurement of a single pixel MKID receiver, we scaled the system hardware and processing pipeline to analyze the response of an entire focal plane array instrument. The system architecture described in sections 3.2.1 , 3.2.2, and 3.3.3 is tailored for direct detector instruments, but section 3.4.2 are useful to any complex field array measurements, either direct-detector or mixer based.

A significant part of the development of the analysis pipeline presented here relies on streamlining the code as much as possible to reduce the computation time of the analysis steps running over several gigabytes worth of data. Many of the analysis pipeline steps had to be re-written to vectorize the analysis routines, eliminating some processes that had originally run using 'for loops'. The original pipeline was written in Matlab (Inc. 2016) software, and used a method of assigning 'global variables' to pass data in between functions such that the minimization algorithm did not change the data, only the analysis variables. However, this approach does not allow for parallel processing techniques because there can only be one global variable assignment to the code directory. Instead, the code for this pipeline was rewritten to use a nested-function approach, which does allow for parallel processing.

Another consideration of the analysis pipeline is to make the analysis steps flow seamlessly between each segment, but also be able to run independently.

Each segment is designed such that it can handle datasets with arbitrary scan plane dimensions, pixel counts, and sampling frequencies. The only steps individualized to the specific nature of the input dataset is the first step in the pipeline, and the pixel matching routine to combine the two polarization datasets. With little software finessing the pipeline should handle data from many instruments and read-out electronics systems.

3.1 Introduction

Astronomical survey instruments naturally progress towards large focal plane cameras with wide-field optics schemes. Visible light cameras have achieved pixel counts in the hundreds of megapixels or more. At lower frequencies, both microwave kinetic inductance detector (MKID) array (Day et al. 2003), (Baselmans 2012), (Doyle et al. 2008) and transition-edge sensor (TES) (Irwin and Hilton 2005), (Romani et al. 1999), (Beyer 2010) array cameras are being developed and approaching kilo-pixel detector counts. In the sub-millimeter regime, each detector can no longer be considered as a 'light-bucket' that captures incident photons with a calibrated base efficiency, and thus the coupling mechanism to each individual pixel must be taken into consideration when calibrating the data for image processing.

Characterizing large array instruments in this regime presents a unique challenge to conventional calibration techniques. Some of the next big scientific questions can be addressed with widefield instruments but require breakthroughs in sensitivity and polarization accuracy of these arrays. For example, the next generation of CMB mapping missions envisioned for both ground and space-based CMB-S4 need unprecedented pointing knowledge, sensitivity, and polarization selectivity to detect or set limits on the energy in primordial B-modes of CMB photon polarization

(Abazajian et al. 2016). For imaging instruments studying extended sources, such as the polarization of thermal emission from dusty molecular clouds as the grains align to the galactic field lines (Galitzki et al. 2014), (Dober et al. 2016), accurate pointing knowledge of the beams is necessary to fully reconstruct the astronomical image. However, as the field of view increases, it becomes increasingly difficult to ensure uniform alignment accuracy, stability, and coupling to calibration sources when characterizing the instrument prior to deployment. New characterization techniques are called for to address these scientific questions (see Abitbol et al. 2017, section 4.6).

Broadband (direct) detectors are phase insensitive, so the full on-sky beam patterns have traditionally been measured with thermal (incoherent) sources (Murphy et al. 2010), typically in the far field of the instrument. However, complex field mapping offers several advantages not available to thermal beam scans. The phase pattern of a detector element probes the optical path length difference measured in a plane normal to the principle axis of the instrument. To determine the fundamental Gaussian beam parameters, the complex field can be fit to a model function, and can in principle be used to obtain offsets in the phase center along the E- and H-planes. The scan plane can be located at any place along the optical axis, for instance in the near-field of a telescope's focal plane. Complex field measurements can also accurately predict an instrument's coupling to a telescope.

Most commercially available optical modeling software can solve only for monochromatic beam patterns. Complex field measurements are naturally monochromatic and therefore allow the measured response to be compared directly to simulation data, which is not influenced by instrument/measurement effects . The most common type of instrument effect is the presence of standing waves. This scanning strategy and analysis pipeline we preset removes the first-order standing waves introduced between

the source probe and the optical system (i.e. standing waves between the source probe and cryostat) by moving the source probe by a quarter wave offset in z between two measurement scans. A standing wave will have a 180° phase shift between scan planes, and will cancel itself when averaged during post-processing.

Because optical standing waves and alignment errors between the scan system and the instrument can be corrected and removed during post processing, we reduce the number of measurement scans required to calculate the bore-sight angle for the array. Doing so eliminates the need for extensive metrology to ensure alignment of the probe system. Additionally, the complex field parameters measured in an arbitrary plane can be propagated either forwards or backwards through optical elements to arbitrary planes along the principal axis (see discussion in (Jellema 2015)).

Coherent beam pattern measurements are standard for missions using heterodyne receivers, and have been used to characterize Flagship-class missions such as IRAM, Herschel, and ALMA (Tong, Paine, and Blundell 1994), (Tong et al. 2003), (Carter et al. 2002), (Jellema 2015), (Naruse et al. 2009), (Baryshev, A. M. et al. 2015).

A two-source coherent detection approach to beam characterization of direct-detector instruments in the sub-millimeter regime was first presented in C. N. Thomas and Withington (2013) where the phase difference between the two sources was modulated to create interference fringes detected by a commercial power meter. An alternate approach was presented in Davis et al. (2017) using a quasi-heterodyne technique where the two coherent sources are coupled in front of the FPA with a passive beamsplitter. The two sources are slightly offset in frequency, and the optical difference or 'beat' frequency modulates the detector response. By tuning the beat frequency to fall within the response time of the read-out system, the modulation can be tracked in the time domain and the complex field parameters can be acquired

through a FFT of the response signal. The beam map is the resulting amplitude and phase of the FFT peak as a function of pixel position. Because direct detectors are not true mixing devices, the phase of the incoming signal is not preserved through the readout system. Therefore, to properly reconstruct the phase pattern of the measurement, the detector response must be referenced to the drive signal. We produce this reference tone by splitting the drive signal at low frequency and passing one branch from each source to a low frequency harmonic mixer. The phase of the reference signal is used to calibrate the detector response signal in post-processing. Though originally demonstrated using MKID detectors, the principle applies to TES arrays as well as other direct detectors, provided that they have sufficiently fast response time.

The work presented in Davis et al. (2017) demonstrated detailed analysis on only a single pixel of a 3×3 array. For wide-field optical systems, maintaining the required level of calibration stability over a long scan duration drives the need for modifications to the experimental apparatus, system configuration, and analysis pipeline. Firstly, a new optical injection scheme is necessary to uniformly illuminate the array with the local oscillator (LO) source. The phase referencing system was modified to be read continuously on a calibration tone in the read out system rather than triggering data acquisition. We also use an on-the-fly (OTF) scanning strategy in order to minimize the scan duration as compared to a step-and-integrate scan strategy. Additionally, updates to the post-processing pipeline required implementing parallel processing tools to streamline the analysis.

We demonstrate an additional processing step detailed in 1 in the analysis pipeline to extract the co- and cross-polarization radiation patterns from the measurement data. This is a new technique we did not employ in chapter 2. By measuring the

complex field patterns we are able to take two scans in orthogonal directions that are at an arbitrary rotation angle with respect to the image plane. The co- and cross-polarization fields were extracted individually for each pixel by re-projecting the two orthogonal measurement planes onto a rotated coordinate system until the signal is the co-polarization field is maximized (and the signal in the cross-polarization field is minimized). The aim is for this characterization scheme to help address the characterization improvements called for in Abitbol et al. (2017).

3.2 Methods

The analysis methods originally proposed in (Davis et al. 2017) is both computationally expensive and was plagued by system drifts over the scan duration set by the point-by-point integration scanning strategy. To scale the technique to kilo-pixel array characterization, we adapted both the hardware implementation and software processing techniques for phase referencing to more rapidly acquire the timestream signal from each individual pixel. By transitioning to an on-the-fly (OTF) scanning strategy we reduced the scan duration from 20 hours to 4 hours per scan, leading to significantly improved phase stability over the course of a measurement. We also include the details of the co- and cross-polarization finding algorithm in this section.

3.2.1 Phase Acquisition

Phase patterns of direct detectors can be measured by modulating the detector readout in the time domain, using the interference of two coherent RF sources at gridded intervals across a scan plane, as shown in figure 3.1. In this experiment, the RF

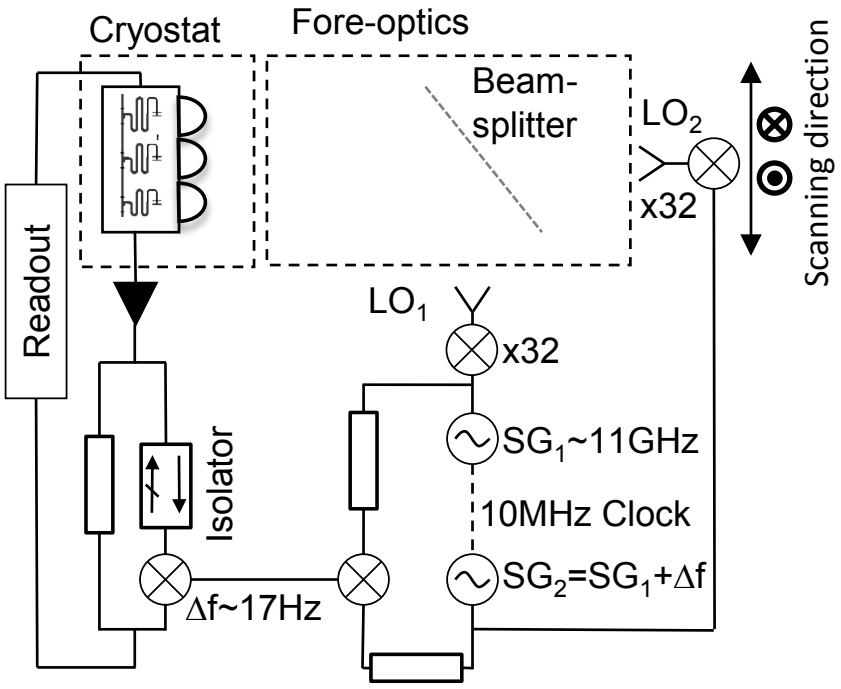

Figure 3.1. Electrical and optical coupling scheme. The two local oscillators (LO) are driven at $\times 32$ of the frequency from two signal generators (SG), one at 11.25 GHz while the second is offset by Δf =17.66Hz. The power and polarization of LO_1 is controlled via two polarizers, while a 150mm focal length lens is used to optimize the coupling over the field of view. The difference signal is mixed together, and used to modulate the MKID readout. This is then extracted in software, giving the phase reference and allowing phase noise correction. The attenuators and directional coupler optimize the linearity of the reference signal and reduces leakage of one LO signal into the other.

signals are generated using a multiplier chain (Local Oscillator LO_1) and a harmonic mixer (LO_2). Each LO chain outputs a signal at the M^{th} (here 32^{nd}) harmonic of the drive signal, here 11.26 GHz, such that the RF frequency is $\sim$ 360 GHz. The two synthesizers are driven with a small offset frequency ($\Delta f \sim 17.66$ Hz), which produces a intermediate frequency ($IF_{optical} = 565$ Hz) through coherent modulation of the quasiparticle number in the MKID pixel.

Multiplexing for the array under test is based on a frequency domain read-out

scheme, where each MKID is coupled at a individual frequency in the range 4...8 GHz to a transmission line. A signal generator produces a frequency comb with all the tones for each device, plus an additional set of extra tones (blind tones) that are uncoupled. These blind tones are used to remove electrical system drifts and aid calibration. To extend the complex beam pattern measurements from a signal pixel to a multiplexed readout, we use the phase reference to directly modulate the multiplexed MKID readout (Rantwijk et al. 2016).

The phase reference signal is generated as in (Davis et al. 2017) by splitting a signal from the two drive synthesizers at low frequency and mixing the signals with a double balanced mixer, generating a $\mathrm{IF_{ref}} = \Delta f$. The mixer is driven in the linear regime to accurately translate the reference and noise from the synthesizers whilst minimizing higher order harmonic generation. A second double-balanced mixer is used to upconvert $\mathrm{IF_{ref}} \rightarrow \mathrm{IF_{opt}}$ and encode it onto the blind tones. The power in the second mixer is optimized to keep it in the linear regime, while an isolator is added in series to reduce reflections off the mixer. The phase reference can then be extracted from the blind tones in pre-processing (described in section 3.2.2) before the blind tone correction is applied. It is important to note that the phase reference gives no stray contribution to the measured optical signal; the blind tone correction suppress the phase reference signal on the KID tones, while the phase reference is at $\times 32$ lower frequency than the optical signal.

3.2.2 Pre-processing Pipeline

The multiplexed readout (Rantwijk et al. 2016) samples the MKID signals at a rate of 1.271 KHz, and can read out $\sim$500 MKIDs and 100 extra blind tones. The choice of

using a offset frequency of $\Delta f \sim 17.66$ Hz synchronizes the reference frequency with the data acquisition rate, such that the period of one reference waveform is an integral number of samples. We calibrate the signal so that it is proportional to absorbed power with the following steps: 1) performing a blind tone correction to remove cable phase delay and system readout drifts (Rantwijk et al. 2016); 2) maximizing the signal-to-noise ratio and giving a first order linearizion by calibrating the complex phase plane relative to the MKID resonance circle (Gao et al. 2007); and 3) finally calibrating a signal of relative frequency shift to the MKID resonance (Bisigello et al. 2016), which is proportional to the incoming power (Calvo, M. et al. 2013).We use the average of the uncalibrated blind tones for the phase reference signal.

For each pixel, the data recorded in the time domain is separated into blocks corresponding to a single position of the source probe in the scan plane. The length of each block is set to the period of one full reference waveform (0.56 ms). A complex fast-Fourier transform (FFT) of each block is performed, where the output resembles a delta function at the frequency bin corresponding to the optical modulation $\mathrm{IF_{opt}}$ (565 Hz). A FFT of the phase reference at the same source probe location is performed, with the signal appearing in the bin corresponding to $\mathrm{IF_{opt}}$ (17.66 Hz). The phase of the reference signal is then multiplied by $M = 32$ and subtracted from the detector FFT phase. This produces the fully corrected complex field point at each location in the scan plane. Long term drifts in amplitude and phase of the system are measured by periodically returning to a reference position during the scan, which are interpolated and then subtracted from the interleaving points in the scan plane.

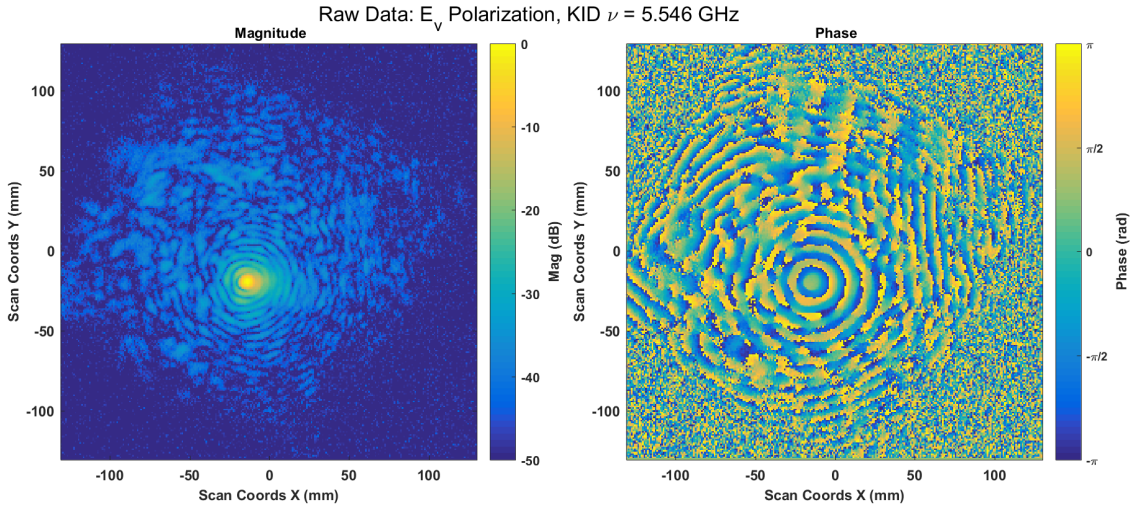

Figure 3.2. Full pre-processed complex field map for a representative pixel located at the center of the array. The data shown is shown for the E_h polarization, and has not yet been processed to find the co- and cross-polarization axis. The array under test has a stray-light absorbing mesh fabricated in the device substrate to minimize reflections between pixels; however, there is still significant coupling to the pixel even at the array edge. The rotation of the scan plane with respect to the instrument principle $\hat{x}$ and $\hat{y}$ axis is clearly visible. The extent of the scan plane past the edges of the array is both to reach a -30 dB minimum in the radiation pattern of the edge pixels but also to allow spatial filtering for the beamfitting and far-field transformation pipeline processes, described later in sections 3.4.2.1 and 3.4.2.2.

3.2.3 Phase and Amplitude Noise

At each point in the scan plane, the optical modulation of the moving source probe $\vec{E}_{LO_2}$ and stationary LO $\vec{E}_{LO_1}$ will modulate the power response of the detector according to equation (3.1):

$$P_{det}(x,y) \approx \frac{|\vec{E}_{LO_1}|^2}{2} + \frac{|\vec{E}_{LO_2}|^2}{2} + |\vec{E}_{LO_1}||\vec{E}_{LO_2}|\cos(2\pi M\Delta f + \Delta\phi) \qquad (3.1)$$

where $\vec{E}_{LO_i}$ is the E-field generated by each of the two sources. Here we assume that the $\vec{E}_{LO_2}$ field represents the convolution between the source probe and the optical system's radiation pattern at each point in the scan plane. The first two terms of equation (**??**) correspond to DC offsets, from direct the coupling of the sources

to the detector. The last term describes the optical modulation due to the coherent interference of the two sources.

The noise is this measurement, to first order, is dominated by noise on the optical sources and will scale linearly with the signal strength. Therefore, the best signal-to-noise ratio is reached where $\vec{E}_{LO_1} \approx \vec{E}_{LO_2}$, else the noise will become dominated by the DC terms. Increasing $\vec{E}_{LO_1}$ to increase the modulation depth will degrade the noise performance. Additional noise from the setup stability (eg. beamsplitter vibration) will be, to first order, added to the $\vec{E}_{LO_2}$ term, which is the static source coupled via the beamsplitter.

From equation (3.1) we see that the power response of the detector is proportional to the amplitude of the E-field produced by the source probe. To obtain the power beam pattern, the E-field magnitude and thus the instrument power response must be squared. This has the effect of squaring the power dynamic range of the complex-field measurement compared to a direct measurement using a single optical source with the same source power. Here we achieve unprecedented signal to noise for a direct detector instrument, with a (detector) noise floor of <-55 dB compared to beam maximum.

The source noise is dominated by the phase and amplitude noise from the synthesizers, which has a $1/f^2$ frequency dependence. Direct detectors tend to be slow, as high on-chip integration improves the sensitivity. Therefore, only low $\mathrm{IF}_{\mathrm{optical}}$ frequencies will fall within the read-out bandwidth of the detector, leading to the measurement noise being dominated by synthesizer stability. The noise can be estimated from the specifications of the synthesizers used in our experiment. At 10 GHz, only 1 Hz from the drive frequency, the synthesizer noise specified from the manufacturer was -44 $^{dBc}/_{Hz}$. This leads to an expected experimental noise, assuming the sources are equal in power, of 2×32^2 higher, or $-10 \sim {}^{dBc}/_{Hz}$, or 0.1 $^{rad}/_{\sqrt{Hz}}$. The full software

phase correction using the phase reference further reduces this to 40 $^{mrad}/\sqrt{Hz}$, showing the phase reference also corrects a significant amount of phase noise. This corresponds to RMS setup stability of order of 11 $^{\mu m}/\sqrt{Hz}$, for the optical wavelength of 833 μm. After phase correction, measured standard deviation of phase noise varies with $\sqrt{\text{time}}$, which is a Gaussian noise term (rather than $^1/_f$). Amplitude noise does not scale this way, so it is $^1/_f$ limited. Excess phase noise prevents complex data analysis, and will smear out the amplitude signal. Typically, a reasonable requirement on the measurement phase noise is $\lesssim {}^{\lambda}/_{25}$ which is equivalent to ~ 20 % loss (Ruze 1966). We reach that limit here in 0.22 s of acquisition, which sets the limits on the scanning speed.

3.2.4 On-The-Fly Scanning Strategy

The scanning strategy and integration time must be optimized to ensure accurate beam reconstruction and amplitude and phase stability. Nyquist sampling of the beam patterns corresponds to points in the scan plane spaced by the half of the full-width half maximum (FWHM) beamsize at the focus. However, higher angle information—for example ghosts, reflections, and beam steering—can be extracted by oversampling and looking at the far field beam patterns, see section 3.4.2.2. Quick diagnostic scans can be done at Nyquist spacing, but the full data presented here is oversampled by a factor of 2 at $^{FWHM}/_4$ grid spacing, which corresponds to a 1 mm spacing over a 260×260 mm scan plane.

The simplest scan mode is step-and-integrate, where the source probe is stationary for a set period of time at each x, y point in the scan plane before the scanner moves to the next x, y point. However, this strategy suffers from 'dead time' as the scanner

moves. For widefield instruments that require lots of x, y points, this dead time can dominate the scan duration. We therefore adopted a partial OTF scanning strategy which proceeds as follows: At a given x position the scanner is scanned slowly in y; the scanner then moves to the next z position and repeats the y-scan (in order to remove optical standing waves in post-processing); then the scanner rapidly returns to a drift reference position (to enable long term drift removal); and finally the scanner moves to the next x position and repeats the process.

A slow scan speed of 8 mm/s was used, giving 0.125 s integration per mm, equivalent to 2 reference waveforms (blocks). Each scan in y takes $\sim$35 s. Synchronization between the scanner and data acquisition is done in software via an Ethernet connection, but faster scan rates can be done with a hardware trigger (see Baryshev, A. M. et al. 2015). A crosscheck of the software trigger was performed by checking OTF and step and integrate beam pattern cross-cuts of the array. A scan at a z offset of $\lambda/4$ enables first-order standing wave removal (Davis et al. 2017), and further improves phase and amplitude noise. The measurements we present are taken near the focal plane, where the phase front is flat except for phase jumps at the sidelobes. Further from the image plane, the wavefront will be more spherical, and care must be taken that the phase does not change rapidly over each measurement block, or it will not be correctly sampled.

3.3 Experimental System

3.3.1 Test Array

To demonstrate the effectiveness of our measurement and analysis technique, we measured the complex field patterns of a representative wide field, high pixel count, direct detector array. Our choice was the APEX Microwave Kinetic Inductance Detector (A-MKID), developed for the APEX telescope on the Atacama Plateau in Chile (Otal 2014). Its primary mission is to survey the nearby galaxy to study the formation and disruption of interstellar medium (ISM) clouds. AMKID serves as a complimentary instrument to identify interesting sources for follow-up target studies using high resolution observations, such as with ALMA. AMKID is separated into two frequency bands, with he higher band centered at $\nu = 850$ GHz. The low frequency band centered at $\nu = 350$ GHz is an 880-pixel, single polarization MKID array with a $15'$ by $15'$ field of view. Each frequency band consists of 4 MKID sub-arrays, and one spare sub-array for L-band is characterized in this analysis.

Each individual pixel is a meandering MKID with a twin-slot coupling antenna. The pixels are hexagonally packed with a pitch of 2 mm on a chip measuring 60.8×62 mm. The antenna is fed by a silicon lens mounted to the front of the array. A stray light absorber is integrated into the chip, giving good imaging capabilities. More details on the chip fabrication and results are presented in S. J. Yates et al. (2017). The dynamic range from the technique presented here was essential in identifying the mitigation of the on-chip stray light problem.

The array uses a readout scheme with an intermediate frequency (IF) bandwidth of 4.2-7.8 GHz broken up into two sections, each with 2 GHz bandwidth. The readout

(Rantwijk et al. 2016) currently only has 2 GHz of bandwidth, which with only one readout available on site requires two separate measurements to readout the entire array. The channels are interleaved in a spiral pattern to help eliminate cross-talk to adjacent pixels on the array (Baselmans, J. J. A. et al. 2017).

3.3.2 Optics

To test the technique, the test array was mounted at 250 mK in an optical cryostat designed to test sub-arrays for the A-MKID instrument. The system optics is a wide field camera, made from an aberration compensated (Murphy 1987) optical relay of magnification M=3 using four active mirrors and three fold mirrors. The active mirror surface shape is optimized from an initial parabolic shape to biconic, to give low aberration, distortion performance with a designed Strehl ratio greater than 0.99 over the entire field of view (FOV). It consists of two separate mirror relays, one internally mounted at 4 K and one mounted externally. The fold mirrors rotate the array by $\sim$ 30 deg but give access to a horizontal image focal plane for testing. The array image size is 180$\times$180 mm, which is slightly smaller than the FOV. Scan are done in an xy plane which is 30 deg rotated with respect to the array, so we need to scan 260mm by 260mm to get the entire FOV.

The optical band is selected by a filter stack. Note, there is required > 60 dB of optical attenuation of the out-of-band radiation power, dominated by infra-red. This is achieved with multiple infra-red filters, but it is necessary also to block stray light leaks and self emission from filter heating. A cold aperture (pupil) limits the opening angle on the array to 14 deg, or a focal length to diameter (f#) ratio of 2 at the array. More details on the cryostat and filtering are presented in S. J. Yates et al. (2017).

3.3.3 LO Injection

To measure all pixels simultaneously, the static optical source LO_1 needs to be coupled to the entire array. However, with the folded optics there is not enough space to couple LO_1 at the image focal plane. These problems are here solved by weakly coupling LO_1 with a thin film beamsplitter at a position near the image of the pupil in the warm optics. Here, all beams overlap spatially, but have different steering or boresight angle. The beamsplitter reflects < 10 % of the beam, and we ensure that the reflected beam and transmitted non-reflected power from LO_1 are terminated on a 300 K load. A lens is used between the LO and beamsplitter to match the beams, while a defocus allows optimization of coupling across the entire array. Additionally, two polarizers are added to fix the LO polarization and allow tunability of the source power: the LO_1 source power is ~ 10 μW, while the power per pixel is $\sim$10 pW, so even weakly coupled to 1000 pixels the LO power needs further control. Variation in the coupling of LO_1 across the array varies the individual pixel's beam pattern signal strength, however in the presented data the entire FOV has sufficient signal to noise to enable full beam fitting and data analysis.

3.4 Analysis

The analysis pipeline we create for the complex field maps described here can be broken into three main stages : 1) pre-processing of the raw data output readout system and FFT processing to the complex field points across the scan plane, as described above in section 3.2.2; 2) preliminary map processing via performing a linearity analysis between the two polarized scan planes, the elimination of standing

waves, and making co- and cross-polarization maps, described in section 3.4.1; and 3) optical analysis of the processed maps including Gaussian beam fitting and near-to-far field transformation described in section 3.4.2.

3.4.1 Map Processing

3.4.1.1 Linearity

The radiation pattern of the FPA was measured twice resulting in the measurements $\vec{E}_h$ and $\vec{E}_v$, where the subscripts h and v refer to the polarization of the source probe aligned horizontally and vertically with respect to the scan plane, respectively. In the data presented here, the source was aligned close to the co-polarization for one scan and close to the cross-polarization for the second scan. We keep the convention of the subscripts h and v to avoid confusion with the fields $\vec{E}_c$ and $\vec{E}_x$, which refer to the processed co- and cross-polar field maps.

Because of the close alignment to the co- and cross-polarization axis, the power absorbed by each detector for the $\vec{E}_h$ polarization orientation was significantly stronger than when the source was more aligned towards the cross-polarization axis $\vec{E}_v$.We therefore performed a linearity check on the response of the detector as the drive power for the source probe was increased within this range. We scanned a representative central pixel for several linear cuts across the scan plane while decreasing the source probe power between each cut. Figure 3.3 shows that as the power decreases, we see excellent linearity across the peak and main side lobes of the beam. We conclude that the source power offset between the two scans of $\vec{E}_h$ and $\vec{E}_v$ will result in a linear scaling factor between the two maps. From scans across a representative pixel in the

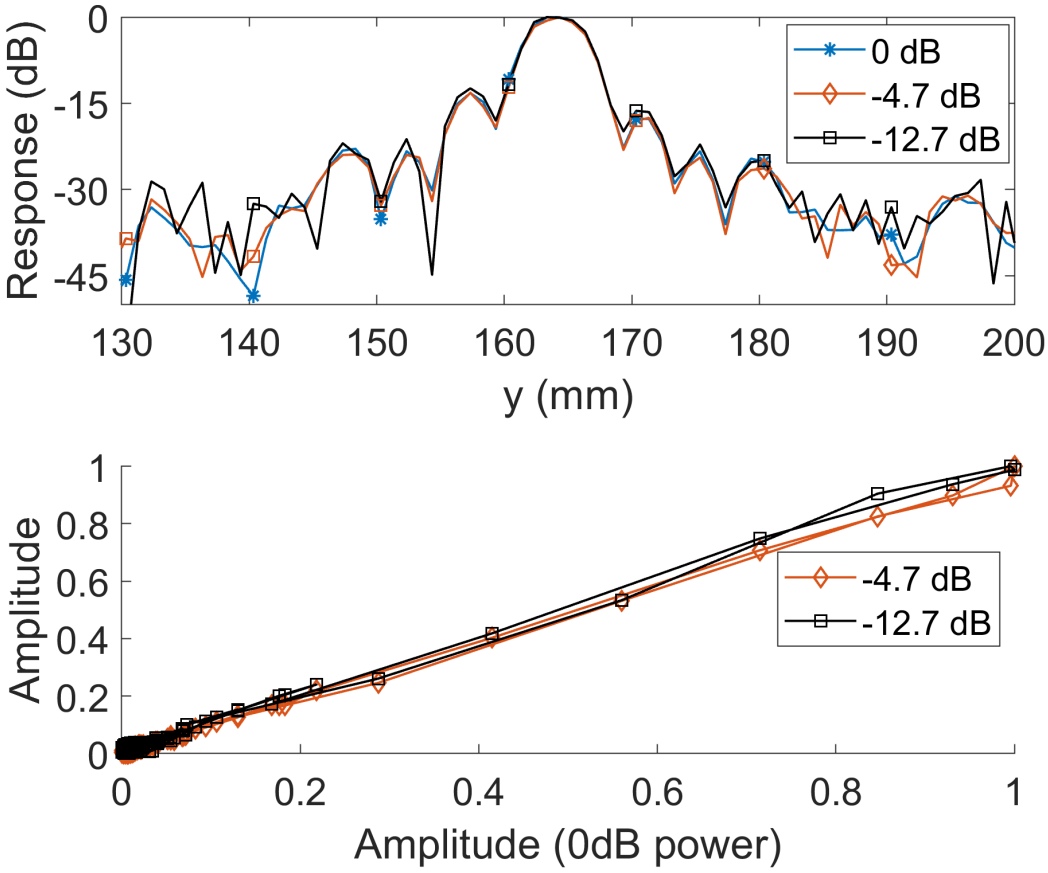

Figure 3.3. Three separate measurements of scanning across one pixel. For each measurement, the power of source Lo_1 was reduced relative to the first by the amount given in the legend. The top panel shows the measurements in dB relative to their maximum response; the lower panel the amplitude response of versus the first high power measurement. The difference between measurements shows the measurements to be linear within standard deviation of order $\lesssim 10\%$, limited by the optical source noise.

middle of the focal plane, we find that we need to increase the drive power of the source probe by $\sim$ 17.8 dB to measure the same absolute power at the detector.

Using these results for field mapping, we increased the drive power to the source probe by 17.8 dB for the $\vec{E}_v$ source probe orientation so that there was enough detected power to produce the same signal-to-noise ratio in each map. However, to properly determine the co- and cross-polarization axis, the absolute power in each map needs to be properly represented since the algorithm minimizes $|\vec{E}_x|$. Therefore, we scale $|\vec{E}_h|$ by +17.8 dB before fitting the values of A and ϕ according to equation (1.12). A then becomes a scaling parameter to encompass the coupling difference between the source and detector at each orientation, and also is adjusts for the relative power levels received by each individual pixel across the array, since the value 17.8 dB was found by scanning only one pixel.

3.4.1.2 KID Matching

As part of the start-up routine and calibration process for the FPA, the KID frequencies are re-calibrated between each measurement scan. This calibration is automatic as part of the start-up routine for the array because the resonant frequency of each device can shift due to different thermal or optical loading within the cryostat. Additionally, for each polarization measurement the optical source power was tuned to optimize signal to noise. The consequence of that step for this analysis was that the KID pixel read-out frequencies differ between the $\vec{E}_h$ and $\vec{E}_v$ scans, which caused problems because the only way a pixel is identified in the raw output is by read-out frequency.

Therefore, a processing step is introduced to match individual pixels between the

$\vec{E}_h$ and $\vec{E}_v$ datasets. We use a two-step matching technique that finds the closest match in frequency between the two scans but does a follow-up check on the location of the amplitude maximum. For the two scans, we first set a frequency tolerance level for disparity between the two measurements, $\nu_{tol} = \pm 10$ kHz. An algorithm takes each KID pixel frequency from one scan and searches for a match within $\pm\nu_{tol}$. If a match is found, the algorithm then calculates the central peak position of both maps, and determines if they fit within a distance tolerance $\pm d_{tol}$, where $d_{tol} = \pm 8$ mm. If more than one match is found within ν_{tol}, the best match between d_{tol} is selected as a match, otherwise the algorithm exits with no match. With an initial pixel count of 732 pixels, the routine matches 718 pixels corresponding to a matching yield of 98.1 %.

3.4.1.3 Polarization

The analysis pipeline uses a minimization algorithm to determine the rotation angle to project the scan planes onto the co- and cross-polarization axis of the image plane. This algorithm is based on the principles outlined in section 1.7.2, and uses a Nelder-Mead minimization function (Nelder and Mead 1965) acting upon the scale factor $Ae^{i\phi}$. The pipeline's polarization function gets passed a initial value for A and ϕ, and solves equation (1.12) over a set range of projection angles θ_{proj}. The function exits when it converges on a solution that minimizes the total power in the cross-polar radiation pattern $|\vec{E}_x|$. Initially, a subset of 100 pixels in the center of the FPA were fed into the algorithm in the range $-\frac{\pi}{2} < \theta_{proj} < \frac{\pi}{2}$ with increments of $\frac{\pi}{180}$. Once the average projection angle was found we ran the algorithm over the full array but narrowed the projection angle range to $-\frac{\pi}{6} < \theta_{proj} < 0$ with increments of $\frac{\pi}{360}$.

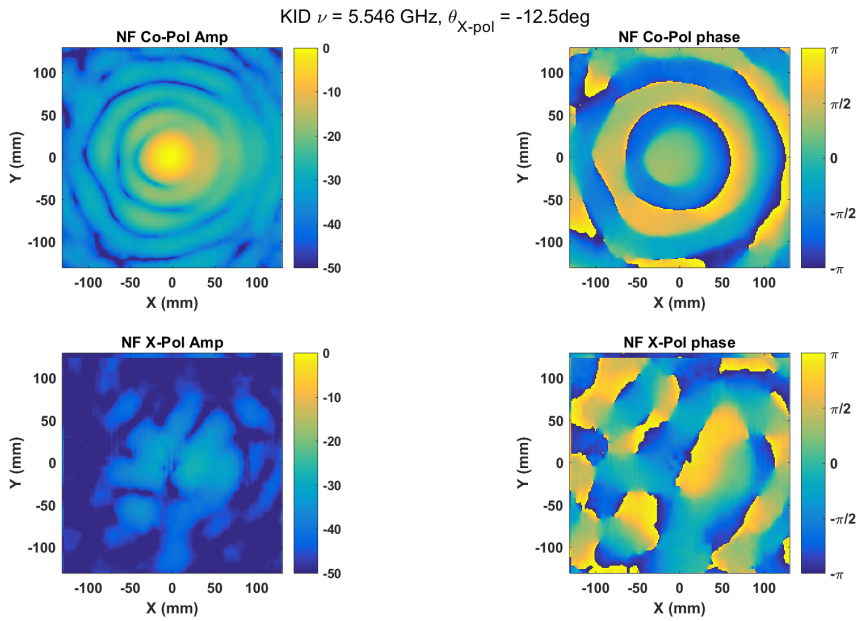

Figure 3.4. Near field co-polarization (upper two panels) and cross-polarization (bottom two) panels. The left two panels show the amplitude, scaled to the peak of the co-polarization map, and the right two panels show the phase structure. The image has been cropped to a square 8x the beamwidth centered on the amplitude peak in the co-polarized map to cut out the wide-field noise.

Because the raw data maps were scanned over a large field of view relative to the individual beam size (as seen in figure 3.2) and include an elevated off-axis signal, we select only a inner portion of the raw data map to pass to the fitting routine. To find the best size for the selected region, we centered a box of scan coordinates with side length $\ell = \omega(z) * bw$, where $bw = 5...10$, around the amplitude maximum of the beam. At the edges of the array, the region size of $\ell \times \ell$ points is maintained but is shifted to begin at the edge of the scan plane, meaning that the amplitude centroid of the map may not be in the center of the selected region. Because of this, the raw data scan extends well beyond the edge of the field of view of the array, and only a small fraction of pixels have centroid positions significantly far from the center of the selected region.

We pass this scan region to the co-and cross-polarization finding algorithm over a subset of 10 KID pixels and calculated the average integrated $|\vec{E}_x|$ as a function of bw. We found the difference between integrated $|\vec{E}_x|$ (scaled by the area of the selected region) as a function of bw did not vary significantly, and so we chose $bw = 8$ as a trade-off between region size and computational time. This area is large enough to include at least 2 phase wraps in the selected scan region, which is used to determine whether these points were actual wraps caused by the spherical phase roll-off or from nulls in the amplitude map where phase jumps due to the sign change in the complex field map.

In order to minimize $|\vec{E}_x|$, the amplitude centroid of the two maps $\vec{E}_h$ and $\vec{E}_v$ must be co-aligned as accurately as possible. The raw data maps were gridded onto a 1 mm spacing, but this sampling was too course to see the fine detail of the cross-polarized maps. We then linearly interpolated the data onto a 0.2 mm grid spacing and used a cross-correlation routine to find the amplitude centroid offset between the two map orientations. The co- and cross-polarization finding algorithm uses a circular shift to co-align the two datasets, for the selected region surrounding the amplitude maximum.

The angle θ_{proj} is determined for each pixel individually. Doing so allows us to search for trends in cross-polar angle as a function of pixel position across the array, such as a misalignment of the lenslet array to the MKID array. We find that the average rotation angle across the array is $\theta_{proj} = -14.9 \pm 0.1^\circ$. Figure 3.4 shows the resulting $\vec{E}_c$ and $\vec{E}_x$ fields of a central array pixel in both amplitude and phase after the above routine was performed. The cross-polar maximum was -21.3 $\pm$ .9 dB below the co-polar field maximum on average across the array. After the projection angle was fit for the region $\ell \times \ell$ for each pixel, the projection was scaled to the entire region of 260 $\times$ 260 mm.

Table 3.1. Beamfitting Parameters and Fits

Fitting Parameter	Initial Value	Average
$\omega_{o,x}$ (mm)	3.25	3.59±0.03
$\omega_{o,y}$ (mm)	3.25	3.54±0.03
x (mm)	x_{NFmax}	–
y (mm)	y_{NFmax}	–
z (mm)	-1.0	-33.6±0.6
θ_{TB1} (°)	0.0	0.2134±0.0005
θ_{TB2} (°)	0.0	0.2843±0.0005
θ_{TB3} (°)	0.0	0.5± 0.2

The beamfitting parameters used to calculate the Gaussicity of the individual pixel beams. The middle column shows the value used to seed the initial minimization algorithm, and the right column shows the average values and uncertainties across the array.

3.4.2 Data Analysis

3.4.2.1 Beamfitting

In the co- and cross-polar extraction pipeline process, the input full range pre-processed maps were clipped to a region around the amplitude centroid, interpolated to a finer grid sampling, and then the $\vec{E}_v$ was circularly shifted to match the other polarization. The shifted data was passed to the co-and cross-polar projection finding algorithm. Because the scan region encompassed in the original region of size ℓ terminates in the noise floor of the amplitude map, the effects of circularly shifting the maps do not significantly affect the beamfitting routine. However, since the data was interpolated to a fine grid sampling, the region contained a large number of scan points and it was computationally expensive to process the entire array. To ease the computational burden, we further clipped the data to a new region of size ℓ'. The size of ℓ' was determined by testing the same subsample of pixels and analyzing the

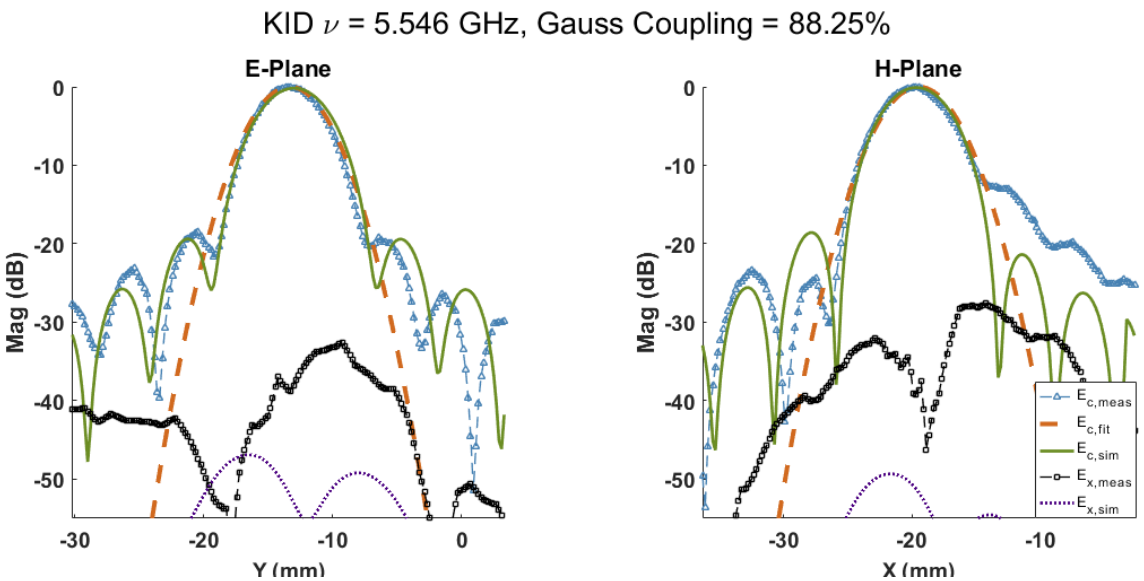

Figure 3.5. Cuts in both the $\hat{E}$(left) and $\hat{H}$ (right) planes of the near-field 2D co-polarized beam patterns, $|\vec{E}_{c,meas}|$, as presented in figure 3.4. We also plot the results of the fitting function $|\vec{E}_{c,fit}|$, which is the first order Gaussian function $|\psi_{00}|$, and the beam pattern cross-cuts from optical simulations $|\vec{E}_{c,sim}|$. The simulated patterns include the effects of the truncation of the beam on the secondary mirror and more fully simulate the optical properties of the receiver system. We see a strong null in the measured cross-polar pattern $|\vec{E}_{x,meas}|$, showing that we recover the cross-polar pattern after re-projection. The measured cross-polar peak is 15 dB higher than simulated $|\vec{E}_{x,sim}|$. This is likely caused by coupling to stray-light in the device substrate as well as residual cross-polarization signal from the stationary source probe pattern. However, at a peak value of $\sim$ -28 dB, this level of measured cross-polarized signal is good for a fabricated instrument.

beamfitting parameters as a function of region size, starting with a severely clipped size of $bw = 4$ and increasing in size until the beam parameters converged to a stable value at $bw = 7.2$ corresponding to a box of size 33.8 $\times$ 33.8 mm centered on the amplitude maximum of the beam.

The beamfitting analysis routine used in our pipeline is a scaled version of that presented in (Davis et al. 2017) and (Jellema 2015), following the procedure described in section 1.7.3. It fits for the fundamental beam parameters $\omega_{o,x}, \omega_{o,y}$ by creating a

new coordinate system at location x, y, z and rotated with respect to the scan plane by $\theta_{TB1}, \theta_{TB2}, \theta_{TB3}$ from which to propagate an idealized, fundamental Gaussian beam ψ_{00}. The angles $\theta_{TB1}, \theta_{TB2}, \theta_{TB3}$ are Tait-Bryan angles. A minimization function takes the set of initial seed parameters to set a coordinate system an Gaussian beam, propagates the beam forward to the image plane, calculates the coupling loss coefficient between the measurement and fit data, and iterates over the parameter space until a convergence criteria is met.

Here, we use a two-step minimization approach that optimizes the search for a global minima over the parameter space but efficiently solves for the uncertainties in the fit parameters. Initially, we use an unbounded Nelder-Mead (Nelder and Mead 1965) minimization function to solve for equation (1.13), which can efficiently probe the parameter space and has a low chance of getting stuck into local rather than global minima. We use the output parameters of that function to use as an initial guess for a non-linear least-squares minimization function (Marquardt 1963), which is also unbounded. The least squares algorithm allows us to more easily find the confidence intervals for the solution set of beam parameters. In order to process the entire array efficiently, the beamfitting algorithm of the pipeline was re-optimized to run using parallel processing techniques. This was possible because the fitting routine is independent to each pixel. The search routines both used a nested function approach to pass the measurement data into the minimization routine without being optimized as a fitting parameter. The beamfitting step of the data processing pipeline can run in under two hours when running on four parallel threads.

Table 3.1 shows the initial values used to seed the minimization algorithm used for beamfitting, as well as the average of the final fit values for all 718 matched pixels. Initial parameters for the beam characteristics were taken from an idealized,

symmetric first order Gaussian beam with a magnification at the image plane of 3.0 and perfect alignment between the scan plane and image plane. The exception to this is the fit in z. During testing of a small subset of pixels, we found that setting this parameter initially to zero caused the algorithm to get stuck in an unrealistic local minimum at $z = 0$, meaning the scan plane was precisely located at the focal plane of the optics system. We therefore seed it with an initial distance of 1 mm, and it converged to the global minimum near -33 mm.

Figure 3.5 shows the results from the beamfitting analysis for a representative pixel. Here we show only the amplitude of the co-polar map, though we also fit the phase map. We include the measured data $|\vec{E}_c|$ as well as the magnitude of the idealized first-order Gaussian beam $|\vec{E}_{ideal}|$ from equation (1.4). We also include the results of optical simulations using the parameters from lens-antenna simulations in CST (*CST Microwave Studio* 2016) which were then ported into GRASP (*GRASP* 2017) for full end-to-end beam pattern simulation. The fit in both amplitude and phase is shown both across the region selected for the array as well as for a cut in both the E-and H-plane. Because we use a first order Gauss-Hermite polynomial for fitting, we do not fit for side lobes. We discuss the choice of fitting function in section 3.5.

Figure 3.6 show the coupling coefficient between the co-polar map and the first-order Gaussian beam. Optical simulations predicts a 85% coupling (*Zemax* 2017). We see no significant trend between coupling and pixel position, although we have eliminated pixels for which the beamfitting algorithm did not converge to a solution, which typically signifies crosstalk in the beam.

Initial testing of the beamfitting algorithm included another independent parameter, used when processing the data presented in Davis et al. (2017). This value parametrizes the beam's astigmatism, which is the offset between the phase centers in the x and y

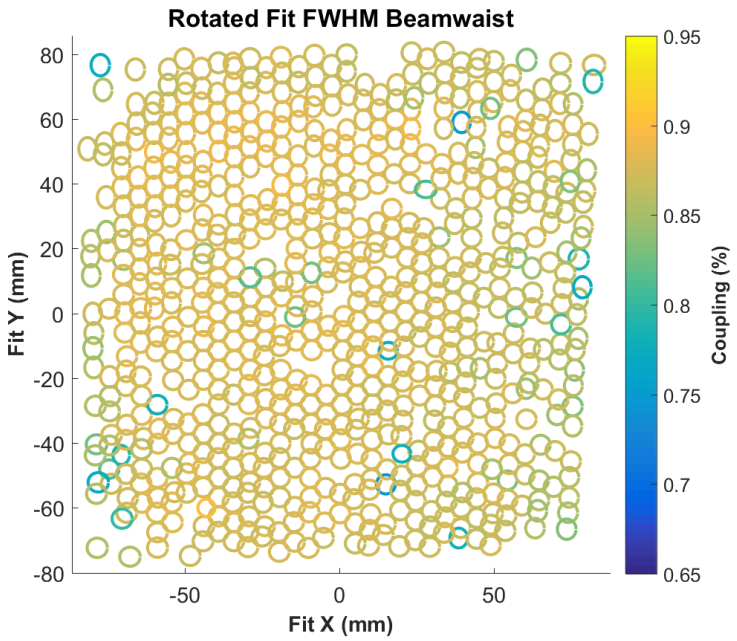

Figure 3.6. This plot simultaneously shows the beam ellipticity and coupling coefficient for each pixel across the array. We have filtered out all pixels for which the beamfitting algorithm does not converge. The shape of each beam is proportional to ω_x and ω_y at the distance z fit for each pixel according to the coordinate system transformation outlined in section 3.4.2.1. The color of each beam is proportional to the coupling value c_{00} from equation (1.13).

direction (parameter $\delta z_{x,y}$ as defined in (Jellema 2015)). However, when analyzing the beamfitting equation, we find that the function is fairly insensitive to the z parameter, where a 10 mm change in z produces only a $\sim$ 1% change in the beam coupling. Upon further inspection, we found that the minimization function was oscillating between two minima for different values of z and $\delta z_{x,y}$, thus these two parameters are not sufficiently independent for the level of noise present in this dataset. Thus, we removed this parameter from the fitting routine and kept the fit in z only. We still solve for the beam ellipticity by independently fitting the beam along the x and y axis, to find ω_x and ω_y. The ellipticity as a function of pixel position is shown in figure 3.7

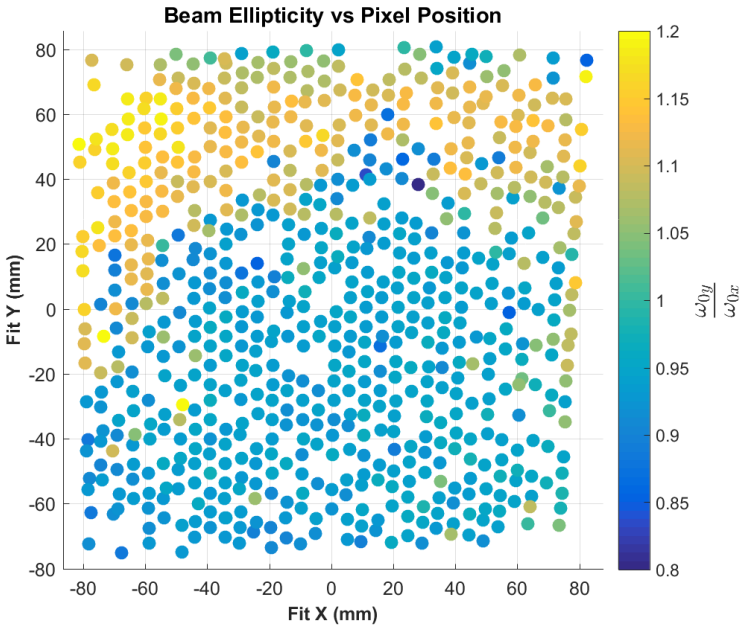

Figure 3.7. Ellipticity as a function of pixel position across the array. Each pixel is represented by a uniform circle, and the color of each pixel is related to the ellipticity. We do see a trend across the array, from $\omega_y > \omega_x$ toward the bottom half of the array, and $\omega_y < \omega_x$ trending towards the upper half of the array. The origin of this trend is still unclear.

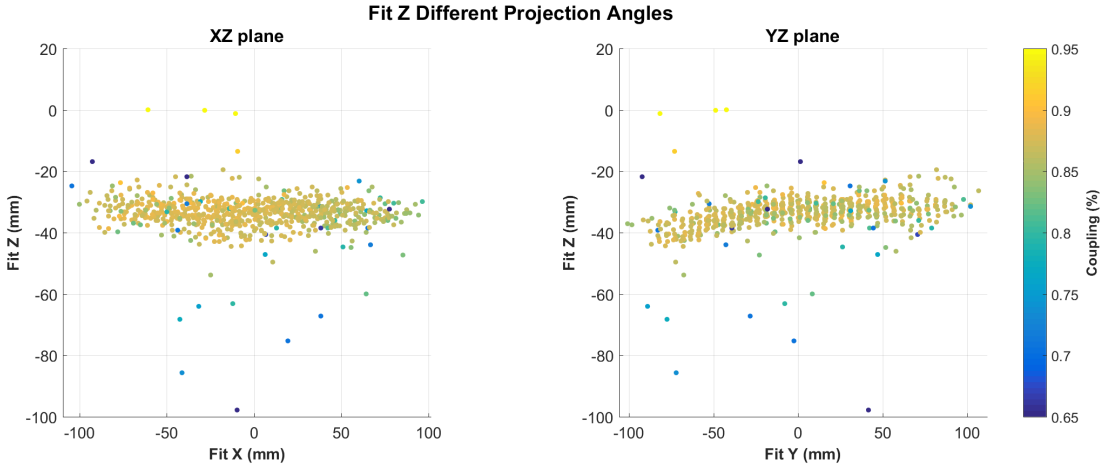

Figure 3.8. Projection of the z-fit parameter as viewed from the XZ (right) plane and YZ (left) plane. Again, the color of each pixel is related to the coupling percentage. The results of this plot demonstrate there is a slight defocus on order of 3 cm of the measurement plane with respect to the external optical focal plane.

Figure 3.8 shows the value of the fit in z as a function of pixel position. The mean fit distance was -33 mm. This fitting parameter is effectively the distance of the measurement plane from the focal plane of the optical system, fit individually for each pixel. At this distance we are just outside the confocal distance of $\sim$ 20 mm. We do not see a flat focal plane, rather there is a spread of $\pm$ 6 mm. However, as we described earlier, the sensitivity of the algorithm is only weakly coupled to the distance in z, and this spread falls within the noise level of the fitting algorithm.

3.4.2.2 Near- to-Far-Field Transformation

We take advantage of the external focus of the AMKID optical system to measure the complex beam pattern in the near field. We then solve for the far field beam pattern following an angular plane wave spectrum technique detailed in section 1.7.4, which is accomplished with a Fast Fourier transform (FFT). Instead of clipping the data in a boxed region as for the beamfitting pipeline process, we apply a circularly symmetric Hanning window function over the full 260 $\times$ 260 mm co-polar map. The windowing region is centered on the amplitude maximum and has a radius of $r_{Hann} = 24$ mm.

Because we use the full scan plane data to transform the near field data, the amplitude maximum is not at the center of the measurement plane. Because of this, the transformation will propagate from the center of the scan plane rather than the center of each beam, and the far field transformation will show a phase tilt which appears 'striped'. We mathematically correct for this projection by shifting the phase by equation (1.21).

The upper two panels of figure 3.9 show the far field amplitude and phase of the co-polar field, and the bottom two panels show the amplitude and phase of the

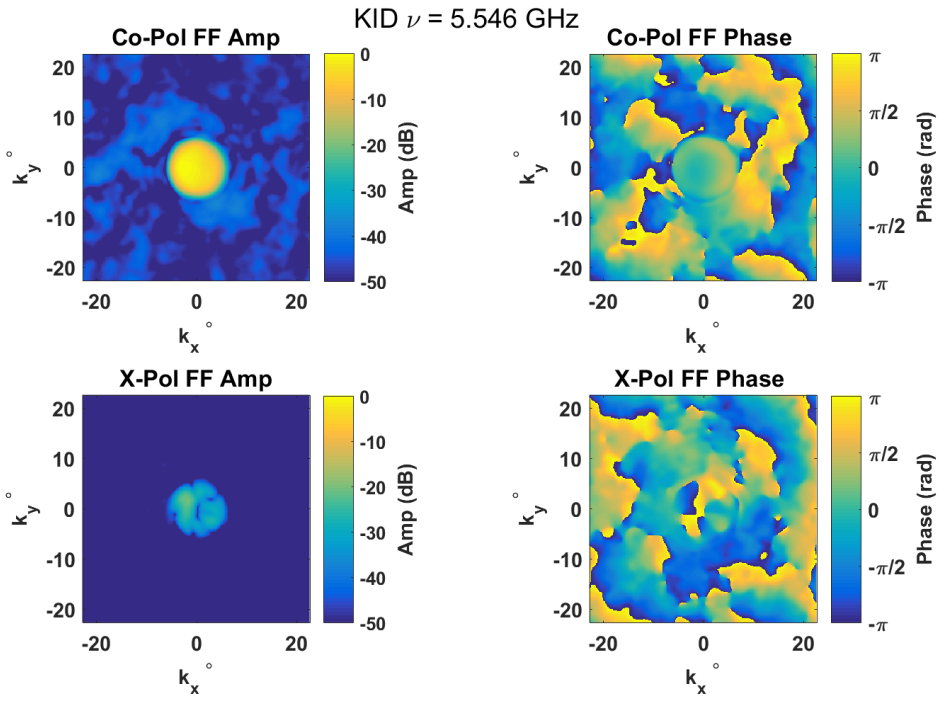

Figure 3.9. Far field radiation patterns of the representative MKID pixel. The upper two panels are the co-pol far field, lower two panels show the cross-pol far field. The left two panels are the amplitude patterns and the right two are the corrected phase patterns. We recover a null in the central region of the cross-polar amplitude map, demonstrating that we do indeed fit for the proper cross-polarization field even at an elevated signal compared to the design.

cross-polar field. The far-field pattern represents the illumination of the beams at the aperture stop of the optical system (ie the secondary mirror of the telescope). Though it appears to be mostly flat, the field in the central amplitude region of the co-polar far-field projection is a truncated Gaussian with an edge taper of $>\sim$-5 dB on average across the array. The array under test was designed with a -3dB taper, to enable oversampling of the focal plane (Griffin et al. 2015). We see some very-low level diffraction effects present in the amplitude of the co-polarization maps from the high truncation of the beam at the optical pupil of the instrument.

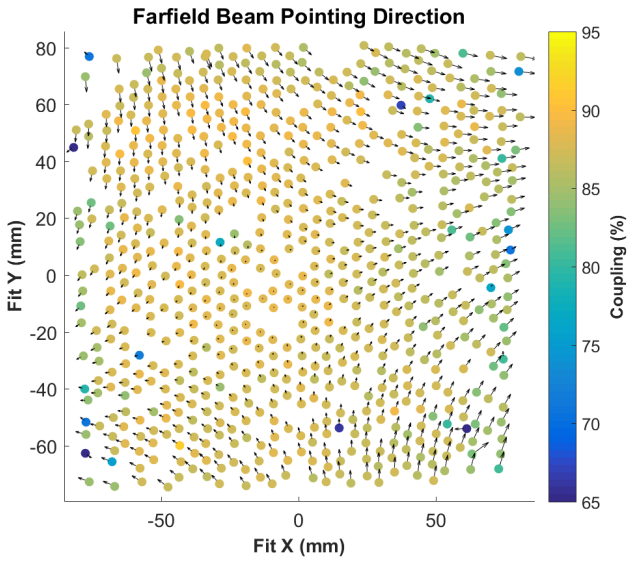

Figure 3.10. The black arrows overlaid on the central dots point in the direction of the boresight angle. The length of the arrow is proportional to the magnitude along the pointing direction, but scaled by a factor of 25 to be visible across the plot. The color of each pixel is proportional to the coupling % of the pixel, and does not correlate to the pointing direction. The beams have to be scaled by a large factor to show the pointing direction, demonstrating that overall the beams are very well aligned to the optical axis.

Once the phase correction has been applied, we find the phase center in angular coordinates k_x, k_y by setting all coordinates of the co-polar map with amplitude > -10 dB to unity and nulling all coordinates with amplitude < -10 dB. We then average all the coordinates with signal to find the central coordinates of the beam, which correspond to the boresight angle of each pixel fitted in the far field. The angle as a function of pixel position is shown in figure 3.10.

3.5 Results

The far-field co-polarized beam map confirmed the secondary edge taper of only -3 dB, verifying the optical design of the system at planes other than the measurement

plane. Where possible, we take advantage of fitting routines and mathematical field transformations to achieve a complete radiation pattern measurement to find the co- and cross-polar patterns and beam pointing angles from two measurement scans (though for this antenna under test the readout equipment had only enough bandwidth to read out half of the array per measurement scan, thus requiring a total of four scans).

As a result of the complex field radiation pattern measurement, the AMKID array was measured with a dynamic range of >50 dB, a factor of 2-3 orders of magnitude improvement over similar radiation pattern measurements taken using only a thermal source. Initial complex field pattern measurements of an early fabrication run of the AMKID array revealed the presence of a -40 dB optical surface wave. The surface wave was removed by adding an absorbing mesh for subsequent fabrication run (S. J. Yates et al. 2017). The results we present here are measurements from an array fabricated with an absorbing mesh in the substrate. Our results show a decrease in the magnitude of the surface wave to ∼-50 dB. Complete removal of the surface wave can potentially improve the dynamic range even further.

This pattern found in both the near field beamfitting and far field pattern confirms the fact that the beams are only somewhat Gaussian in nature; the highly truncated beams are therefore dominated by diffraction effects through this stop. The choice to fit for a Gaussian beam stems from the desire to know the coupling to a point source for each individual pixel. In this analysis with the AMKID array, the fundamental beam produced by the lenslet array was designed to produce more Gaussian beams, but the significant truncation at the pupil degrades the Gaussian coupling produced at the image plane. It is therefore important to propagate the beams from the near-field into the far-field to check the edge taper at the secondary in order to accurately

characterize the performance of the array. This step is only effective with complex-field measurements.

We could in principle recover different information about the optical system by fitting for a diffracting function, for example, a first order truncated 2D Bessel function (Yousif and Melka 1997), (Functions et al. 2012), (Lucas and Stone 1995). The framework presented here is easily adaptable to other fitting functions while maintaining an approximately equal degree of computer processing time. The memory allocation requirements for the beamfitting step in the processing pipeline scale with the number of fitting variables used by the particular equation.

In the fitting algorithm we present, six variables are used to transform coordinate systems between the scan plane and image plane, and two variables are beam parameters. Two additional beam parameters were used to fit for the real and imaginary energy contained in the field when using the least-squares fitting routine, and another beam parameter describing beam astigmatism was removed from this analysis due to the ambiguity between distance to the focal plane and the distance to the beam phase center. This ambiguity is partially caused by the presence of the residual surface wave in the array substrate, so for arrays with more stray-light absorption or anti-reflective coatings, this parameter can be added back to the processing pipeline.

The most computationally expensive task in the processing pipeline is the step to match the MKID readout timeseries to the phase reference (blind tone) signal and convert the timeseries into a complex field measurement. This step is also the most significant data reduction. The limitations of this system are set by the memory and processing power of the machine running the analysis. The data here was reduced in post-processing and was performed on a modest system on a desktop machine. It is possible to conceive of a bench-top environment to run this processing in real time,

but since these results are useful for laboratory characterization only, it may not be practical to implement.

This level of detailed analysis will be crucial to ascertain the accuracy of instrument fabrication when looking to the future of space missions using direct detectors with thousands to hundreds of thousands of pixels. For example, the next generation of CMB mapping satellites envisioned for CMB-S4 need unprecedented pointing knowledge to detect or set limits for the energy in primordial B-modes of CMB photon polarization. For imaging instruments studying extended sources, accurate pointing knowledge of the beams is necessary to fully reconstruct the source. The technique we present here is a highly accurate and efficient measurement of the co- and cross-polarization fields of an instrument and can be located at any scan plane convenient for in-situ beam scanning.

3.6 Conclusions

A phase mapping technique for direct detector arrays has been demonstrated and has sufficient sensitivity and accuracy to determine fundamental beam parameters of the individual pixels as well as the optical performance of the system. New analysis techniques were included in a data reduction pipeline for beam pattern characterization of direct detector arrays, including extracting co- and cross polarization maps from data scanned with an arbitrary source probe polarization orientation and near-to-far field optical propagation.

Chapter 4

CIRCULAR TO RECTANGULAR THZ WAVEGUIDE TRANSFORMERS

Abstract

The best way to understand interstellar cloud processes is to study the light emitted directly from the cloud. Indirect methods, for example by studying the extinction of light emitted from background sources, can be very challenging to separate the background environment and radiation conditions from the properties of the cloud. Instead, we use heterodyne cameras to study the spatial and spectral information of interstellar clouds as they cool and condense. Ballooning missions in particular offer a unique opportunity to study the lifecycle of interstellar clouds because at ballooning altitudes of $\sim$ 40 km (125,000 ft), the observation platform is above 99% of the Earth's water vapor, which absorbes a significant fraction of the light entering Earth's atmosphere in the THz regime, limiting the spectral coverage and depth of observations for ground-based observatories. Survey missions are especially advantageous from ballooning platforms because they offer ample observing time dedicated to a single science case and have modest budgets so new detector technology in the THz regime can be tested without the rigorous testing common to satellite missions.

According to Plank's law in equation (1.1), most astronomical bodies emit blackbody radiation within the THz range of the spectra. Though this emission is great for studying astronomical sources, it can be problematic from an instrumentation standpoint, since the environment around a telescope, and even the telescope's optical components themselves, will emit THz radiation that adds noise to the sky signal along the optical path. Instrument scientists are aware of

this phenomenon, and use an equivalent thermal noise to characterize all sources of noise in a system, due to blackbody radiation or not. Various sources of electronic noise are typically converted into units of noise temperature, which is the equivalent noise of a resistor at a temperature T over a bandwidth $B = \Delta\nu$. In order to observe an astronomical target, the incoming radiation from that source must obtain a sufficiently high signal-to-noise ratio over the accumulated thermal noise added to the optical path of the instrument, characterized as T_{sys}. The radiometer equation gives the relationship between observation bandwidth $\Delta\nu$, integration time τ_{int}, and the telescope and receiver's T_{sys}

$$\sigma_{RMS} = \frac{kT_{sys}}{\sqrt{\Delta\nu\tau_{int}}} \tag{4.1}$$

where σ_{RMS} is one standard deviation above the RMS of the Gaussian noise floor of the instrument, and k is a constant equal to 1 or 2, depending on the instrument type (see Walker 2015b, chapter 8). Cooling emission lines of clouds in the THz frequency regime are relatively weak, so high signal-to-noise observation requires a long integration time. Ballooning missions have only modest primary mirror diameters (≈1 meter or so) and low pixel counts (single pixel up to 2×2 arrays demonstrated on-sky), so the best way to improve signal is to make each individual pixel as sensitive as possible.

There are several ways to achieve high pixel sensitivity, but one easy and cost effective approach is to have highly efficient feedhorns that funnel photons from the observatory's optical system and onto the detector chip. For the original proposal of the Stratospheric Terahertz Observatory (STO-2) mission, the focal plane of Hot Electron Bolometer (HEB) detectors was baselined to use diagonal feedhorn profiles. These profiles are cost effective to manufacture by direct-metal micro-machining processes, which is a lot faster and cheaper than other methods such as electroforming or etching. However, a diagonal feedhorn suffers from

a 15% sensitivity loss (only 85% of incident photons are detected) because the feedhorn couples to cross-polar radiation, which contributes to the noise in the detector.

The motivation for this work is based on instrument development to survey large regions of the galaxy in the astrophysically important [CII] cooling line of the interstellar medium at 158 μm (1.905 THz) Goldsmith et al. 2012. Line emission surveys do not require receivers with large fractional bandwidth, but do require the highest mapping speed and spectral resolution available. Thus, it becomes important to develop technologies that can expand large focal plane arrays of heterodyne receivers.

The technology discussed in this chapter has been used for several missions to design feedhorns for heterodyne HEB arrays, at multiple frequencies and with multiple feedhorn profiles, including STO-2, the Galactic/extragalactic Ultra-long duration Stratospheric Terahertz Observatory (GUSTO), and Super Heterodyne Array for Space Terahertz Applications (SHASTA) missions. This chapter introduces a method for integrating a circular-to-rectangular waveguide transformer into the feedhorn block, such that the transformer can be machined from within the aperture of the feedhorn. Micro-machining is much more cost effective than electroforming, making large arrays quick and relatively inexpensive to manufacture. The micron-sized dimensions and tolerances of these horns require new fabrication techniques. Consideration of the machining processes ensure the designs are easily repeatable and can be scaled from engineering models to large arrays with hundreds to thousands of pixels.

4.1 Background

Recent terahertz (THz) heterodyne instruments for astronomical research have utilized horn-coupled receiver devices (Walker 2015a; Bernasconi et al. 2010; Risacher et al. 2016; Dober et al. 2016). For astronomical receivers, it is generally desirable to use a feedhorn to maximize signal coupling to the detector and minimize cross-polarization. Many of these receivers are designed to use rectangular waveguide feeds. This criteria has been used to determine the feedhorn profile. Many instruments have adopted diagonal feedhorns as a standard profile due to their machinability and low cost to manufacture (Johansson and Whyborn 2000). Diagonal horns intrinsically have rectangular waveguide feeds, so they integrate easily with rectangular waveguide fed detector chips. However, diagonal horns suffer in efficiency because of their high cross-polarization component, which can be as high as 15%.

Corrugated feedhorns offer some of the highest sensitivity and lowest cross-polarization (Robertson et al. 2016) but conventional manufacture via electroforming is both costly and time consuming, making them impractical for large array instruments. Other feedhorn profiles, such as Pickett-Potter horns (Pickett et al. 1984) or multi-flare angle horns (Chahat et al. 2015), offer a simpler fabrication process compared to electroformed horns and have lower cross-polarization than diagonal horns, and so are more suitable for low-cost submillimeter array instrumentation.

Both of these feedhorn profiles have circular exit waveguides, so a waveguide transformer is required to integrate them with rectangular waveguide-fed devices. We aim to create a feedhorn module that can integrate with rectangular waveguide-fed detectors, is comparable in performance to a corrugated feedhorn, and uses a

fabrication technique that is within the budgetary and schedule constraints required to manufacture large focal plane arrays.

Circular-to-rectangular (CTR) waveguide transformers (WGT) in the THz frequency range have been produced using direct-metal micro-machining techniques, as reported in Chahat et al. 2015. Two conventional strategies exist for integrating direct-metal micro-machined CTR WGTs into a receiver chain: machining the transformer onto a separate thin plate inserted between the feedhorn and the detector block, or integrating the transformer with the feedhorn block using a split-block technique. In the former case, the transformer segments become increasingly difficult to manufacture at short wavelengths. As an example, the 1.9 THz transformer presented here is only 46 μm thick. A plate of this thickness is susceptible to buckling or warping from being held rigidly in the machine while cutting the transformer. With multiple receiver segments, the mated system is more susceptible to misalignment between the transformer, the detector housing, and the feedhorn blocks. In the latter case, using a conventional split-horn fabrication technique introduces the potential of misalignment between the two halves of the split-block upon mating.

We present a better solution of integrating the CTR WGT directly into the monolithic feedhorn module, making all machining cuts directly from the aperture side of the block. One advantage of this technique is that it decreases machining time because the part can be inserted into the machine workspace and remain in place for all or most machining passes. Each time a part is removed and reinserted into the workspace, a new reference calibration of the machine's positioning system relative to features on the part must be made. The reference calibration can be on the order of a few to tens of microns. Such large deviations can lead to alignment errors between the waveguide segments, and these errors scale with increasing frequency and

the number of individually machined pieces. In contrast, modern milling machines can reliably hold alignment accuracies to <5 μm during a machining pass with a single reference calibration. Thus, the machining strategy presented here can decrease machine worktime and maximize alignment between waveguide elements, helping to advance future instrumentation in the THz regime towards heterodyne arrays of hundreds to thousands of pixels.

4.2 Module Design

There are several feedhorn profiles with circular waveguide feeds that meet the criteria for having high sensitivity, low cross-polarization, and are capable of being made with direct metal manufacturing processes. The optical performance of these feedhorns is well-documented, and is outside the scope of this paper. We therefore have chosen a feedhorn profile to use as a proof-of-concept demonstration, and concentrate our analysis on the design and performance of the CTR WGT.

The design of the CTR WGT is itself conventional, but we use the novel approach of integrating the segment at the rear of the receiver feedhorn by machining it directly from within the feedhorn aperture. We will therefore discuss the details of the manufacturing technique as well as comparing the performance of the integrated feedhorn-transformer module to diagonal feedhorns, which have comparable machining complexity and scalability to large focal plane arrays.

4.2.1 Feedhorn Selection

We choose Pickett-Potter feedhorns as the horn profile for this demonstration. Our design is the same as that introduced in Pickett et al. 1984 scaled to $\lambda_o = 158\mu$m, and the exact values are listed in Table 4.1. CST simulations of the feedhorn have a FWHM beamwidth of 12.3°, -32.6 dB side lobe levels, and cross-polarization coupling of -32.2 dB relative to the main beam. The fractional bandwidth is approximately 10%, which is suitable for emission line surveys. Pickett-Potter horns have a flat-topped conic profile, allowing them to be machined with tools that are custom-ground but do not require electroforming, adhesives, or etching methods. Other direct machined horn profiles are suitable for this module, such as multi-flare horns Chahat et al. 2015, but the increase in bandwidth of these horns is not necessary for emission line studies and may not generally justify the increased complexity and customization of the tooling required for fabrication.

4.2.2 Transformer Design

The design of the CTR WGT is based on Stuchly and Kraszewski 1965, with the dimensions of the cross section scaled in frequency for operation at 158 μm. The feedhorn choice defined the input CWG dimensions at the input of the CTR WGT. This design was chosen over other CTR WGT designs (Rosenberg, Bornemann, and Rambabu 2002; Zhao et al. 2016; Holzman 2005; Munir and Musthofa 2011; Pawlan 2015) because the features get progressively smaller from the circular to rectangular waveguide, allowing all features to be machined from a single side of the feedhorn

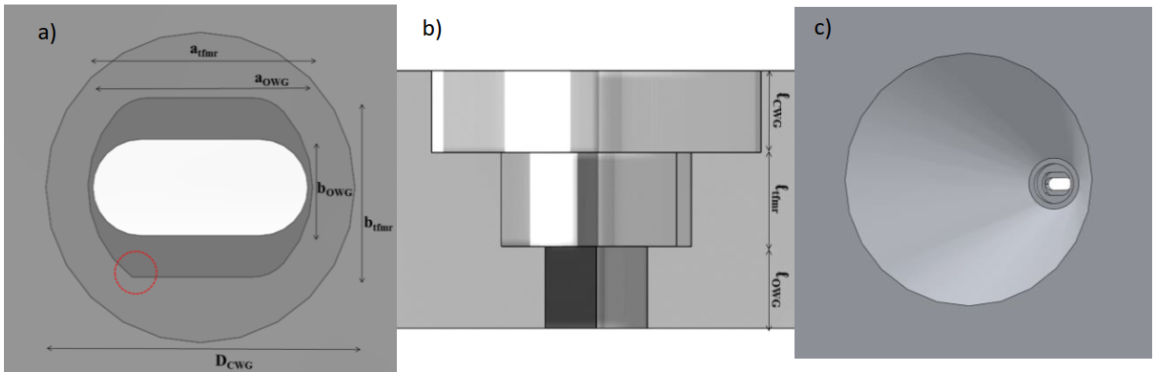

Figure 4.1. Critical dimensions of the model of the waveguide circuitry of the transformer module as seen (a) looking down the optical axis, (b) cut across the profile, and (c) an isotropic view looking down the aperture of the Pickett-Potter feedhorn (c). Dimensions of these features are listed in Table 4.1. The red dashed circle in (a) shows a corner of the transformer that does not have the corner fillet, to demonstrate the difference between the idealized transformer and the edge-rounding required by the manufacturing technique. Similarly, the idealized rear WG would be rectangular instead of oval.

block. Figure 4.1 shows a diagram of the transformer profile, including the circular waveguide exiting the feedhorn.

The dimensions of the CTR WGT were optimized in both HFSS (High Frequency Structure Simulator) (*HFSS* 2014) and Computer Simulation Technology (CST) (*CST Microwave Studio* 2016) simulation packages. The design objectives were to produce a transformer with S_{11} below -20 dB across the 10% bandwidth of the Pickett-Potter feedhorn. Since the input reflection of Pickett Potter horns is well constrained, we chose to optimize only the transformer, circular waveguide, and rear waveguide (see section 4.2.3).

In both simulation packages, we initially optimized the transformer dimensions a_{tfmr}, the circular radius of the curved edges along the width of the transformer, b_{tfmr}, the straight edges along the height of the transformer, and ℓ_{tfmr}, the transformer

Table 4.1. Transformer Module Dimensions

Design	Dimension (mm)	Machined (mm)
D_{horn}	1.011	1.015
D_{step}	0.205	0.208
L_{horn}	1.678	1.669
D_{CWG}	0.161	1.159
ℓ_{CWG}	0.048	0.060
a_{tfmr}	0.117	0.114
b_{tfmr}	0.093	0.098
ℓ_{tfmr}	0.046	0.035
a_{OWG}	0.100	0.108
b_{OWG}	0.050	0.053
ℓ_{OWG}	0.060	0.081

The designed and as-machined dimensions of the feedhorn-transformer module. The as-machined dimensions were verified using a microscope with sub-micrometer precision. The tested unit was measured without cutting it open, so there is ± 0.005 mm uncertainty in the measurements due to diffraction of optical light within the horn.

length, for the minimum achievable input reflection S_{11} at the frequency of interest (1.9 THz). The two packages returned slightly different optimized transformer dimensions. The differences between simulation packages can arise from several factors, including the differences in convergence criteria and meshing algorithms. There may also be difference arising from the fact that CST is time domain solver, which is more suited to represent the scattering parameters across the full bandwidth of the module, but HFSS is a frequency domain solver, which is more suited to finding a solution at a single frequency of interest. We averaged the two optimization results together to produce the dimensions presented in table 4.1. We then re-simulated the module in both packages with the averaged dimensions to ensure there was a -20 dB S_{11} across the frequency bandwidth of the Pickett-Potter horn (1.7-2.1 THz). Figure 4.2 shows a comparison between the S_{11} optimized using each software package. At 1.905 THz, HFSS finds a S_{11} of -33.6 dB, and CST finds a S_{11} of -34.6 dB.

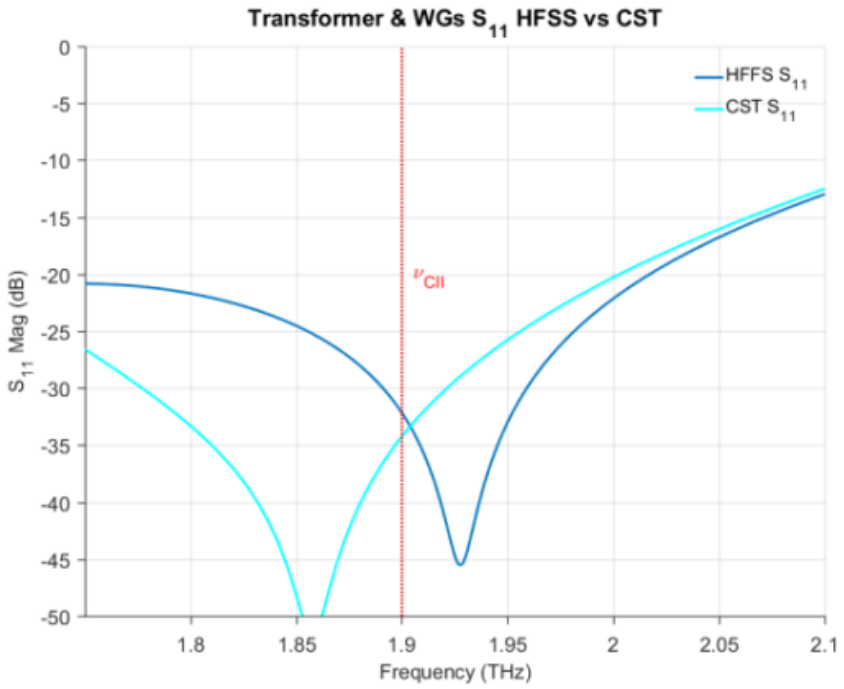

Figure 4.2. Comparison of the S_{11} parameter between CST and HFSS. The red dashed frequency indicates the rest frequency of the CII line at 1.905 THz. Both simulations include the circular waveguide in front of the transformer and an oval waveguide feeding a rectangular waveguide behind the transformer. We included the oval to rectangular transition to simulate the feedhorn-transformer module mated to a receiver block with a rectangular waveguide feed.

4.2.3 Oval (Slot) Waveguide

A consequence of machining the transformer from within the aperture of the feedhorn is that the rear waveguide must be cut with the endmill along the optical axis. In figure 4.1a, the endmill making the waveguide (WG) feature would be sticking out of the page, and it is possible to see how the circular tool cannot make a 90° corner as would be required for a rectangular WG. As a result, the cross section of the exit waveguide changed from rectangular to oval. Similarly, this constraint required us to round (fillet) the edges between the straight and curved transformer walls. The

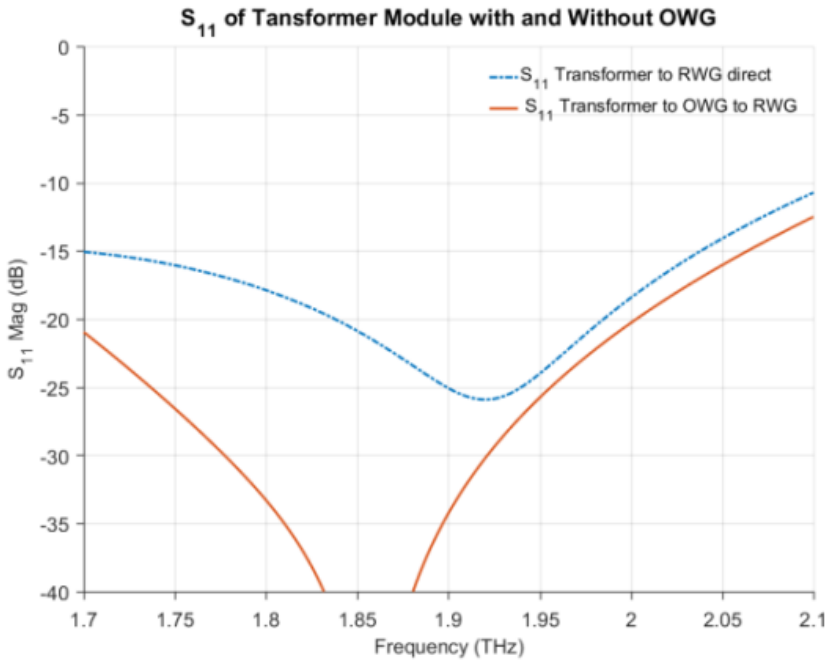

Figure 4.3. Comparison of the S_{11} parameter between a module with a CWG, transformer, and RWG (top curve) and the S_{11} of a module with a CWG, transformer, OWG, and lastly a RWG (bottom curve). The dimensions of the transformer in both curves are those presented in Table 4.1

dashed circle in figure 4.1.a shows the idealized edge, and all other edges are shown with the fillet. The radius of the fillet is determined by the radius of the endmill used to make the cuts. In this case the radius was 22 μm, slightly smaller than $^{b_{tfmr}}/_{2}$ so that there was room to drive the tool while making the cut.

We simulated the effects of using an oval waveguide (OWG) rather than rectangular waveguide (RWG) using CST. We first simulated just the CWG and transformer leading directly into a 0.1x0.05 mm RWG, where the RWG dimensions were set by our test detector (see section 4.4). We then inserted an OWG segment between the transformer and the RWG to simulate the transformer module connected to a block with a RWG leading to the detector chip. Figure 4.3 shows the comparison of the

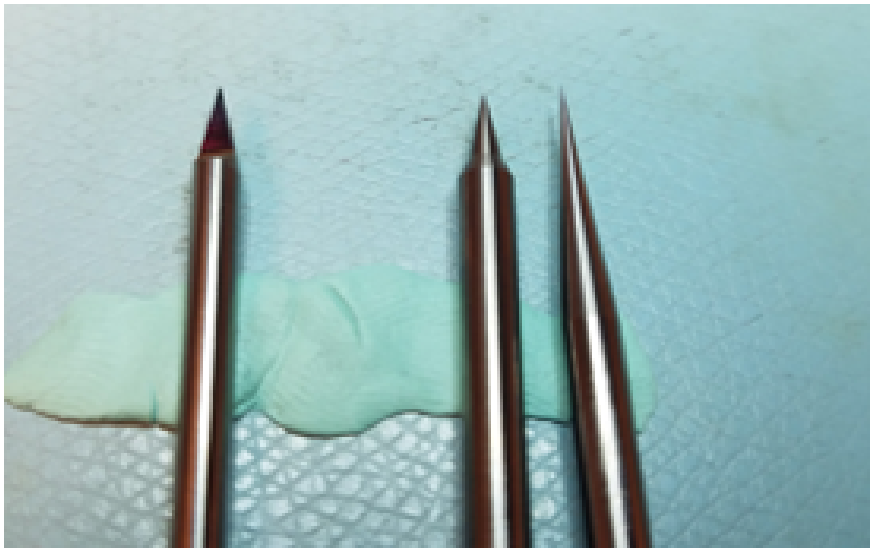

Figure 4.4. Endmills used for the manufacture of the feedhorn-transformer module. The left-most tool is a custom-ground tapered bit ending in a flat step, used for machining the Pickett-Potter feedhorn. The right-most tool is a standard 40 μm diameter endmill that was ground to recess the neck of the tool to fit within the horn aperture. For comparison, the middle endmill shows a standard tool with no specialized necking.

input reflection between the module mated directly to a rectangular waveguide versus a module with an oval waveguide mated to a rectangular waveguide. The module with the OWG inserted performs better than the direct transition to RWG because we have optimized the transformer dimensions to the OWG rather than the RWG transition. Though not the original intent, the OWG is itself a CTR WGT, as was demonstrated in Pawlan (2015), and so the performance increase when the OWG is included is not surprising.

4.3 Fabrication Techniques

It is possible to machine all waveguide circuitry from the aperture of the Pickett-Potter horn with just three tools; one custom tapered tool with a flat end for the feedhorn (shown on the left of figure 4.4), and two additional modified endmills for the CWG and transformer/OWG segments (one shown on the far right side of figure 4.4). To achieve the proper dimensions at 1.9 THz, the horn tool was ground at a 6.5° half angle and the tip was flattened to match the diameter of the step between the horn and the CWG. The endmill used to cut the CWG is slightly smaller in diameter than the CWG (here 150 μm) at the exit of the feedhorn, and the endmill used to cut the transformer and the OWG has a diameter less than that of the short dimension of the output OWG (here 40 μm). The diameter of these endmills is standard but both were recessed at the tool neck in order to fit in the horn aperture. The recessing was done at the Jet Propulsion Laboratory by grinding the tool at the appropriate clearance angle.

The length of each waveguide segment of the module was designed to be as short as possible to minimize attenuation. Short machining depths also minimizes the possibility of breaking the thinner, necked endmills in the waveguide during fabrication. The main drawback to machining all features from the front of the block is that it is at risk of leaving machining chips on any step between the progressively smaller features along the optical axis (the steps from top to bottom in figure 4.1.b).

One alternative machining strategy is to machine the exit RWG from the back of the feedhorn block. Doing so requires that the block be taken from the base, flipped, and re-mounted in the machine. Each time the part is remounted, the alignment of the block to the spindle axis must be re-calibrated, costing significant machining time

and creating the possibility for misalignment. Instead of referencing the location of the rear waveguide to a corner of the block, misalignment can be mitigated by drilling a guide hole down from the bottom of the transformer segment before flipping the part, and using centering microscope to re-align the machine's coordinate system to the guide hole.

In this process the smallest diameter endmill does not require a recessed neck in order to fit within the aperture of the horn. The benefit of this is that the endmill is more rigid, increasing the expected tool lifetime. Machining the OWG from the back of the horn is a trade-off because as the endmill pushes down into the transformer segment, it may push material into the transformer and leave burrs on the step between the two segments, causing unwanted reflections at the transition. We chose this method to manufacture the test horn to avoid modifying the 40 μm endmill.

Figure 4.5 shows the as-machined single pixel receiver assembly. The feedhorn block is connected to the detector backend. A SMA connector coming out of the back can be seen for scale. Two guide pins spaced on the flange ensured precise alignment to the mixer backend. The horn is located in the middle of a 20 mm square block of C145 Tellurium copper alloy.

In figure 4.5b, we see some detectable burs and machining chips visible along the edge of the oval waveguide, though none protrude excessively into the waveguide cavity. We check for reflections caused by these small machining artifacts with radiation pattern measurements, discussed in sections 4.4.3 and 4.5.2. We also see a small rotation between the transformer and the OWG, occurring because during the manufacture of this test unit, not all machining passes were performed in a single step. We believe that the machining process described above will reduce this error.

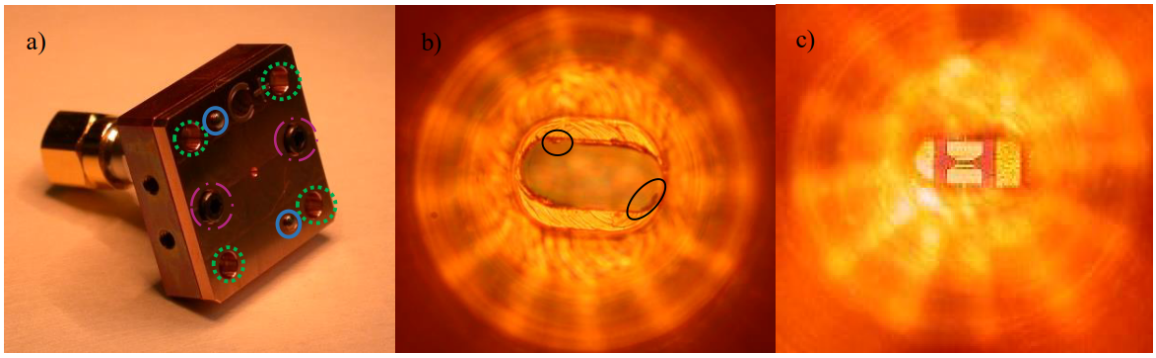

Figure 4.5. (a) Single pixel feedhorn-transformer module connected to the thicker mixer backend. The small circle in the center of the block is the aperture of the Pickett-Potter feedhorn. The green dotted circles highlight the holes to mount the receiver assembly to the cold work surface, the magenta dot-dash circles highlight the screws that connect the feedhorn and detector blocks, and the solid blue circles highlight the alignment guide pins. (b) Looking down the aperture of the horn at the flat surface between the transformer and the oval waveguide. The outer feature is the edge of the transformer and the inner feature is the OWG. The two black ovals highlight the presence of machining artifacts, either burrs or stray machining chips, at the step between the transformer to oval waveguide. (c) The bowtie structure at the bottom of the waveguide is the hot electron bolometer (HEB) detector device, mounted in the detector block and mated with the feedhorn- transformer module. The orientation of the HEB is aligned to the short dimension of this panel.

Despite this rotation, in figure 4.5c, we see good alignment of the detector chip to the optical axis of the horn.

4.4 Measurement System

Though the design requirements we used for the transformer module rely on optimal S_{11} performance, it is impractical to measure the return loss directly, mainly because there are no standard vector network analyzers available at 2 THz. Instead, we measure the performance of the integrated module using noise temperature and radiation pattern measurements.

The noise temperature of the receiver assembly is partially determined by the

return loss of the transformer, although there are contributions to this number from the return loss of the feedhorn, noise from the HEB, cryogenic low noise amplifier, and warm intermediate frequency (IF) chain. We can separate out the noise contribution from the system by performing a comparative measurement between two frontend blocks, each with different feedhorn profiles but both mated to the same detector chip and IF electronics. We have chosen diagonal feedhorns as a comparative feedhorn profile for this analysis due to their similarity in timescale and simplicity of fabrication, and the fact that they do not need a CTR WGT to mate with RWG-fed receiver blocks. There is lingering uncertainty in the contribution to the noise temperature between the feedhorn profiles used for this comparison, so we estimate the relative difference of the feedhorn return loss using simulations of each module.

We use the radiation pattern measurements as a secondary way to verify the machining technique. By itself, the radiation pattern is mostly influenced by the feedhorn. In conjunction with the dimension analysis via microscope, these measurements check that the offset of the oval waveguide and the small burs and chips left from the fabrication process—seen in figure 4.5b do not create obvious distortions in the radiation pattern. We are therefore interested only in the general shape of the radiation pattern and if, to first order, it matches the expected beam radius.

We tested the feedhorn-transformer modules by mating them to detector backend blocks containing Niobium Nitride (NbN) hot electron bolometers (HEBs). The HEBs were scaled from the design presented in Boussaha et al. 2011 to operate at 1.9 THz. The backend block design uses input RWGs and quarter-wave backshorts. Typical devices have a noise temperature of 900 K when used as a mixer device at this frequency.

4.4.1 Diagonal Horn Design

The dimensions of the diagonal horn are scaled in frequency to 1.9 THz from the design presented in Johansson and Whyborn 2000, resulting in the principle feedhorn dimensions $a = 0.38$ mm and $L = 3.6$ mm. This feedhorn was machined using a split-block fabrication technique, and was designed with the same interface connections to the HEB detector block as the Pickett-Potter feedhorn module. This way, the two front-end blocks were interchangeable so that the exact same device was used to measure the noise temperature of both receiver assemblies.

In order to minimize the waveguide attenuation within the receiver front-ends, both front-end blocks were designed to minimize length of each waveguide segment. Intrinsically, a diagonal feedhorn has a longer horn length than a Pickett-Potter feedhorn of the same beam waist, and consequently had a longer feedhorn module. Therefore, to keep the HEB at the same position relative to the cryostat window, we machined two sets of alignment holes with the appropriate offset distance to mate the receiver assemblies to the cryostat mounting structure.

4.4.2 Noise Temperature Measurement System

The dual side band (DSB) noise temperature was calculated using the Callen-Welton Y-factor method (Callen and Welton 1951). The noise temperature was measured with the receiver pumped by a 1.9 THz Schottky-diode based multiplication chain (Siles et al. 2012). A grid beamsplitter placed in the optical path of the receiver coupled 10% of the multiplication chain signal to the receiver beam. Inside the cryostat there are no optical elements between the window and the receiver assembly.

Eccosorb pads at 300 K and 77 K were manually inserted in the source path of the system. The intermediate frequency of the receiver was 1.5 GHz with a bandwidth of 500 MHz. A power meter was attached to the IF connection from the receiver, and multiple hot/cold cycles of the thermal sources were averaged together.

4.4.3 Radiation Pattern Measurement System

Figure 4.6 shows a block diagram of the test bench used to measure the radiation pattern of the feedhorn. For this experiment, we used the devices as direct detectors due to the simplicity of the experimental system, in comparison to using a two source heterodyne technique. The receiver assembly was mounted in a liquid helium-cooled cryostat that was placed on a rotating stage. The HEB location relative to the front of the cryostat is known from both CAD models and direct measurements with the cryostat open, and we used that knowledge to manually align the HEB to the stage's rotation axis. A thermal break consisting of an insulating Mylar sheet was inserted between the receiver mount and cold work surface to keep the HEB just below its critical temperature, $T_c = 9$ K, and fine temperature adjustment was controlled by a resistive heater mounted to the interface block between the cold work surface of the cryostat and the back-end block. An external bias system and read-out electronics were connected to the HEB through a hermetic flange on the cryostat lid.

The radiation pattern measurements were conducted using the same source probe as in the noise temperature measurements. For this test the source was mounted directly in front of the receiver cryostat. We inserted a stationary wire grid between the cryostat and the test source to eliminate the cross-polarization from the source signal. We electrically modulated the source signal using a square wave generator.

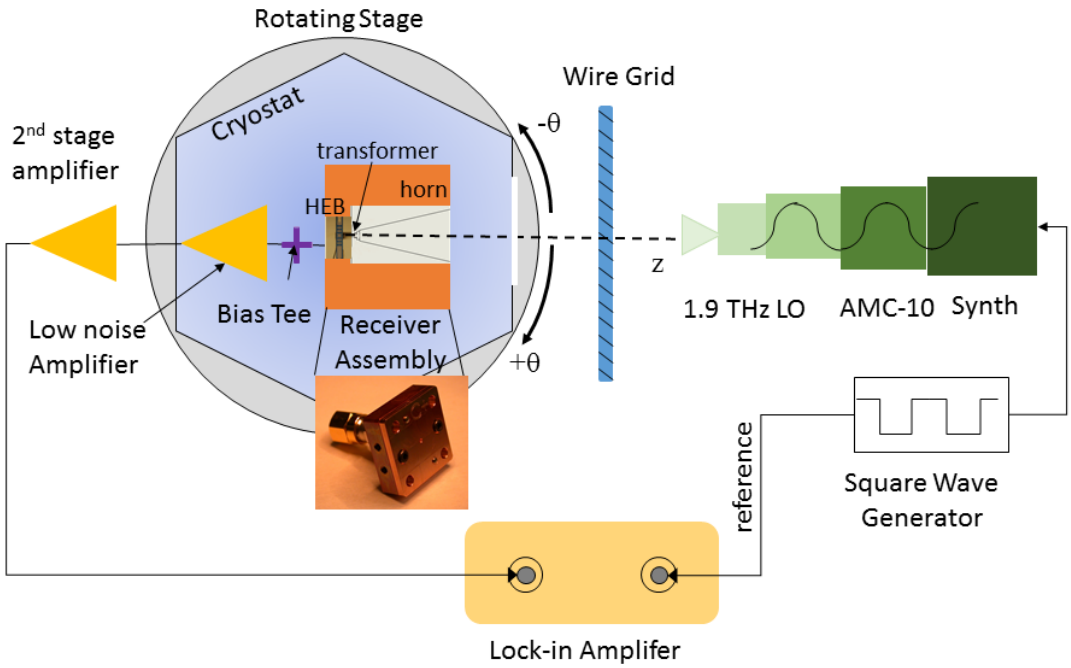

Figure 4.6. Block diagram of the radiation pattern measurement system. Note that the horn profile and HEB image are not to scale relative to the other system components. The small HEB image in the receiver assembly was adapted from Boussaha et al. 2011

The current output from the modulated HEB was fed to a lock-in amplifier referenced to the square wave generator. The amplified signal was recorded as a function of the rotation angle θ.

4.5 Results

4.5.1 Noise Temperature

Simulation results of the input reflection loss from a Pickett-Potter and diagonal feedhorn at 1.9 THz can be seen in figure 4.7. We see that the Pickett-Potter horn

Table 4.2. Noise Temperature Measurements

Source Frequency (THz)	Potter Horn Noise Temp. (K)	Diagonal Horn Noise Temp. (K)
1.84	840	840
1.87	780	780
1.89	925	925

The dual side band (DSB) noise temperature of the Pickett-Potter feedhorn-transformer module compared to the diagonal feedhorn module. The uncertainty in each measurement is $T_N = \pm 30$ K. Measurements were taken with the multiplication chain tuned to three different frequencies. The noise temperature presented here is the average of several Y-factor measurements taken with each feedhorn module.

has a better performance across the band, but the diagonal horn has a lower S_{11} at the center frequency (-22.55 dB and -25.41 dB for the diagonal and Pickett Potter horns, respectively). We found the S_{11} of the waveguide circuitry, simulated in figure 4.2, to be below -32 dB in both CST and HFSS.

Table 4.2 shows the noise temperature calculated from Y-factor measurements comparing the Pickett-Potter-transformer feedhorn modules to the diagonal feedhorn modules. There was no distinguishable difference between the noise temperature between the diagonal horn and the Pickett-Potter feedhorn modules at all three source frequencies. The lowest noise temperature occurred slightly lower than the rest frequency of the [CII] emission line at 1.87 THz.

We expect a lower noise contribution from the Pickett-Potter feedhorn module horn varying between 2-5 dB at all three source frequencies. We would expect the contribution to the noise temperature from the machining errors of the transformer segment and oval waveguide to scale linearly frequency. It is highly unlikely that the machining errors would scale perfectly to match the difference in input reflection between the diagonal and Pickett-Potter feedhorn modules. Instead, we can reasonably

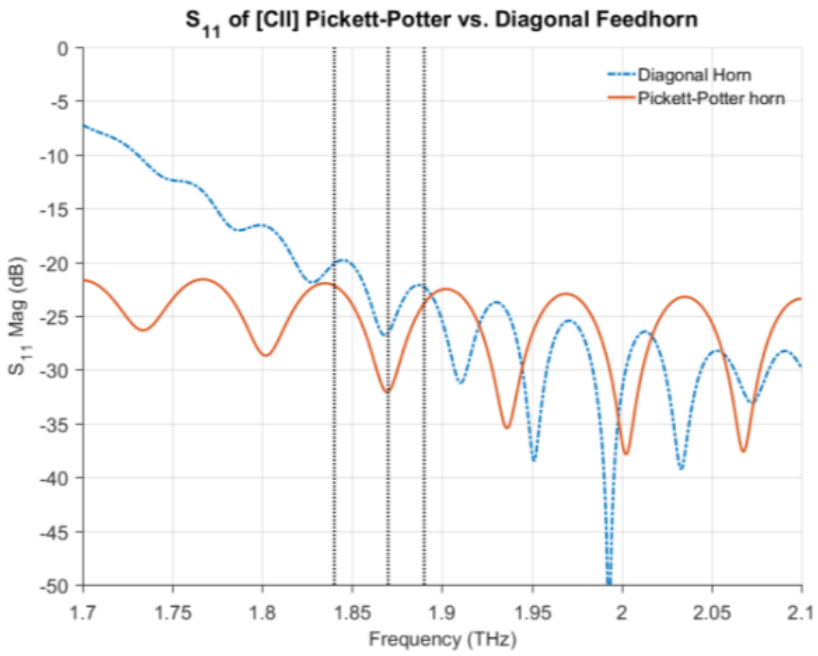

Figure 4.7. Simulated S_{11} of both a Pickett-Potter feedhorn (solid) and a diagonal feedhorn (dashed). The transformer and exit waveguide of the Pickett-Potter feedhorn was not included in these simulations. The three vertical lines indicate the frequency of the source for the noise temperature measurements.

conclude that the dominant noise contribution is coming from elsewhere in the system, likely from the mixer itself.

This result shows that the feedhorn-transformer modules we present do not contribute significantly to the noise performance of stat-of-the-art receiver systems. Though this method does not measure the performance of the module independently, it does demonstrate the suitability of the design for large scale emission line survey missions.

Table 4.3. Beamwaist Calculations

z (cm)	ω_0 (cm)
121.9	0.287
152.4	0.296
203.2	0.310
Average	0.298
GRASP	0.287
CST	0.288
Theory	0.281

There is a ± 0.050 mm uncertainty in ω_0 at all three scan planes, mostly due to the uncertainty of ± 5 mm uncertainty in z. The calculated beamwaist is slightly larger than the theoretical value for all three measurement scans. This was expected since we do not correct for the beam size of the source probe.

4.5.2 Radiation Pattern Measurements

Three scans of the radiation pattern were made by rotating the cryostat with a one-second integration at each point along the cut. We measure the radiation pattern at three distances z between the source probe aperture and the cryostat window. From each measurement scan, we first fit the beam to a first-order Gaussian profile and find the beam radius $\omega(z)$. We then calculate the initial beam waist at the aperture of the feedhorn, ω_0 at distance z using the following equation from Table 2.3 in Goldsmith 1998:

$$\omega_0^2 = \frac{\omega(z)^2}{2}\left\{1 \pm \left[1 - \left(\frac{2\lambda z}{\pi\omega\left(z\right)^2}\right)^2\right]^{0.5}\right\} \tag{4.2}$$

where ω_0 is the beamwaist, and $\omega\left(z\right)$ is the beam diameter at distance z . We use a first- order Gaussian fitting routine to calculate ω_0 from the raw data at all three scan planes. The measured beamwaists show good agreement to the theoretical beamwaist of $\omega_0 = 1.78\lambda = 0.288$ mm from Pickett et al. 1984.

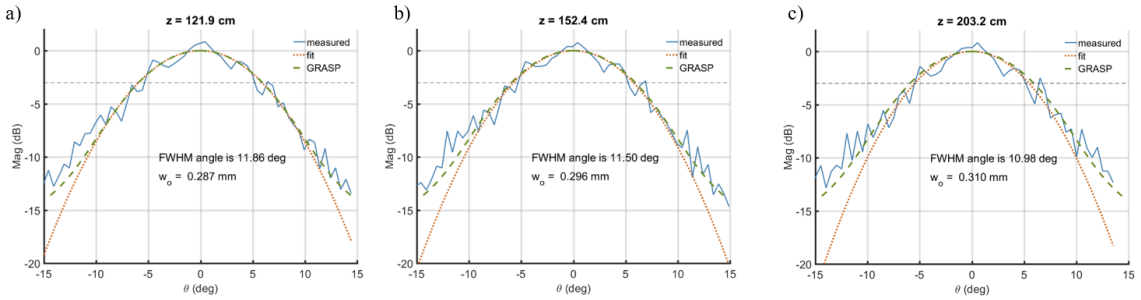

Figure 4.8. Measurement data (solid), first order Gaussian fit (dotted), and GRASP-simulated (dashed) radiation patterns of the feedhorn module. The measurement data was scaled such that the fit peaks at 0 dB. The -3 dB points are indicated by a horizontal dashed line in each plot.

In figure 4.8 we show the measured data from the radiation pattern measurements, a first order Gaussian fit to the data, and a simulated radiation pattern including the feedhorn and waveguide circuitry using GRASP (*GRASP* 2017).

Though the measurement data in figure 4.8 shows significant 'ripple' across the scan, the shape of the ripples is consistent between measurement planes. This consistency indicates that these ripples are most likely caused by standing waves in the system rather than spurious reflections caused by debris within the module. Despite the standing wave effect, the qualitative beam shape agrees well with simulations, as is summarized in table 4.3. We see that the fit and GRASP data agree with each other to at least the -3 dB level. Beyond that, the data agrees much better to the GRASP simulation than it does to the Gaussian fit. As the distance between the source and the receiver increases, the agreement between the simulation and measured beam pattern degrades, which we expect as the signal to noise ratio also decreases.

We do not see excessive beam distortion or boresight error as we trace the beam from one scan plane to the next. We show here that the manufacturing process used to fabricate these horns is reliable and does not negatively influence the beam pattern.

4.6 Conclusions

We have modeled, fabricated, and tested a CTR WGT, that can be easily machined directly into a feedhorn block. The advantages of an integrated architecture are a more precise alignment of waveguide circuitry features by reducing the number of times the milling machine must be referenced to the feedhorn block, and minimizing the machining time by implementing a monolithic rather than split feedhorn block. The performance of the integrated transformer is comparable to that of conventionally machined feedhorn profiles, and the implementation of the integrated blocks do not decrease the performance of the feedhorn profile chosen for a particular module. These new technological advances can serve as a pathway toward the implementation of cost-effective large monolithic focal plane array units.

Chapter 5

CONCLUSIONS AND FUTURE WORK

5.1 Science Motivation

Instrumentation development and characterization techniques presented in this dissertation are designed to enable better astronomical studies of ISM clouds with new frequency coverage and either high spectral resolution or large field of view. In order to better understand the origins of our Sun and our solar system, we need to understand how the gas and dust from previous generations of stars is recycled. We can do this by looking out into our Milky Way galaxy and studying nearby ISM cloud formation and disruption in detail. By studying the light in the THz frequency regime emitted directly from these clouds, we can study their formation processes, how they interact internally and with their surrounding environment, and how both new stars and external factors lead to their disruption. These studies can help give context to our the uniqueness of the formation of our solar system and help us to understand our place in the Milky Way galaxy and beyond.

Widefield cameras using broadband detectors do not match the spectral resolution of heterodyne instruments, but serve a complementary purpose to the study of ISM processes. These cameras can study astronomical clouds with a large spatial extent in order to best study cloud morphology. For example, there is an ongoing scientific debate as to how much the presence of turbulence within a cloud disrupts ongoing or future star formation. Widefield cameras with high spectral resolution can look for turbulent flows that can indicate recent or ongoing disruption. Additionally, wide field

cameras can take large surveys of ISM clouds. These surveys can be used to build up a statistical representation of clouds, by looking at a distribution in terms of size, age, thermal or radiation environment, interactions with other clouds or proximity to different types of stars, or spatial distribution throughout the galaxy.

Heterodyne instruments have the finest spectroscopic resolution in the THz frequency range, though with the pixel counts of the most state-of-the-art instruments they have a lower spatial resolution than widefield instruments. Spectroscopic instruments are able to detect the presence of different chemical species in these clouds as well as probe their thermal and kinematic properties. Combining the detailed chemical, thermal, and kinematic information provided by heterodyne instruments with the high spatial resoultion of other widefield images, we can piece togeter a model of how clouds form, evolve, and are recycled by the Milky Way.

Both heterodyne and direct detector instruments can help us study the properties of exoplanets. Near-infrared MKID cameras have been recently comissioned to work in conjunction with advanced adaptic optic systems and caronagraphs to surpress starlight from a host star in order to directly image exoplanets. The advantage that MKIDs offer over other direct detector instruments is that they have fast read times and are very close to being read-noise free. Heterodyne measurements help inform studies of exoplanets by studying the early protostellar environment of potential exoplanetary systems. In order for rocky planets to exist, there must be a sufficient absolute abundance of heavy elements present in the surrounding medium. As we better understand how these molecules form in the diffuse interstellar medium and are processed dense clouds before the star formation process begins, we can better model solar system processes based on the mechanics of the initial environment.

The device and system-level characterization techniques presented in this dis-

sertation help scientific studies by improving sensitivity and pointing knowledge of the cameras used for these missions. Beam pattern measurements can reconstruct the on-sky sensitivity pattern and further improve sensitivity by characterizing (and helping to remove) optical losses due to reflections or misalignment of elements in the receiver system. The waveguide transformer module described in chapter 4 helps improve sensitivity by eliminating potential misalignment and losses due to mismatches between receiver sub-assembly components. It also allows detector devices requiring rectangular feeds to use low-cross-pol sensitive feedhorn profiles, which can eliminate up to a 15% noise factor introduced at the feedhorn.

5.2 Future Work

The radiation pattern analysis pipeline developed through chapters 1-3 of this dissertation are useful for instrument characterization of both direct detector and heterodyne instruments. A pipeline that can handle arbitrarily large sapling planes and data types will be useful to have so that future measurements can focus more on instrument analysis rather than pipeline development. The measurement techniques introduced in this dissertation will help future beam pattern measurements be more precise and informative at diagnosing problems in an instrument's optical system. One of the main challenges to adapting the pipeline for future datasets will be coordinating the time-stamp between the scanner system and the data acquisition system, which is a minor challenge solved in software post-processing. Future improvements to this part of the analysis pipeline can streamline the process and being less memory-intensive, for example by windowing the timeseries of each dataset to more easily find a match between the position data and detector response. Lowering the end-to-end processing

time of a new dataset, a beam mapping system can be put in place in the optical path, and the pattern can be remeasured after adjustments are made to the system components to ensure maximum optical efficiency through the instrument.

The characterization technique described in chapters 2 and 3 is suitable to meet the characterization requirements for new advanced suites of direct-detector array instruments. Particularly for instruments where polarization sensitivity is important—potentially for CMB measurements but also for magnetic field polarization studies, dust polarization, and more—the ability to characterize co-polar and cross-polar sensitivity patterns for an array will allow tighter uncertainty limits in the scientific data. Future work on using this characterization technique is to push the frequency limits both higher and lower than the demonstrated performance, use it with new detector types, and characterize dual-polarization selective devices.

Both datasets in chapters 2 and 3 were measured at 350 GHz. Scaling up to higher frequency is possible with multiplication chains with sufficient output power to 'pump' the detector. Tests at 850 GHz are already underway to characterize the high frequency channel of the A-MKID instrument. Scaling up in frequency presents a technological challenge because the response time of the detector becomes a factor. This can be mitigated with appropriate selection of IF_{opt} frequency, where the $1/f$ noise decreases for higher IF_{opt}, though it must be sufficiently lower than the response time of the detector. There may be a practical limit to how high in frequency this technique can be used due to the instrument read-out technique. Infrared or X-ray MKID arrays are coming on to the instrumentation scene, but these instruments are not read out continuously. Instead, they are individual photon counting devices, and the coherent modulation technique, the foundation principle of the complex beam mapping scheme, cannot be applied.

However, for lower frequencies, the mapping technique we introduce should have little challenge being implemented. Indeed, the technique itself stems from applications in microwave detectors, and has only been relatively recently demonstrated in the THz regime. Polarization selective devices at 150 GHz, for CMB experiments and potential uses by the Office of Naval Research, are currently fabricated and could be a potential application of this technique (McCarrick et al. 2017). For MKIDs, the phase reference scheme presented in chapter 3 is easy to implement because it does not require any new software updates to the read-out electronics of the instrument. The data may need to be manipulated at the entry point to the post-processing pipeline according to the specific data format from a new instrument, but the subsequent analysis steps are designed to link together through the subsequent analysis steps. Additionally, the hardware integration is achieved by simply inserting a power combiner in the read-out electronics (in addition to the other hardware required by the scanning system) so is relatively easy to implement with existing architecture.

In order to apply this technique to TES arrays, consideration must be made to accommodate the time constant t_c of these detectors. TES detectors have been demonstrated for multiple instruments with $t_c \sim 1$ ms (Abitbol et al. 2017). It is conceivable, then, for the optical modulation to be detected if it is placed at fairly low $\mathrm{IF_{opt}}$ frequency, for example, at $\sim$100 Hz. In chapter 2 we use an $\mathrm{IF_{opt}}$ of only 400 Hz. Lower frequencies have a higher $1/f$ noise, which may limit the number of arrays where this technique will be effective, depending on other noise contributions to the system.

Another challenge for characterizing TES arrays is a new suitable phase referencing system will be necessary. For a single pixel receiver, triggered acquisition is suitable, following the referencing scheme presented in chapter 2. However, for array instruments,

the phase referencing scheme presented in chapter 3 is specific to MKID detectors and cannot be used for TES arrays, even when using a frequency domain multiplexing scheme. A triggered technique is possible, though the scan duration using a step-and-integrate scanning strategy used with this acquisition mode makes the data output excessively large. A potential solution could be to have a separate detector for the IF_{ref} signal that is timestamped appropriately to do a time comparison between the scanner system, reference signal, and TES signal in post-processing.

The direct metal-machining of feedhorn-integrated waveguide transformer modules presented in chapter 4 are already incorporated into the design of future missions that are in the proposal phase. These missions include Astrophysics Stratospheric Telescope for High spectral Resolution Observations at Submillimeter-wavelengths (ASTHROS) proposed for an APRA balloon mission and the Stratospheric Heterodyne Array System for Terahertz Astronomy (SHASTA) that will be submitted as a facility instrument for SOFIA. A SHASTA feedhorn module has been fabricated that uses a multi-flare angled horn profile rather than a Pickett-Potter feedhorn. The machining accuracy of the milling machine used in fabrication has designed features for use up to 4.7 THz, including a phase grating and ortho-mode transducer at those frequencies. At 63 μm, the smaller dimension of the rear oval waveguide at the exit would be 36 μm, which is barely within the size range of the smallest commercially available end mills of 30 μm.

Additionally, micro-machined monolithic horn arrays for use with MKID or TES arrays can benefit from these horn modules. Horn coupled devices for S4 instruments will likely not need a transformer since they are designed to be dual-polarization detectors and will probably have circular waveguide feeds. However, missions like AMKID, NIKA and others that use twin-slot antennas as on-chip absorbers could use

feedhorns for wide field imaging of ISM clouds or other objects. TES array cameras can also use these feedhorn profiles, perhaps for upgrades to the cameras on the South Pole Telescope.

One potential avenue for invesitgating the optical quality of these modules is to make a S_{11} measurement. The standard way to make this measurement would be using a vector network analyzer (VNA) as a source probe and receiver, with calibrated feedhorns such as a open-ended waveguide. One of the calibration feeds can then be swapped for a single pixel module for the measurement. However, this can be a challenging endeavor since there are not many calibrated VNAs that work up to these frequencies. Commercial companies are making extenders that reach the THz range, so there is potential for this type of measurement to be conducted at a few facilities that specialize in high frequency devices.

As astronomers dive deeper into answering the remaining questions of ISM evolution, instruments of all types are scaling to larger and larger arrays. The focus of this dissertation has been to address some of the challenges on the instrumentation side, to make large format arrays feasible and practical without sacrificing performance, timescale, or budget. With more advanced receiver systems, we can better understand the uniqueness of Earth and the Universe around us.

REFERENCES

Abazajian, Kevork N, Peter Adshead, Zeeshan Ahmed, Steven W Allen, David Alonso, Kam S Arnold, Carlo Baccigalupi, et al. 2016. "CMB-S4 Science Book, First Edition" (October).

Abitbol, Maximilian H., Zeeshan Ahmed, Darcy Barron, Ritoban Basu Thakur, Amy N. Bender, Bradford A. Benson, Colin A. Bischoff, et al. 2017. "CMB-S4 Technology Book, First Edition": 1–191. arXiv: arXiv:1706.02464.

Aguirre, J. 2015. *The Spectroscopic Terahertz Airborne Receiver for Far-InfraRed Exploration (STARFIRE): a Next-Generation Experiment for Galaxy Evolution Studies.* NASA APRA Proposal.

Balanis, Constantine A. 2005. *Antenna theory : analysis and design.* 3rd ed.. Hoboken, N.J.: Wiley-Interscience.

Baryshev, A. M., Hesper, R., Mena, F. P., Klapwijk, T. M., van Kempen, T. A., Hogerheijde, M. R., Jackson, B. D., et al. 2015. "The ALMA Band 9 receiver - Design, construction, characterization, and first light." *A&A* 577:A129. doi:10.1051/0004-6361/201425529.

Baryshev, Andrey, Ronald Hesper, and Wolfgang Wild. 2015. "ALMA Band 9 receiver design and performance." In *2015 IEEE MTT-S International Microwave Symposium, IMS 2015.* doi:10.1109/MWSYM.2015.7167144.

Baselmans, J. J. A., Bueno, J., Yates, S. J. C., Yurduseven, O., Llombart, N., Karatsu, K., Baryshev, A. M., et al. 2017. "A kilo-pixel imaging system for future space based far-infrared observatories using microwave kinetic inductance detectors." *A&A* 601:A89. doi:10.1051/0004-6361/201629653.

Baselmans, Jochem J A. 2012. "Kinetic Inductance Detectors." *Journal of Low Temperature Physics* (Boston) 167, no. 3 (May): 292–304.

Bernasconi, Peter. N., D. Neufeld, Christopher K Walker, D. Hollenbach, Jonathan H Kawamura, and J. Stuzki. 2010. "The stratospheric terahertz observatory." In *Johns Hopkins APL Technical Digest (Applied Physics Laboratory),* 28:238–239. 3.

Beyer, J. 2010. "Transition edge sensor series array bolometer." *Superconductor Science and Technology* 23 (10). doi:10.1088/0953-2048/23/10/105019.

Bisigello, L., S. J. C. Yates, V. Murugesan, J. J. A. Baselmans, and A. M. Baryshev. 2016. "Calibration Scheme for Large Kinetic Inductance Detector Arrays Based

on Readout Frequency Response." *J. Low Temp. Phys.* 184 (1): 161–166. doi:10.1007/s10909-016-1524-x.

Born, M., and Emil Wolf. 1994. *Principles of optics: Electromagnetic Theory of Propagation, Interference and Diffraction of Light,* 1–952. doi:10.1016/S0030-3992(00)00061-X. arXiv: arXiv:1011.1669v3.

Boussaha, F., J. Kawamura, J. Stern, A. Skalare, V. White, C. Jung, and I. Mehdi. 2011. "Development of waveguide balanced HEB receivers beyond 2 THz." In *IRMMW-THz 2011 - 36th International Conference on Infrared, Millimeter, and Terahertz Waves.* doi:10.1109/irmmw-THz.2011.6104836.

Bowman, Judd D., Alan E.E. Rogers, Raul A. Monsalve, Thomas J. Mozdzen, and Nivedita Mahesh. 2018. "An absorption profile centred at 78 megahertz in the sky-averaged spectrum." *Nature* 555 (7694): 67–70. doi:10.1038/nature25792.

Callen, Herbert B, and Theodore A Welton. 1951. "Irreversibility and Generalized Noise." *Phys. Rev.* 83, no. 1 (July): 34–40. doi:10.1103/PhysRev.83.34.

Calvo, M., Roesch, M., Désert, F.-X., Monfardini, A., Benoit, A., Mauskopf, P., Ade, P., et al. 2013. "Improved mm-wave photometry for kinetic inductance detectors." *A&A* 551:L12. doi:10.1051/0004-6361/201219854.

Carter, M., A. Baryshev, R. Hesper, S.J. Wijnholds, W. Jellema, and T. Zijlstra. 2002. "Phase and Amplitude Antenna Measurements on an SIS Mixer Fitted with a Double Slot Antenna for ALMA Band 9." In *Thirteenth International Symposium on Space Terahertz Technology,* 515–524. March.

Chahat, Nacer, Theodore J Reck, Cecile Jung-Kubiak, Tinh Nguyen, Ronan Sauleau, and Goutam Chattopadhyay. 2015. "1.9-THz Multiflare Angle Horn Optimization for Space Instruments." *Terahertz Science and Technology, IEEE Transactions on* (USA) 5, no. 6 (November): 914–921. doi:10.1109/TTHZ.2015.2487781.

CST Microwave Studio. 2016. https://www.cst.com/.

Davis, Kristina K, Willem Jellema, Stephen J C Yates, Lorenza Ferrari, Jochem J A Baselmans, Kotaro Kohno, David Thoen, Vignesh Murugesan, and Andrey M Baryshev. 2017. "Proof-of-Concept Demonstration of Vector Beam Pattern Measurements of Kinetic Inductance Detectors." *Terahertz Science and Technology, IEEE Transactions on* (USA) 7, no. 1 (January): 98–106. doi:10.1109/TTHZ.2016.2617869.

Day, Peter K, Henry G Leduc, Benjamin A Mazin, Anastasios Vayonakis, and Jonas Zmuidzinas. 2003. "A broadband superconducting detector suitable for use in large arrays." *Nature* 425, no. 6960 (October).

Dober, Brad, J. A. Austermann, J. A. Beall, D. Becker, George Che, Hsiao-Mei M. Cho, Mark Devlin, et al. 2016. "Optical Demonstration of THz, Dual-Polarization Sensitive Microwave Kinetic Inductance Detectors." *Journal of Low Temperature Physics* 184, nos. 1-2 (July): 173–179. doi:10.1007/s10909-015-1434-3. arXiv: 1603.02963.

Doyle, Simon, P. Mauskopf, J. Naylon, A. Porch, and C. Duncombe. 2008. "Lumped element kinetic inductance detectors." *Journal of Low Temperature Physics* 151 (1-2 PART 1): 530–536. doi:10.1007/s10909-007-9685-2.

Draine, B. T. 1978. "Photoelectric heating of interstellar gas." *The Astrophysical Journal Supplement Series* 36:595. doi:10.1086/190513.

Field, G., D. Goldsmith, and H. Habing. 1969. "Cosmic-Ray Heating of the Interstellar Gas." *Astrophysical Journal* 155:149–149. doi:10.1086/180324.

Functions, Bessel, By Tom, Irvine Email, Differential Equation, Bessel Function, First Kind, Zero Order, First Order, and Martin Kreh. 2012. "Bessel Functions." *Order A Journal On The Theory Of Ordered Sets And Its Applications:* 1–21. doi:doi:10.1201/9781420034790.axc.

Galitzki, Nicholas, Peter A. R. Ade, Francesco E. Angilè, Peter Ashton, James A. Beall, Dan Becker, Kristi J. Bradford, et al. 2014. "The Next Generation BLAST Experiment." *Journal of Astronomical Instrumentation* 03, no. 02 (September): 1440001. doi:10.1142/S2251171714400017. arXiv: 1409.7084.

Gao, Jiansong, Jonas Zmuidzinas, Benjamin A. Mazin, Henry G. LeDuc, and Peter K. Day. 2007. "Noise properties of superconducting coplanar waveguide microwave resonators." *Appl. Phys. Lett.* 90, 102507 (10). doi:http://dx.doi.org/10.1063/1.2711770.

Goldsmith, Paul F. 1998. *Quasioptical systems : Gaussian beam quasioptical propagation and applications.* IEEE Press/Chapman & Hall Publishers series on microwave technology and RF Quasioptical systems.

Goldsmith, Paul F, William D Langer, Jorge L Pineda, and T Velusamy. 2012. "Collisional excitation of the [C II] fine structure transition in interstellar clouds." *Astrophysical Journal, Supplement Series* 203, no. 1 (September). doi:10.1088/0067-0049/203/1/13. arXiv: 1209.4536.

GRASP. 2017. http://www.ticra.com/products/software/grasp.

Griffin, M, Jochem J A Baselmans, Andrey M Baryshev, Simon Doyle, M Grim, P Hargrave, T Klapwijk, et al. 2015. "SPACEKIDS: Kinetic inductance detector arrays for space applications." In *The Institute of Electrical and Electronics Engineers, Inc. (IEEE) Conference Proceedings.* 1–2. August. http://search.proquest.com/docview/1778012919/.

HFSS. 2014. http://www.ansys.com/Products/Electronics/ANSYS-HFSS.

Hollis, J. Searcy, and H. Allen Ecker. 1973. "Determination of Far-Field Antenna Patterns from Near-Field Measurements." *Proceedings of the IEEE* 61 (12): 1668–1694. doi:10.1109/PROC.1973.9358.

Holzman, Eric L. 2005. "A simple circular-to-rectangular waveguide transition." *IEEE Microwave and Wireless Components Letters* 15 (1): 25–26. doi:10.1109/LMWC.2004.840969.

Inc., The MathWorks. 2016. *MATLAB (R2016b).* doi:10.1007/s10766-008-0082-5.

Irwin, K D, and G C Hilton. 2005. "Transition-Edge Sensors." Chap. Transition in *Cryogenic Particle Detection,* 99:63–149. Springer-Verlag. http://venus.ifca.unican.es/%7B~%7Dxray/XEUS/archivopapers/TESIrwinHilton.pdf.

Isernia, Tommaso, Giovanni Leone, and Rocco Pierri. 1996. "Radiation pattern evaluation from near-field intensities on planes." *IEEE Transactions on Antennas and Propagation* 44 (5): 701–710. doi:10.1109/8.496257.

Janssen, R. M.J., J. J.A. Baselmans, A. Endo, L. Ferrari, S. J.C. Yates, A. M. Baryshev, and T. M. Klapwijk. 2013. "High optical efficiency and photon noise limited sensitivity of microwave kinetic inductance detectors using phase readout." *Applied Physics Letters* 103 (20). doi:10.1063/1.4829657. arXiv: arXiv:1311.2429v1.

Jellema, Willem. 2015. "Optical design and performance verification of Herschel-HIFI." PhD diss., University of Groningen.

Johansson, Joakim F., and Nicholas D. Whyborn. 2000. "Diagonal horn as a submillimeter wave antenna." *IEEE Transactions on Microwave Theory and Techniques* 40, no. 5 (May): 795–800. doi:10.1109/22.137380.

Karpen, E. W., and R. J. Mohr. 1966. "Graphical Presentation of Spurious Responses in Tunable Superheterodyne Receivers." In *1966 Symposium Digest: 8th National*

Symposium on Electromagnetic Compatibility, 1–5. July. doi:10.1109/ISEMC.1966.7567080.

Kloosterman, Jenna, Brandon Swift, William Peters, David Lesser, Criag Kulesa, Casey Honniball, Christian Villegas, et al. 2014. "Engineering and science data from SuperCam: A 64-pixel heterodyne receiver for CO J=3-2 at 345 GHz." In *2014 39th International Conference on Infrared, Millimeter, and Terahertz waves (IRMMW-THz),* 1–2. IEEE, September. doi:10.1109/IRMMW-THz.2014.6956072.

Kovacs, A. 2008. "Scanning strategies for imaging arrays." In *Proceedings of the SPIE.* June. doi:10.1117/12.790272. arXiv: 0806.4888.

Landau, H. J. 1967. "Sampling, Data Transmission, and the Nyquist Rate." *Proceedings of the IEEE* 55 (10): 1701–1706. doi:10.1109/PROC.1967.5962.

Leach, W. Marshall, and Demetrius T. Paris. 1973. "Probe Compensated Near-Field Measurements on a Cylinder." *IEEE Transactions on Antennas and Propagation* 21 (4): 435–445. doi:10.1109/TAP.1973.1140520.

Lovas, Frank J., and Paul H. Krupenie. 1974. "Microwave Spectra of Molecules of Astrophysical Interest VII. Carbon Monoxide, Carbon Monosulfide, and Silicon Monoxide." *Journal of Physical and Chemical Reference Data* 3 (1): 245–257. doi:10.1063/1.3253140.

Lucas, S. K., and H. A. Stone. 1995. "Evaluating infinite integrals involving Bessel functions of arbitrary order." *Journal of Computational and Applied Mathematics* 64 (3): 217–231. doi:10.1016/0377-0427(95)00142-5.

Lüke, Dieter. 1999. "Origins of the sampling theorem." *IEEE Communications Magazine* 37 (4): 106–108. doi:10.1109/35.755459.

Marquardt, Donald W. 1963. "An Algorithm for Least-Squares Estimation of Nonlinear Parameters." *Journal of the Society for Industrial and Applied Mathematics* 11 (2): 431–441. doi:10.1137/0111030. arXiv: arXiv:1011.1669v3.

McCarrick, H., G Jones, B R Johnson, M H Abitbol, P A R Ade, S Bryan, P Day, et al. 2017. "Design and performance of dual-polarization lumped-element kinetic inductance detectors for millimeter-wave polarimetry." *Astronomy&aAstrophysics.* doi:10.1051/0004-6361/201732044. arXiv: 1710.02239.

McKee, C. F., and J. P. Ostriker. 1977. "A theory of the interstellar medium - Three components regulated by supernova explosions in an inhomogeneous substrate." *The Astrophysical Journal* 218:148. doi:10.1086/155667. arXiv: 1101.5669.

Munir, Achmad, and Muhammad Fathi Yakan Musthofa. 2011. "Rectangular to circular waveguide converter for microwave devices characterization." *International Journal on Electrical Engineering and Informatics* 3 (3): 350–359.

Murphy, A., T. Peacocke, B. Maffei, I. McAuley, F. Noviello, V. Yurchenko, R. Ade, et al. 2010. "Multi-mode horn design and beam characteristics for the Planck satellite." *Journal of Instrumentation* 5 (4). doi:10.1088/1748-0221/5/04/T04001.

Murphy, J. A. 1987. "Distortion of a simple Gaussian beam on reflection from off-axis ellipsoidal mirrors." *Int. J. Infrared and Milli. Waves* 8, no. 9 (September): 1165–1187. doi:10.1007/BF01010819.

Naruse, Masato, Tetsuya Ito, Yutaro Sekimoto, Hiroyuki Toba, Naohisa Satou, Masahiro Sugimoto, Wenlei Shan, et al. 2009. "Near-field beam pattern measurement of qualification model of ALMA band 8 (385-500 GHz) cartridge receiver." *Experimental Astronomy* 24 (1-3): 89–107. doi:10.1007/s10686-008-9136-3.

Nelder, J. A., and R. Mead. 1965. "A simplex method for function minimization." *Computer Journal* 7 (4): 308–313. doi:10.1093/comjnl/7.4.308.

Novotny, L., M. Frimmer, and R. Reimann. 2016. *Angular Spectrum Representation.* https://www.photonics.ethz.ch/fileadmin/user%7B%5C_%7Dupload/Courses/EM%7B%5C_%7DFieldsAndWaves/AngularSpectrumRepresentation.pdf.

Otal, Luis. 2014. "The Optical System and the Astronomical Potential of A-MKID, a New Camera Using Microwave Kinetic Inductance Detectors." PhD diss., Rheinischen Friedrich-Wilhelms-Universität Bonn. http://hss.ulb.uni-bonn.de/2015/4094/4094.pdf.

Paris, Demetrius T., W. Marshall Leach, and Edward B. Joy. 1978. "Basic Theory of Probe-Compensated Near-Field Measurements." *IEEE Transactions on Antennas and Propagation* 26 (3): 373–379. doi:10.1109/TAP.1978.1141855.

Parker, E. N. 1966. "The Dynamical State of the Interstellar Gas and Field." *The Astrophysical Journal* 145:811. doi:10.1086/148828. arXiv: 0603851 [astro-ph].

Paveliev, D. G., Y. I. Koshurinov, A. S. Ivanov, A. N. Panin, V. L. Vax, V. I. Gavrilenko, A. V. Antonov, V. M. Ustinov, and A. E. Zhukov. 2012. "Experimental study of frequency multipliers based on a GaAs/AlAs semiconductor superlattices in the terahertz frequency range." *Semiconductors* 46 (1): 121–125. doi:10.1134/S1063782612010150.

Pawlan, Jeffrey. 2015. "Compact and easy to manufacture dual mode feed horn with ultra-low backlobes." In *2015 German Microwave Conference, GeMiC 2015,* 355–358. doi:10.1109/GEMIC.2015.7107826.

Pickett, Herbert M., John C. Hardy, J. Jam, and F. Farhoomand. 1984. "Characterization of a Dual-Mode Horn for Submillimeter Wavelengths." *IEEE Transactions on Microwave Theory and Techniques* 32, no. 8 (August): 936–937. doi:10.1109/TMTT.1984.1132801.

Piovan, G., and F. Bullo. 2012. "On Coordinate-Free Rotation Decomposition: Euler Angles About Arbitrary Axes." *IEEE Transactions on Robotics* 28, no. 3 (June): 728–733. doi:10.1109/TRO.2012.2184951.

Preibisch, Thomas, Veronica Roccatagliata, Benjamin Gaczkowski, and Thorsten Ratzka. 2012. "Herschel far-infrared observations of the Carina Nebula complex I. Introduction and global cloud structure." *Astronomy & Astrophysics* 541:A132. doi:10.1051/0004-6361/201218851. arXiv: 1303.5201.

Rantwijk, J. van, M. Grim, D. van Loon, S. Yates, A. Baryshev, and J. Baselmans. 2016. "Multiplexed Readout for 1000-Pixel Arrays of Microwave Kinetic Inductance Detectors." *IEEE Trans. Microw. Theory Techn.* 64, no. 6 (June): 1876–1883. doi:10.1109/TMTT.2016.2544303.

Rebolledo, David, Michael Burton, Anne Green, Catherine Braiding, Sergio Molinari, Graeme Wong, Rebecca Blackwell, Davide Elia, and Eugenio Schisano. 2016. "The Carina Nebula and Gum 31 molecular complex - I. Molecular gas distribution, column densities, and dust temperatures." *Monthly Notices of the Royal Astronomical Society* 456 (3): 2406–2424. doi:10.1093/mnras/stv2776. arXiv: 1511.07513.

Risacher, Christophe, Rolf Gusten, Jurgen Stutzki, Heinz Wilhelm Hubers, Denis Buchel, Urs U. Graf, Stefan Heyminck, et al. 2016. "First Supra-THz Heterodyne Array Receivers for Astronomy with the SOFIA Observatory." *IEEE Transactions on Terahertz Science and Technology* 6, no. 2 (March): 199–211. doi:10.1109/TTHZ.2015.2508005.

Robertson, Duncan A., Johannes E. McKay, Robert I. Hunter, Peter J. Speirs, and Graham M. Smith. 2016. "High Gaussicity feedhorns for sub-/ millimeter wave applications." In *International Conference on Infrared, Millimeter, and Terahertz Waves, IRMMW-THz,* vol. 2016-Novem, 1–2. IEEE, September. doi:10.1109/IRMMW-THz.2016.7758492.

Roccatagliata, V., T. Preibisch, T. Ratzka, and B. Gaczkowski. 2013. "Herschel far-infrared observations of the Carina Nebula complex." *Astronomy & Astrophysics* 554:A6. doi:10.1051/0004-6361/201321081. arXiv: 1303.5201.

Romani, R. W., a. J. Miller, B. Cabrera, E. Figueroa-Feliciano, and S. W. Nam. 1999. "First Astronomical Application of a Cryogenic Transition Edge Sensor Spectrophotometer." *The Astrophysical Journal* 521 (2): L153–L156. doi:10.1086/312202.

Rosenberg, U, J Bornemann, and K Rambabu. 2002. "Analysis and Design of Flange-Integrated Rectangular-To-Circular Waveguide Transformers for Splashplate Antenna Feeds." In *Microwave Conference, 2002. 32nd European,* 1–4. IEEE, September.

Ruze, J. 1966. "Antenna tolerance theory #8212;A review." *Proc. IEEE* 54, no. 4 (April): 633–640. doi:10.1109/PROC.1966.4784.

Saslaw, William C., and John E. Gaustad. 1969. "Interstellar Dust and Diamonds." *Nature* 221 (5176): 160–162. doi:10.1038/221160b0.

Savage, Blair D., and John S. Mathis. 1979. "Observed Properties of Interstellar Dust." *Annual Review of Astronomy and Astrophysics* 17 (1): 73–111. doi:10.1146/annurev.aa.17.090179.000445. arXiv: arXiv:1011.1669v3.

Siles, Jose V, Goutam Chattopadhyay, E Schlecht, C Lee, R Lin, J Gill, J Ward, et al. 2012. "Next generation solid-state broadband frequency-multiplied terahertz sources." In *Antennas and Propagation Society International Symposium (APSURSI), 2012 IEEE,* 1–2. IEEE, July.

Solomon, Philip M. 1973. "Interstellar molecules." *Physics Today* 26 (3): 32–40. doi:10.1063/1.3127983.

Spang, Matthias, Tina Stoeckel, Goeran Schubert, and Manfred Albach. 2010. "Application of probes with multiple outputs on probe-compensated EMC near-field measurements." In *Proceedings of the IEEE International Conference on Industrial Technology,* 188–193. doi:10.1109/ICIT.2010.5472677.

Stuchly, S, and A Kraszewski. 1965. "Wide-Band Rectangular to Circular Waveguide Mode and Impedance Transformer (Correspondence)." *Microwave Theory and Techniques, IEEE Transactions on* (USA) 13, no. 3 (May): 379–380.

Tervo, Jani, and Jari Turunen. 2002. "Angular spectrum representation of partially coherent electromagnetic fields." *Optics Communications* 209 (1-3): 7–16. doi:10.1016/S0030-4018(02)01665-6.

Teyssier, D, N D Whyborn, W Luinge, W Jellema, J W Kooi, P Dieleman, and T D Graauw. 2008. "HIFI pre-launch calibration results." In *19th International Symposium on Space Terahertz Technology, ISSTT 2008,* 113–120.

Thomas, Christopher N, and Stafford Withington. 2013. "Optical modeling techniques for multimode horn-coupled power detectors for submillimeter and far-infrared astronomy." *Journal of the Optical Society of America. A, Optics, image science, and vision* 30 (8): 1703–13. doi:10.1364/JOSAA.30.001703.

Thomas, Christopher, and Stafford Withington. 2012. "Experimental demonstration of an interferometric technique for characterizing the full optical behavior of multi-mode power detectors." In *IEEE Transactions on Terahertz Science and Technology,* 2:50–60. 1. January. doi:10.1109/TTHZ.2011.2177693.

Tielens, A.˜G.˜G.˜M. 2005. *The Physics and Chemistry of the Interstellar Medium,* 510. doi:10.1017/CBO9780511819056.

Tkadlec, Roman, and Zdeněk Nováček. 2005. "Radiation pattern reconstruction from the near-field amplitude measurement on two planes using PSO." *Radioengineering* 14 (4): 63–67.

Tong, C. Y Edward, Denis V. Meledin, Dan P. Marrone, Scott N. Paine, Hugh Gibson, and Raymond Blundell. 2003. *Near field vector beam measurements at 1 THz.* doi:10.1109/LMWC.2003.814602.

Tong, Cheuk-yu Edward, Scott Paine, and Raymond Blundell. 1994. "Near-Field Characterization of 2-D Beam Patterns of Submillimeter Superconducting Receivers." *5th ISSTT Proceedings:* 660–673.

Walker, Christopher K. 2015a. "SuperCam: A 64 pixel SIS receiver array for submillimeter-wave astronomy." In *2015 IEEE MTT-S International Microwave Symposium, IMS 2015,* 1–4. IEEE, May. doi:10.1109/MWSYM.2015.7166873.

———. 2015b. *Terahertz Astronomy.* 1st. 1–335. CRC Press.

Weisstein, Eric W. 2014. "Sampling Theorem." *Wolfram MathWorld:* 1. doi:10.3840/08004298.

Yaghjian, Arthur D. 1986. "An Overview of Near-Field Antenna Measurements." *IEEE Transactions on Antennas and Propagation* 34 (1): 30–45. doi:10.1109/TAP.1986.1143727.

Yates, S.J.C., J.J.A. Baselmans, A. M. Baryshev, S. Doyle, A. Endo, L. Ferrari, S. Hochgürtel, and B. Klein. 2014. "Clean beam patterns with low crosstalk using 850 GHz microwave kinetic inductance detectors." *Journal of Low Temperature Physics* 176 (5-6): 761–766. doi:10.1007/s10909-013-1034-z.

Yates, Stephen J.C., Andrey M. Baryshev, Ozan Yurduseven, Juan Bueno, Kristina K Davis, Lorenza Ferrari, Willem Jellema, et al. 2017. "Surface Wave Control for Large Arrays of Microwave Kinetic Inductance Detectors." *IEEE Transactions on Terahertz Science and Technology* (Piscataway) 7, no. 6 (January): 789–799. doi:10.1109/TTHZ.2017.2755500. arXiv: 1707.02142.

Yousif, Hashim A., and Richard Melka. 1997. "Bessel function of the first kind with complex argument." *Computer Physics Communications* 106 (3): 199–206. doi:10.1016/S0010-4655(97)00087-8.

Zemax. 2017. Kirkland. https://www.zemax.com/.

Zhao, Xuhao, Chengwei Yuan, Qiang Zhang, and Lishan Zhao. 2016. "Design and experiment study of compact circular-rectangular waveguide mode converter." *Review of Scientific Instruments* 87, no. 7 (July).

Zhu, Yang Ming. 1992. "Generalized Sampling Theorem." *IEEE Transactions on Circuits and Systems II: Analog and Digital Signal Processing* 39 (8): 587–588. doi:10.1109/82.168954.

Zmuidzinas, Jonas. 2012. "Superconducting Microresonators: Physics and Applications." *Annual Review of Condensed Matter Physics* 3 (1): 169–214. doi:10.1146/annurev-conmatphys-020911-125022.